LANGLEY GRANT
IN-02-CR
12585
p 141

NONEQUILIBRIUM RADIATION AND CHEMISTRY MODELS FOR AEROCAPTURE VEHICLE FLOWFIELDS

Volume II

AEROSPACE ENGINEERING DEPARTMENT

Semiannual Progress Report
July 1990 -- December 1990

TEXAS A&M UNIVERSITY

TAMRF Report No. 6382-91-01-(II)

February 1991

(NASA-CR-188198) NONEQUILIBRIUM RADIATION AND CHEMISTRY MODELS FOR AEROCAPTURE VEHICLE FLOWFIELDS, VOLUME 2 Semiannual Progress Report, Jul. - Dec. 1990 (Texas A&M Univ.) 142 p
CSCL 01A G3/02
N91-24101
535068
Unclas
0012585

NASA Grant No. NAG-1-1003

Leland A. Carlson
Professor of Aerospace Engineering
Texas A&M University
College Station, TX 77843-3141

TEXAS ENGINEERING EXPERIMENT STATION

THE EFFECTS OF SHOCK WAVE PRECURSORS AHEAD OF HYPERSONIC ENTRY VEHICLES

A Thesis

by

SCOTT ALAN STANLEY

Submitted to the Office of Graduate Studies of
Texas A&M University
in partial fulfillment of the requirements for the degree of

MASTER OF SCIENCE

December 1990

Major Subject: Aerospace Engineering

NONEQUILIBRIUM RADIATION AND CHEMISTRY MODELS FOR AEROCAPTURE VEHICLE FLOWFIELDS

Volume II

Semiannual Progress Report

July 1990 -- December 1990

TAMRF Report No. 6382-91-01-(II)

February 1991

NASA Grant No. NAG-1-1003

Leland A. Carlson
Professor of Aerospace Engineering
Texas A&M University
College Station, TX 77843-3141

THE EFFECTS OF SHOCK WAVE PRECURSORS AHEAD OF HYPERSONIC ENTRY VEHICLES

A Thesis

by

SCOTT ALAN STANLEY

Approved as to style and content by:

Leland A. Carlson
(Chair of Committee)

Walter E. Haisler
(Head of Department)

Richard E. Thomas
(Member)

Ricardo L. Diaz
(Member)

December 1990

ABSTRACT

The Effects of Shock Wave Precursors Ahead of

Hypersonic Entry Vehicles. (December 1990)

Scott Alan Stanley, B.S., Texas A&M University

Chair of Advisory Committee: Dr. Leland Carlson

A computational method and computer program have been developed to model the nonequilibrium shock wave precursor in a nitrogen gas. This method includes the effects of both chemical and thermal nonequilibrium. As part of this research, expressions have been derived for the mass production of each species due to photochemical reactions as well as for the effects of the absorption and emission of radiation on each individual energy mode of the gas. The shock layer and the radiative transfer solutions have been obtained by utilizing existing computational methods. The test cases presented represent entry conditions into the earth's atmosphere for an aerocapture vehicle returning from Mars.

ACKNOWLEDGEMENTS

I wish to thank my advisory committee for their participation as well as patience. Special thanks go to Leland Carlson for his everyday support and understanding. Thanks also go to Tom Gally for his opinions and ideas as well as shared knowledge. I also wish to thank Krista Witte for her continued support and patience as well as assistance in preparing this document. Funding for this project was provided by NASA Langley Research Center under NASA Grant No. NAG 1-1003 with Lin Hartung, Aerothermodynamics Branch, as technical monitor.

TABLE OF CONTENTS

Page

INTRODUCTION 1

PRECURSOR FORMULATION 6
Gas Model 9
Governing Equations 12
Solution Scheme 16

RADIATION FORMULATION 19
Equations of Radiative Transfer 20
Radiative Processes 27

SHOCK LAYER FORMULATION 41

GLOBAL SOLUTION SCHEME 47

RESULTS 50
Detailed Discussion of Case 1 (Alt = 72 Km, V_∞ = 16 Km/sec) 52
Parametric Studies 69

CONCLUSIONS AND RECOMMENDATIONS FOR FUTURE WORK 87

REFERENCES 88

APPENDIX A 92

APPENDIX B 106

APPENDIX C 113

VITA 126

LIST OF FIGURES

Page

Figure 1: Nonequilibrium Shock Wave Structure 7

Figure 2: Geometry Associated with the Tangent Slab Approximation 21

Figure 3: Propagation of Radiative Energy from Finite and Infinite Slabs 24

Figure 4: Energy Diagram for Molecular Nitrogen 30

Figure 5: Potential Energy Curves for Molecular Nitrogen 34

Figure 6: Coordinate System for the Viscous Shock Layer Program 44

Figure 7: Block Diagram of the Global Iteration Scheme 48

Figure 8: Heavy Particle Temperature in the Precursor Region;
(Alt = 72 Km, V_∞ = 16 Km/sec) 53

Figure 9: Electron/Electronic Temperature in the Precursor Region;
(Alt = 72 Km, V_∞ = 16 Km/sec) 53

Figure 10: Total Enthalpy in the Precursor Region;
(Alt = 72 Km, V_∞ = 16 Km/sec) 54

Figure 11: Electron/Electronic Energy in the Precursor Region;
(Alt = 72 Km, V_∞ = 16 Km/sec) 54

Figure 12: Pressure in the Precursor Region;
(Alt = 72 Km, V_∞ = 16 Km/sec) 55

Figure 13: Density in the Precursor Region;
(Alt = 72 Km, V_∞ = 16 Km/sec) 55

Figure 14: Velocity in the Precursor Region;
(Alt = 72 Km, V_∞ = 16 Km/sec) 56

Figure 15: N_2 Mass Fraction in the Precursor Region;
(Alt = 72 Km, V_∞ = 16 Km/sec) 56

Figure 16: N_2^+ Mass Fraction in the Precursor Region;
(Alt = 72 Km, V_∞ = 16 Km/sec) 57

Figure 17: N Mass Fraction in the Precursor Region;
(Alt = 72 Km, V_∞ = 16 Km/sec) 57

Figure 18: N^+ Mass Fraction in the Precursor Region;
(Alt = 72 Km, V_∞ = 16 Km/sec) 58

Figure 19: e^- Mass Fraction in the Precursor Region;
(Alt = 72 Km, V_∞ = 16 Km/sec) 58

Figure 20: Radiative Flux Through the Shock Front;
(Alt = 72 Km, V_∞ = 16 Km/sec) 62

Figure 21: Heavy Particle Temperature in the Shock Layer;
(Alt = 72 Km, V_∞ = 16 Km/sec) 64

Figure 22: Electron Temperature in the Shock Layer;
(Alt = 72 Km, V_∞ = 16 Km/sec) 64

Figure 23: Pressure in the Shock Layer;
(Alt = 72 Km, V_∞ = 16 Km/sec) 65

Figure 24: Density in the Shock Layer;
(Alt = 72 Km, V_∞ = 16 Km/sec) 65

Figure 25: N_2 Mass Fraction in the Shock Layer;
(Alt = 72 Km, V_∞ = 16 Km/sec) 66

Figure 26: N_2^+ Mass Fraction in the Shock Layer;
(Alt = 72 Km, V_∞ = 16 Km/sec) 66

Figure 27: N Mass Fraction in the Shock Layer;
(Alt = 72 Km, V_∞ = 16 Km/sec) 67

Figure 28: N^+ Mass Fraction in the Shock Layer;
(Alt = 72 Km, V_∞ = 16 Km/sec) 67

Figure 29: e^- Mass Fraction in the Shock Layer;
(Alt = 72 Km, V_∞ = 16 Km/sec) 68

Figure 30: Electron Temperature in the Nonequilibrium Region of
the Shock Layer; (Alt = 72 Km, V_∞ = 16 Km/sec) 70

Figure 31: N_2 Mass Fraction in the Nonequilibrium Region of the Shock Layer; (Alt = 72 Km, V_∞ = 16 Km/sec) 70

Figure 32: N_2^+ Mass Fraction in the Nonequilibrium Region of the Shock Layer; (Alt = 72 Km, V_∞ = 16 Km/sec) 71

Figure 33: N Mass Fraction in the Nonequilibrium Region of the Shock Layer; (Alt = 72 Km, V_∞ = 16 Km/sec) 71

Figure 34: N^+ Mass Fraction in the Nonequilibrium Region of the Shock Layer; (Alt = 72 Km, V_∞ = 16 Km/sec) 72

Figure 35: e^- Mass Fraction in the Nonequilibrium Region of the Shock Layer; (Alt = 72 Km, V_∞ = 16 Km/sec) 72

Figure 36: The Variation of Heavy Particle Temperature with Altitude in the Precursor Region; (Alt = 72, 75 and 80 Km, V_∞ = 16 Km/sec) . . . 73

Figure 37: The Variation of Electron/Electronic Temperature with Altitude in the Precursor Region; (Alt = 72, 75 and 80 Km, V_∞ = 16 Km/sec) . 73

Figure 38: The Variation of Total Enthalpy with Altitude in the Precursor Region; (Alt = 72, 75 and 80 Km, V_∞ = 16 Km/sec) 74

Figure 39: The Variation of Electron/Electronic Energy with Altitude in the Precursor Region; (Alt = 72, 75 and 80 Km, V_∞ = 16 Km/sec) . . . 74

Figure 40: The Variation of Pressure with Altitude in the Precursor Region; (Alt = 72, 75 and 80 Km, V_∞ = 16 Km/sec) 75

Figure 41: The Variation of N_2 Mass Fraction with Altitude in the Precursor Region; (Alt = 72, 75 and 80 Km, V_∞ = 16 Km/sec) 75

Figure 42: The Variation of N_2^+ Mass Fraction with Altitude in the Precursor Region; (Alt = 72, 75 and 80 Km, V_∞ = 16 Km/sec) 76

Figure 43: The Variation N Mass Fraction with Altitude in the Precursor Region; (Alt = 72, 75 and 80 Km, V_∞ = 16 Km/sec) 76

Figure 44: The Variation of N^+ Mass Fraction with Altitude in the Precursor Region; (Alt = 72, 75 and 80 Km, V_∞ = 16 Km/sec) 77

Figure 45: The Variation of e^- Mass Fraction with Altitude in the Precursor Region; (Alt = 72, 75 and 80 Km, V_∞ = 16 Km/sec) 77

Figure 46: Variation of the Radiative Flux Through the Shock with Velocity and Altitude 79

Figure 47: The Variation of Heavy Particle Temperature with Velocity in the Precursor Region; (Alt = 80 Km, V_∞ = 10, 12, 14 and 16 Km/sec) . 80

Figure 48: The Variation of Electron/Electronic Temperature with Velocity in the Precursor Region; (Alt = 80 Km, V_∞ = 10, 12, 14 and 16 Km/sec) 80

Figure 49: The Variation of Total Enthalpy with Velocity in the Precursor Region; (Alt = 80 Km, V_∞ = 10, 12, 14 and 16 Km/sec) 81

Figure 50: The Variation of Electron/Electronic Energy with Velocity in the Precursor Region; (Alt = 80 Km, V_∞ = 10, 12, 14 and 16 Km/sec) . 81

Figure 51: The Variation of Pressure with Velocity in the Precursor Region; (Alt = 80 Km, V_∞ = 10, 12, 14 and 16 Km/sec) 82

Figure 52: The Variation of N_2 Mass Fraction with Velocity in the Precursor Region; (Alt = 80 Km, V_∞ = 10, 12, 14 and 16 Km/sec) 82

Figure 53: The Variation of N_2^+ Mass Fraction with Velocity in the Precursor Region; (Alt = 80 Km, V_∞ = 10, 12, 14 and 16 Km/sec) 83

Figure 54: The Variation N Mass Fraction with Velocity in the Precursor Region; (Alt = 80 Km, V_∞ = 10, 12, 14 and 16 Km/sec) 83

Figure 55: The Variation of N^+ Mass Fraction with Velocity in the Precursor Region; (Alt = 80 Km, V_∞ = 10, 12, 14 and 16 Km/sec) 84

Figure 56: The Variation of e^- Mass Fraction with Velocity in the Precursor Region; (Alt = 80 Km, V_∞ = 10, 12, 14 and 16 Km/sec) 84

Figure 57: Geometry for the Derivation of the One-Dimensional Radiative Flux Equations 115

Figure 58: Geometry for the Derivation of the Radiative Flux from a Finite Diameter Body 122

LIST OF TABLES

Page

Table 1: Physical Constants for the Species of a Nitrogen Gas 11

Table 2: Radiative Processes Included in the Shock Layer and Precursor 38

Table 3: Atmospheric Conditions for Three Altitudes; 72 Km, 75 Km and 80 Km 51

Table 4: Freestream Conditions, Shock Standoff Distances and Radiative Fluxes 51

NOMENCLATURE

AF - Radiation attenuation factor (-)

D_i - Dissociation energy for the nth species (eV)

e - Energy per unit mass (erg/g)

e_e'' - Electron/electronic energy (erg/g)

E - Energy per particle (eV)

E_2 - Second exponential integral (-)

E_3 - Third exponential integral (-)

h - Static enthalpy (erg/g)

$h\nu$ - Photon energy (eV)

H - Total enthalpy (erg/g)

I_i - Ionization energy of the ith species (eV)

I_ν - Radiative specific intensity

k_ν' - Absorption coefficient (1/cm)

k - Boltzmann's Constant (1.38×10^{-16} erg/°K)

m_n - Mass per particle of the nth species (g)

M_n - Molecular weight of the nth species (g/Mole)

n_{BF} - Number of bound-free radiative processes

$n_{BF\ diss}$ - Number of bound-free photodissociation processes

$n_{BF\ ion}$ - Number of bound-free photoionization processes

$n_{M\text{-}band}$ - Number of molecular bands

n_s - Number of species

N_n - Number density of the nth species ($1/cm^3$)

p - Pressure (dyn/cm^2)

q - Radiative flux (W/cm^2 sec)

R - Universal gas constant (8.317×10^7 erg/°K Mole)

T - Heavy particle temperature (°K)

T_e - Electron/electronic temperature (°K)

V - Velocity in the precursor (cm/sec)

w - Mass production rate (g/cm^3 sec)

x - Spatial variable in the precursor (cm)

Y - Absorption coefficient ratio as defined in Appendix B (-)

β - One-half of the angle subtended by the body as defined in Figure 58 (degrees)

ν - Frequency (1/sec)

ρ - Density (g/cm3)

τ - Optical depth (-)

$\left(\frac{\partial q}{\partial x}\right)_M$ - Change in the radiative flux affecting the energy mode indicated by M

$\left(\frac{\partial q}{\partial x}\right)^P$ - Change in the radiative flux due to absorption or emission through the radiative process indicated by P

Subscripts

e^o	- Zero point
elct	- Electronic
i	- For the ith process
j	- For the jth electronic level
k	- At the kth spatial point
ke_{e^-}	- Free electron kinetic
n	- For the nth species
rot	- Rotational
tr	- Translational
vib	- Vibrational
∞	- Freestream values
ν	- At the frequency ν

Superscripts

$BB_{A\text{-}lines}$	- Bound-bound atomic lines
$BB_{M\text{-}band}$	- Bound-bound molecular band
BF_{diss}	- Bound-free photodissociation process
BF_{ion}	- Bound-free photoionization process
FF	- Free-free radiative process
p	- For a specific radiative process
s	- For a specific species
TS	- Using the tangent slab approximation

INTRODUCTION

The recent emphasis placed on a manned mission to Mars and the return of men and samples to earth has caused an increased interest in the development of accurate methods for predicting the fluid flow around hypersonic entry vehicles. This interest is a result of the plan to use an aerocapture technique to provide the reduction in velocity necessary to place the spacecraft in earth orbit. The benefit of this technique is that aerodynamic drag, resulting from the interaction of the spacecraft with the earth's atmosphere, instead of propulsive braking is used to slow the vehicle to orbital speeds. Such an approach provides a reduction in the fuel necessary for the mission and an increase in the return payload capabilities. The velocities experienced by a vehicle on return to earth from Mars are in the high hypersonic range, on the order of 11 Km/sec to 16 Km/sec.[1,2]

In recent years, the majority of work associated with Mars return has involved the shock layer, the region of hot gas behind the shock wave; an area which has received little attention is the shock wave precursor. The precursor is the region ahead of the shock wave in which radiation, primarily ultraviolet, emitted by the hot shock layer is reabsorbed by the gas. This absorption of radiation causes a heating of the gas in the precursor and the production of atoms as well as ions through photoionization and photodissociation reactions; these changes might also in turn affect the gas behind the shock wave. For example the preheating of the gas in the precursor as well as the introduction of electrons and ions could potentially increase the rate at which the gas

---

Format in accordance with *AIAA Journal.*

behind the shock approaches equilibrium; it has also been shown that for certain conditions the absorption of radiation ahead of the shock can cause significant increases in the radiative heating to the body.[3,4] Further, the presence of free electrons in the precursor also significantly affects communication with and identification of entry vehicles.[5,6]

The majority of the early work on precursors was performed using shock tubes and shock tunnels[5,7,8,9,10]; in this early work, there was considerable debate as to whether the electrons observed ahead of the shock wave were due to diffusion through the shock front, photoionization, or tube wall effects. However, later research by Lederman and Wilson[6] as well as by Zivanovic[11] showed that the dominant cause of these electrons was indeed photoionization. In their work, Lederman and Wilson performed shock tube tests with a venetian blind type insert in the tunnel which prevented the propagation of radiation but allowed the diffusion of electrons. With the insert in place, there were no electrons present ahead of the shock indicating that diffusion could not account for the presence of electrons in the precursor. Zivanovic performed tests in a ballistic range at velocities of up to 6.7 Km/sec, utilizing charged screens to prevent the diffusion of electrons; he found that these screens had no effect on the presence of electrons ahead of the shock.

Another work of particular interest to this study was performed by Omura and Presley[12,13]. They conducted a shock tube study of the electron densities ahead of strong shock waves in nitrogen as well as in air mixtures. These studies by Omura and Presley are, to the authors knowledge, the only actual measurements made of the

precursor in air. In this work, Omura and Presley placed plastic filters in the shock tube to prevent the propagation of ultraviolet radiation. With these filters in place, there were no electrons present ahead of the shock wave; therefore showing that the precursor was due to photoionization of the gas resulting from the absorption of ultraviolet radiation.

In the late sixties and early seventies, a number of analytical and computational studies were made in an attempt to model the precursor. Murty[14] performed a study that included the effects of the absorption of line radiation in the precursor in a hydrogen gas and Nelson[15,16] calculated the degree of ionization and excitation in the precursor ahead of a shock wave in an argon gas. Also, a number of studies including various effects were made by Clarke et al. for argon and hydrogen gases.[17,18,19]

Finally, the most recent work in shock wave precursors was by Tiwari and Szema.[20,21] In this work, they calculated the effect of the precursor on the shock layer and the radiative heating on a body entering into the atmosphere of Jupiter, which is composed of hydrogen.

The purpose of the research described herein was to develop a technique for predicting the character and magnitude of the shock wave precursor ahead of an entry vehicle and to ascertain the effect of this precursor on the vehicle flow field. In order to accomplish this task, a computational method and program were developed to properly model the precursor. As part of this research, expressions were developed for the mass production rates of each species due to the photodissociation and photoionization reactions. Also, consideration was given to the absorption and emission of radiation and how it affects the energy in each of the energy modes of both the atomic and diatomic

species. Subsequently, a series of parametric studies were conducted covering a range of entry conditions in order to predict the effects of the precursor on the shock layer and the radiative heat transfer to the body.

For this research, a nonequilibrium chemistry viscous shock layer (VSL) program developed for NASA[22] and modified extensively by Carlson and Gally[23] was used to predict the conditions of the gas in the stagnation region behind the shock front. This program included nonequilibrium chemical reactions, multi-temperature effects, nonequilibrium nongray radiative transfer, as well as coupling between the radiation and the flow field. The radiation calculations also accounted for the fact that the excited electronic states of the atoms were not in local thermodynamic equilibrium.

The radiative transfer calculations were carried out using a revision of a program called RADICAL, originally written by Nicolet[24] and later improved by individuals at the NASA Langley Research Center. However, it was extensively modified at TAMU to include nonequilibrium phenomena. Further, while the tangent slab approximation was used for the radiation calculations in RADICAL; as part of this research additional expressions were derived to correct for the geometric attenuation of the radiation in the precursor. RADICAL was also changed to include certain radiative processes which were present in the cold gas of the precursor but excluded in the original revision. The properties of the gas in the precursor were calculated using the one-dimensional Euler equations in conjunction with the radiation transfer calculations of RADICAL. For this study, the earth's atmosphere was modeled as a nitrogen gas. These calculations

accounted for the production of each species by radiative reactions as well as thermal nonequilibrium between the electrons and heavy particles.

PRECURSOR FORMULATION

As shown in Figure 1, the flow around a high velocity entry vehicle can be divided into several regions. Immediately behind the shock front, there is a highly nonequilibrium region dominated by collisional chemical reactions, in which the shocked gas relaxes toward to chemical and thermal equilibrium. Following the relaxation region are the near equilibrium and the equilibrium regions, where, as suggested by the names, the gas is close to or in thermal and chemical equilibrium. In these regions, the gas cools due to the emission of radiation. Finally, as the gas approaches the body, it enters the viscous or thermal boundary layer where, due to the cold vehicle surface, the gas temperature rapidly decreases with a subsequent increase in the density.

A portion of the radiation emitted in the hot near equilibrium and equilibrium regions of the shock layer propagates into the region of cool gas ahead of the shock, where part of the radiation is absorbed. This radiation absorbed ahead of the shock wave, referred to as "trapped radiation", causes a heating as well as excitation, photoionization and photodissociation of the cool gas. This region of cool perturbed gas ahead of the shock wave is the precursor. Due to the precursor, the shock wave propagates into an excited, ionized and partially dissociated gas.

Thus, the shock wave precursor is a nonequilibrium region dominated by the absorption of radiation and subsequent photoreactions. However, with the relatively low temperatures in this region the collisional reactions have little influence on the gas in comparison to the photoreactions; likewise, the viscous effects in this region are negligible. As discussed previously, there was originally some confusion as to the

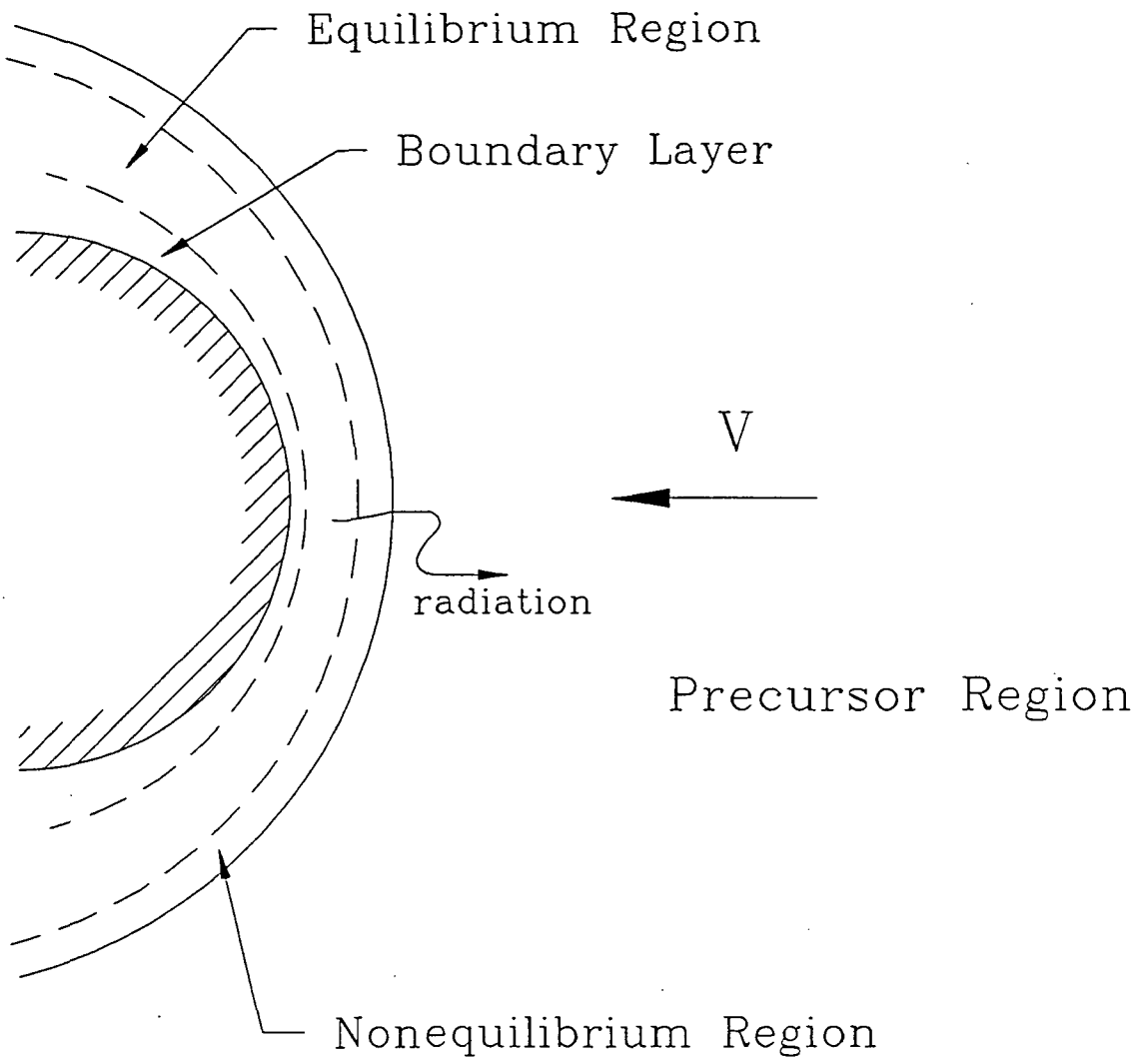

Figure 1: Nonequilibrium Shock Wave Structure

importance of diffusion in the precursor. Very near the shock wave, the effects of electron diffusion from the highly ionized gas behind the shock might be of importance; however, on the distance scale associated with the absorption of radiation and the photoionization and photodissociation processes, the effects of electron diffusion are negligible.

The dominant absorption processes in the cool precursor ahead of a vehicle entering the earth's atmosphere are the photoionization and photodissociation of molecular oxygen and nitrogen involving continuum radiation. Photoionization due to continuum radiation for atomic oxygen and nitrogen are also present to a lesser extent. The atomic photoprocesses are not as prevalent as the molecular continuum due to the relatively low population of atomic species compared to the molecular species. Likewise, atomic line absorption is also small compared to the continuum absorption. This behavior differs from several previous precursor studies which showed significant absorption through the atomic lines.[14,16,25] However, these studies were performed in monatomic gases in which the atom concentrations were high.

In cool air, noticeable absorption of radiation begins at energies greater than approximately 6.7 eV. This absorption takes place in the Schumann-Runge band system of molecular oxygen[26] and the absorption cross section for this process is of the order 10^{-18} cm^2 [27]. At 7.05 eV, continuum processes associated with the dissociation of oxygen become important and at frequencies above 8.55 eV, the Lyman-Birge-Hopfield band of molecular nitrogen absorbs radiation[28]. However, this molecular band corresponds to a forbidden transition, $a^1\Pi_g$ to $X^1\Sigma_g^+$ and is thus relatively weak, having

cross sections on the order of 10^{-21} cm^2 [29]. At frequencies above 9.76 eV, absorption occurs through continuum processes associated with the dissociation of molecular nitrogen through predissociation out of the excited $a^1\Pi_g$ state[26]. This process will be discussed in further detail in the section on radiative processes.

Photons with energies exceeding the ionization energy from the ground state of the oxygen and nitrogen molecules (I_{O2}= 12.1 eV, I_{N2}= 15.59 eV) are also absorbed strongly in cool air. The absorption cross sections for these two processes are of the order 10^{-18} cm^2 and change very little with frequency[27].

Gas Model

For this preliminary study, the earth's atmosphere was modeled as pure nitrogen rather than a nitrogen oxygen mixture. This approach is a common simplifying assumption when performing nonequilibrium, hypervelocity flow field calculations since the atmosphere is predominately nitrogen. In dealing with the precursor, however, the primary concern was whether or not the absorption processes of nitrogen sufficiently model those of air. After careful consideration it was decided that due to the predominance of nitrogen in the atmosphere it would be reasonable to represent the atmosphere as nitrogen in this initial study.

The effects of thermal nonequilibrium in the precursor were included in this study by permitting the free electrons and heavy particles to have different temperatures. Further, it was assumed, that the free electrons and the electronic states were in equilibrium at a common temperature, which as discussed by Nelson and Goulard[15], is

one of the limiting cases for the precursor. For this region of the gas, the temperature governing the electronic states would normally be expected to be greater than the heavy particle temperature but less than the electron temperature; thus, ideally a three temperature model should be used allowing a separate electronic temperature. Nevertheless, since the mechanisms and expressions for the transfer of energy between the electronic states and the free electrons are not known or well understood, it was decided to use only a two temperature model. However, in order to correct for the local thermodynamic nonequilibrium between the electrons and the electronic states, a collision limiting correction[30] was applied to the populations of the molecular electronic states when computing radiative emission and absorption phenomena.

For this study, the mass production rates in the precursor zone due to collisional reactions were neglected in comparison to those due to photoreactions. The photoreactions used in this study included the dissociation of molecular nitrogen and the ionization of both molecular and atomic nitrogen, i.e.

$$N_2 + h\nu \rightleftharpoons^{k_{v1}'} 2N$$
$$N_2 + h\nu \rightleftharpoons^{k_{v2}'} N_2^+ + e^-$$
$$N + h\nu \rightleftharpoons^{k_{v3}'} N^+ + e^-$$

The physical constants for the five species included in this study are given in Table 1; also, the elastic collisional terms in the electron/electronic energy equation were evaluated using the collisional cross sections of Gnoffo, Gupta and Shinn[31].

The effects of the absorption of radiation through free-free and bound-bound processes were also included in this study. While these processes do not cause chemical

Table 1: Physical Constants for the Species of a Nitrogen Gas

Species	M (g/Mole)	e°_n (erg/g)	D (eV)	θ^{vib} (°K)	Elect level	I_m (eV)	θ_m^{elct} (°K)	g_m
N_2	28.014	0.0	9.78	3390.0	1	15.59	0.0	1
					2	9.42	71,592.0	3
					3	8.24	85,343.0	6
					4	-	99,212.0	2
N_2^+	28.014	5.3703×10^{11}	-	3390.0	1	-	0.0	2
					2	-	13,191.0	4
					3	-	36,634.0	2
					4	-	92,977.4	2
N	14.007	3.3689×10^{11}	-	-	1	14.3	0.0	4
					2	12.0	27,670.0	10
					3	10.8	41,496.0	6
					4	-	121,300.0	18
					5	-	137,900.0	54
					6	-	150,900.0	90
N^+	14.007	1.3221×10^{12}	-	-	1	-	0.0	1
					2	-	70.5	3
					3	-	188.5	5
					4	-	22,036.5	5
					5	-	47,029.7	1
					6	-	67,864.8	5
e^-	5.4847×10^{-4}	0.0	-	-	-	-	-	-

reactions, they do cause an increase in the energy of the gas and their effects must be included in the electron/electronic energy equation. Absorption through atomic lines was neglected due to the expected low concentration of atomic species.

Governing Equations

As discussed above, the precursor is a region of the gas in both thermal and chemical nonequilibrium which is governed by the absorption of radiation, in which collisional chemistry and viscous effects are negligible compared to the radiative effects. The shock layer, on the other hand, is dominated by the radiative and viscous phenomena, as well as collisional chemistry effects. Due to this basic difference between the important aspects of these regions, it is efficient to calculate the flow field for each region separately. In this way, the viscous and collisional chemistry effects need not be calculated for the precursor where they are relatively unimportant.

While the precursor is coupled strongly to the shock layer through radiation, the precursor is expected to affect the shock layer only slightly. In this study, the nonequilibrium radiation coupled shock layer flow field was first calculated assuming that the conditions ahead of the shock front were unperturbed. Then the resulting shock layer flow field was used to determine the radiative flux through the shock front and, using an iterative procedure, the precursor flow field as well as the radiation absorbed by the gas in the precursor. Finally, the precursor results were then used as freestream conditions for the calculation of a new shock layer solution to find the effects of the precursor on the shock layer. The methods used for the radiation and shock layer calculations will be

discussed in detail in other sections of the text. The remainder of this section will deal with the calculation techniques for the precursor region.

The equations governing the fluid properties on the stagnation streamline in the precursor are the steady, one dimensional, nonequilibrium Euler equations. The basic one dimensional Euler equations are:

Global Continuity

$$\frac{\partial}{\partial x}(\rho V) = 0 \tag{1}$$

Momentum

$$\rho V\frac{\partial V}{\partial x} + \frac{\partial p}{\partial x} = 0 \tag{2}$$

Energy

$$\rho V\frac{\partial H}{\partial x} + \frac{\partial q}{\partial x} = 0 \tag{3}$$

In equation (3), H is the total enthalpy of the gas defined in terms of the static enthalpy such that

$$H = h + \frac{1}{2}V^2 \tag{4}$$

where

$$h = \frac{p}{\rho} + \sum_{n=1}^{n_s}(e_{tr_n} + e_{rot_n} + e_{vib_n} + e_{elct_n} + e_n^o) \tag{5}$$

The second term in equation (3) is the gradient of the radiative flux. This term accounts for the increase or decrease in the energy of the gas due to absorption and emission of

radiation. In addition to these equations, the equation of state for a two temperature gas is required,

$$p = \rho \hat{R} T \sum_{n=1}^{n_s} \left(\frac{\rho_n}{\rho} \frac{1}{M_n} \right) + \rho \frac{\hat{R}}{M_{e^-}} \frac{\rho_{e^-}}{\rho} (T_e - T) \tag{6}$$

To allow for the effects of thermal nonequilibrium, an electron/electronic energy equation was added to these equations,

$$\begin{aligned} \frac{\partial}{\partial x}(\rho V e_e'') = & -p_e \frac{\partial V}{\partial x} + \sum_{n=1}^{n_s} \xi_{e,n} + \dot{w}_e \frac{V^2}{2} - \frac{\partial q}{\partial x} \\ & + \sum_{i=1}^{n_{diss}} \int_0^{\infty} \frac{Y_{\nu_i}^p (h\nu - \Delta E_{elct_i} - D_i)}{h\nu} \frac{\partial q_\nu}{\partial x} d\nu \\ & + \sum_{i=1}^{n_{mb}} \int_0^{\infty} \frac{Y_{\nu_i}^p (h\nu - E_{elct_i}^{upp} + E_{elct_i}^{low})}{h\nu} \frac{\partial q_\nu}{\partial x} d\nu \end{aligned} \tag{7}$$

where

$$e_e'' = \frac{\rho_{e^-}}{\rho} e_{e^-} + \sum_{n=1}^{n_s} (e_{elct_n} + e_n^o) \tag{8}$$

In this equation, e_{e^-} is the kinetic energy of the free electrons, $3/2\ kT_e/m_{e^-}$, while $e_{elct\,n}$ and e_n^o are the electronic and zero point energies of the nth species. The last three terms on the right hand side of equation (7) allow for the effects of the absorption of radiation. This equation is derived in detail in Appendix A.

Chemical nonequilibrium was accounted for in the precursor through the addition of a species continuity equation for each of the five species in the problem. These equations are of the form

$$\rho V \frac{\partial\left(\frac{\rho_n}{\rho}\right)}{\partial x} = -m_n \int_0^\infty \frac{Y^s_{\nu_n}}{h\nu} \frac{\partial q_\nu}{\partial x} d\nu \tag{9}$$

where

$$Y^s_{\nu_{N_2}} = -\frac{k'_{\nu_1} + k'_{\nu_2}}{k'_{\nu_{tot}}} \qquad Y^s_{\nu_{N_2^+}} = \frac{k'_{\nu_2}}{k'_{\nu_{tot}}}$$

$$Y^s_{\nu_N} = \frac{2k'_{\nu_1} - k'_{\nu_3}}{k'_{\nu_{tot}}} \qquad Y^s_{\nu_{N^+}} = \frac{k'_{\nu_3}}{k'_{\nu_{tot}}} \tag{10}$$

$$Y^s_{\nu_{e^-}} = \frac{k'_{\nu_3} + k'_{\nu_2}}{k'_{\nu_{tot}}}$$

The term on the right hand side of equation (9) is the mass production rate of the nth species due to photoprocesses and is derived in Appendix B. The absorption coefficients, $k'_{\nu 1}$, $k'_{\nu 2}$ and $k'_{\nu 3}$ are those for the absorption and emission processes associated with each of the three photochemical reactions in the previous sections.

In all of the above equations, the radiative terms, $\partial q/\partial x$, are the changes in the radiative flux due only to the absorption of radiation and not those due to the geometry of the problem. These terms will be discussed in further detail later in the text.

Solution Scheme

The equations above are solved using a space marching technique starting at a point far from the shock front and marching in towards the shock wave. The point furthest from the shock wave was assumed to be far enough from the radiating shock layer that the ultraviolet radiation was absorbed between this point and the shock; thus, the gas properties at this point were forced to remain at the freestream conditions. The spacing between each spatial point was adjusted as the solution progressed so that the change in the flow properties between each point was greater than a preselected minimum value but less than a selected maximum value. This procedure forced a high concentration of points in the regions of large gradients and allowed the distance between points to increase in the regions of small gradients.

At each individual point, the above equations were solved using an iterative process. For this iterative procedure, equations (1), (2) and (3) were integrated analytically from point, *k-1*, in the flow field to the next point, *k*, to give the following form:

Continuity

$$\rho_k = \frac{\rho_{k-1} V_{k-1}}{V_k} \tag{11}$$

Momentum

$$V_k = V_{k-1} + \frac{p_{k-1} - p_k}{\rho_{k-1} V_{k-1}} \tag{12}$$

Energy

$$H_k = H_{k-1} + \frac{q_{k-1} - q_k}{\rho_{k-1} V_{k-1}} \tag{13}$$

As previously mentioned, the change in the radiative flux in the energy equation from point *k-1* to point *k* is only that due to absorption and emission.

The iterative scheme at each point, *k*, began by assuming that the flow properties are the same as those at the previous point, *k-1*. Then, the analytic expressions for the continuity, momentum and energy equations (11), (12) and (13) were used to calculate new values for the density, velocity and total enthalpy, respectively. Subsequently, the static/total enthalpy relation, equation (4), was used to calculate a new value for the static enthalpy and the integral expressions for the species concentrations, equation (9), were integrated from the spatial point *k-1* to the spatial point *k* using a fourth order Runge-Kutta (RK) integration scheme. Similarly, the electron/electronic energy equation was also integrated using the RK-4 scheme. At this point, the static enthalpy and electron/electronic energy expressions, equations (5) and (8), were solved for the heavy particle and electron/electronic temperatures, respectively. Finally, the equation of state was solved for the new pressure.

At this point, the change in each of the fluid properties between the new and the original values was calculated. If this change was greater than a selected convergence requirement, then the steps outlined above were repeated until the change in the properties through one iteration was within the convergence requirement. After the fluid properties at a point were calculated, the changes between the current point and the

previous point were calculated. If these changes were not within the maximum and minimum requirements selected then the spatial step size was increased or decreased, whichever was appropriate, by a factor of two and the process was repeated for this spatial point. If, on the other hand, the changes were within the maximum and minimum requirements, then the values for the current point were saved and the current spatial step size was used to move to the next point where the above process was repeated.

RADIATION FORMULATION

In most of the previous work investigating shock wave precursors, there have been several assumptions imposed on the calculation of the radiative transfer. In some cases it was assumed that the shock layer emitted radiation as a black body at the equilibrium temperature behind the shock front.[14,25,32,33] However, the radiative flux passing through the shock front from the nonequilibrium shock layer is considerably less than that predicted by the black body assumption; therefore, the use of the black body assumption can lead to the prediction of larger changes in the precursor than are actually present. Similarly, several of the previous works used a multiple step absorption coefficient model[1,20,34] where at a given temperature the species radiative properties are assumed constant over specific frequency regions. Some researchers, such as Lasher and Wilson[3], have ignored the spectral details entirely. However, since the precursor region is dominated by the photochemical reactions, variations in the radiative transfer might cause significant changes in the precursor. Likewise, the spectral details are very important in the precursor calculations since there are a number of important radiative processes which occur over different frequency ranges and the frequency of the photon absorbed as well as the process through which it is absorbed directly affects how the photons energy changes the energy of the gas. Without sufficient spectral detail, it is not possible to ascertain what portion of the radiation absorbed causes photoionization or photodissociation and what portion simply causes an increase in the internal energy of the gas.

Equations of Radiative Transfer

Because of the necessity for accurate radiation predictions for the calculation of the precursor conditions, it was decided that a complete spectrally detailed method of calculating the radiative flux was in order. Thus, an extensively modified version of the program RADICAL was utilized. RADICAL, which was originally created as a method of predicting the radiative transport through the boundary layer of ablating entry vehicles, is also suitable for the calculation of the radiative flux through the entire shock layer. This program allows the user to select the frequency points to be used for the continuum radiation, so it was possible to obtain the spectral detail necessary for accuracy in the precursor calculations. RADICAL also performs detailed calculations of the atomic line radiation.

RADICAL, like many of the schemes currently used in the calculation of radiative transfer, uses the tangent slab approximation. This assumption is a one-dimensional approximation of the full equation of radiative transfer. Basically, it treats the radiation emitted at a point in the gas as if it were emitted by an infinite plane of gas positioned perpendicular to the direction of travel of the radiation; this can be seen in Figure 2. By this assumption, the radiation emitted by the point, A, in the shock layer is treated as if it were emitted by the plane shown. As can be seen in this figure, this is a good approximation if we consider only the shock layer ahead of a blunt body. Since the thickness of the shock layer is much smaller than the body dimensions, each point in the shock layer is positioned close enough to the body that the rest of the gas in the radiating shock layer indeed appears to be of infinite extent. For the conditions of interest in this

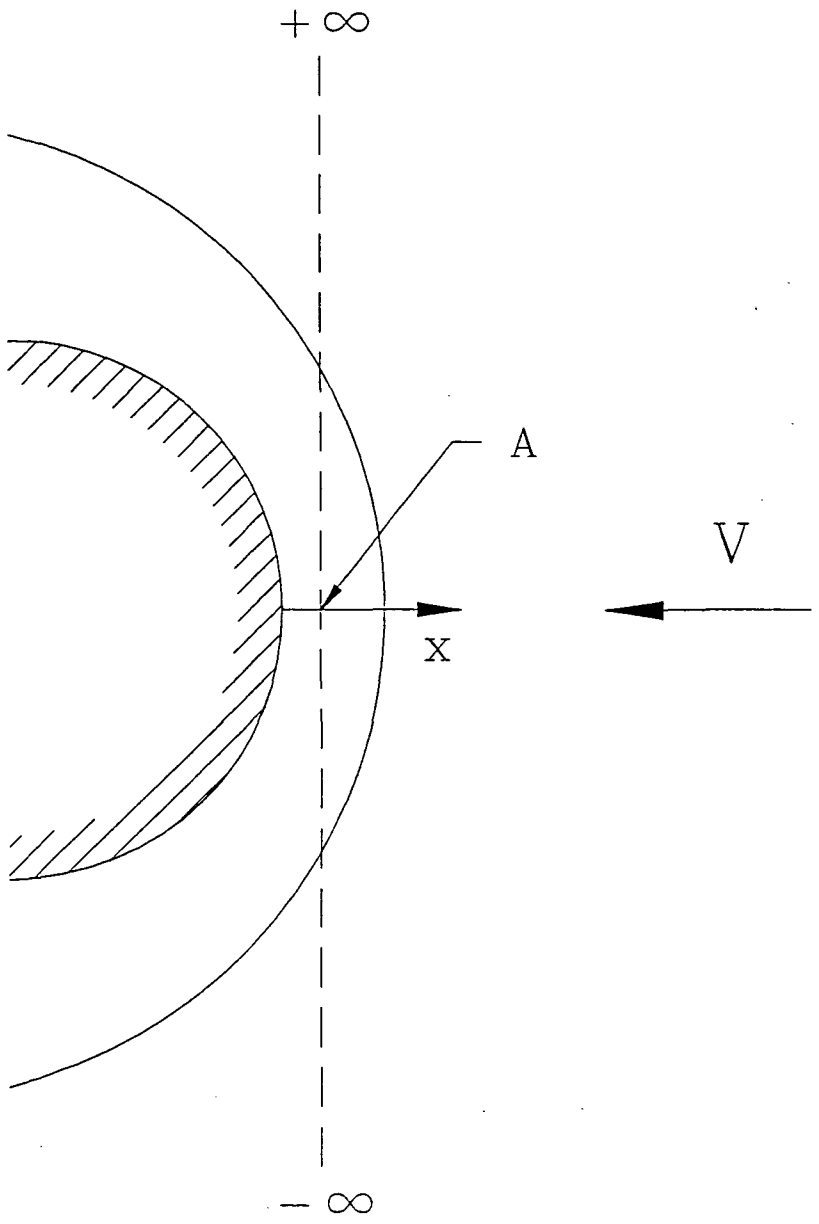

Figure 2: Geometry Associated with the Tangent Slab Approximation

study, the distance between the shock and the body on the stagnation streamline is on the order of 10 cm while the diameter of the body is 230 cm.

The precursor, however, can extend to distances ahead of the shock on the same order of magnitude as the body diameter. For the conditions in this study, the precursor extends to distances on the order of 150 cm ahead of the shock. Therefore, in the precursor, the radiating shock layer no longer appears to be of infinite extent but instead appears to be a slab of finite diameter.

In the one-dimensional problem, as in the shock layer, absorption is the only method by which the radiation is attenuated as it travels through the gas. Therefore, any decrease in the radiative intensity through the gas can be attributed to absorption, which in turn causes an increase in the energy of the gas equal to the decrease in the radiative energy. However, since the shock layer does not appear to be of infinite extent at each point in the precursor, the radiation no longer behaves one-dimensionally; consequently, in the precursor region the radiative transfer is a three-dimensional problem in which a decrease in the radiative intensity can occur because of the geometry of the problem as well as absorption.

This effect can be better understood by considering a plane of radiating gas. In the one-dimensional problem this plane is of infinite extent and the radiative intensity will be constant at all points on a plane parallel to the radiating plane. However, in the case where the radiating plane is not of infinite extent, the radiative intensity on a plane parallel to the radiating disk will be a maximum on the centerline of the disk and will

decrease moving radially outward from this centerline. This attenuation of the radiation radially is due strictly to the geometry.

Similarly, the radiation will attenuate faster in the direction perpendicular to a finite radiating disk than it would moving away from an infinite radiating slab. As shown in Figure 3a, the radiation emitted from an infinite slab travels only in the direction perpendicular to the slab. Therefore, since the radiative flux, q, is the quantity of radiative energy passing through a unit area, if there is no absorption the radiative flux will remain constant in the direction perpendicular to the radiating slab. This is a result of the fact that the radiative energy emitted in a unit area of the slab will continue to pass through the same area as it progresses perpendicular to the slab. However, for the case of a finite radiating slab there will be a decrease in the radiative flux moving in the direction perpendicular to the slab even though there is no absorption. This decrease is a result of the fact that the energy emitted from a finite slab will radiate evenly into the 180 degree semi-sphere as shown in Figure 3b; therefore, as the energy emitted by this slab progresses outward the area through which it passes will increase, thus producing a decrease in the radiative flux. This decrease, however, since not due to absorption by the gas has no effect on the gas through which it passes. Therefore, in the case of a finite slab, the radiative flux will decrease due to both absorption and geometric attenuation. However, only the decrease due to absorption will cause an increase in the energy of the gas.

In order to use RADICAL for the radiation calculations, it was necessary in the precursor to correct for the geometric attenuation of the radiation. The one-dimensional

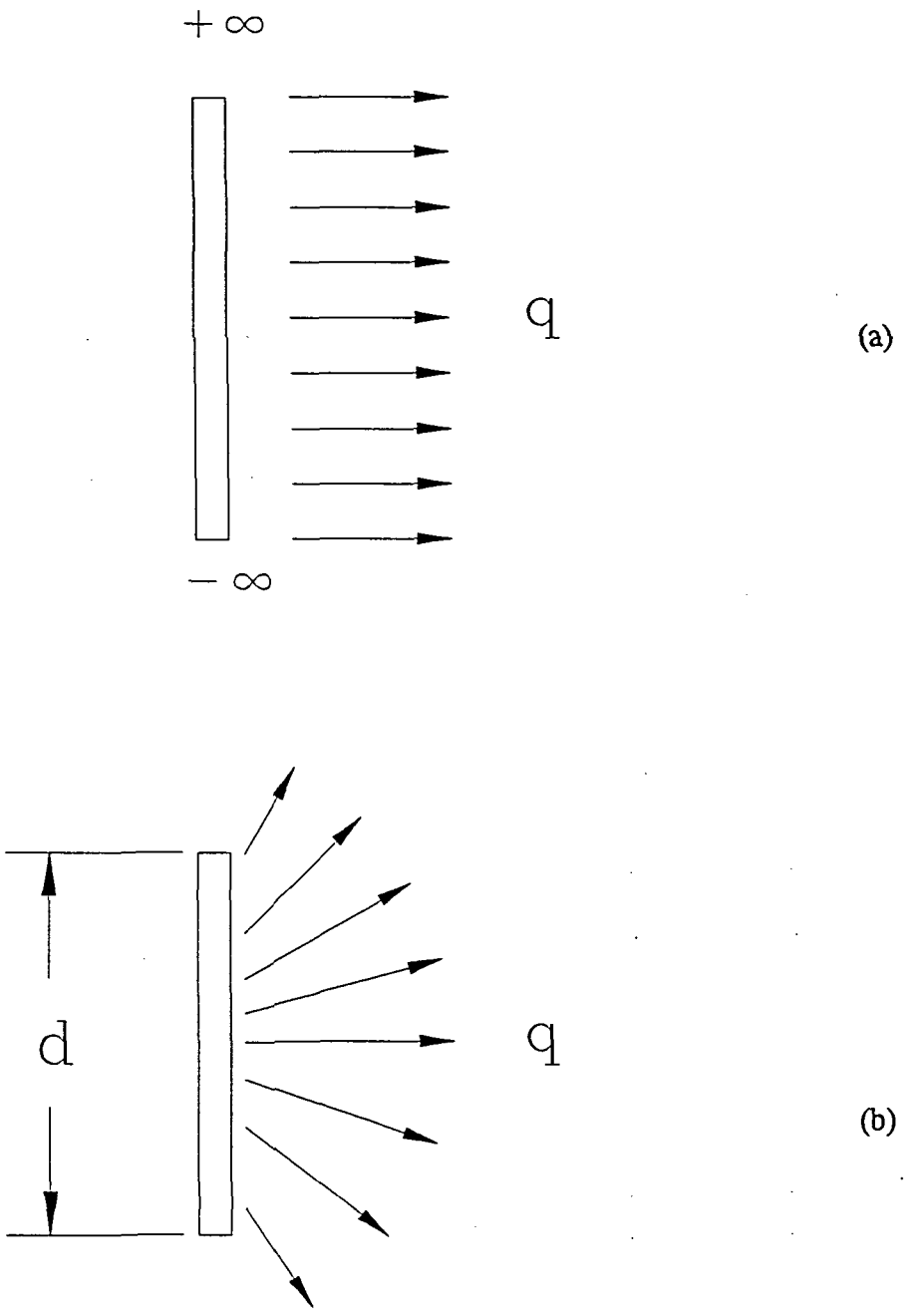

Figure 3: Propagation of Radiative Energy from Finite and Infinite Slabs

equation of radiative transfer resulting from the tangent slab approximation is

$$q_\nu^{TS} = 2\pi I_\nu^{wall} E_3(\tau_\nu) + 2\pi \int_0^{\tau_\nu} S_\nu E_2(\tau_\nu - \tau_\nu') d\tau_\nu' - 2\pi I_\nu^{\infty} E_3(\tau_\nu^{\infty} - \tau_\nu) \\ - 2\pi \int_{\tau_\nu}^{\tau_\nu^{\infty}} S_\nu E_2(\tau_\nu' - \tau_\nu) d\tau_\nu' \tag{14}$$

In this equation, the first term is the radiative flux away from the wall, the second term is the radiative flux due to the gas between the wall and the current point of interest, the third term is the radiative flux from infinity and the fourth term is that due to the gas between the point of interest and infinity.

If we assume that the point of interest is in the precursor and that the radiation emitted in the precursor is negligible, this equation reduces to

$$q_\nu^{TS} = 2\pi I_\nu^{wall} E_3(\tau_\nu) + 2\pi \int_0^{\tau_\nu^s} S_\nu E_2(\tau_\nu - \tau_\nu') d\tau_\nu' \tag{15}$$

The first term here, as above, is that due to the radiative flux from the wall and the second term in this equation is due to the gas in the hot radiating shock layer.

The equivalent equation assuming that the radiation emitted at each point is due to a finite diameter slab is

$$q_\nu = 2\pi I_\nu^{wall} E_3(\tau_\nu) \left[1 - Cos^2(\beta) \frac{E_3(\tau_\nu Sec(\beta))}{E_3(\tau_\nu)} \right] \\ + 2\pi \int_0^{\tau_\nu^s} S_\nu E_2(\tau_\nu - \tau_\nu') d\tau_\nu' \left[1 - Cos^2(\beta) \frac{E_3((\tau_\nu - \tau_\nu^s) Sec(\beta)) - E_3(\tau_\nu Sec(\beta))}{E_3(\tau_\nu - \tau_\nu^s) - E_3(\tau_\nu)} \right] \tag{16}$$

Comparing this equation and the one above, it can be seen that they are identical except for the terms in brackets which are dependent on the vehicle size and the location of the point of interest. These terms are essentially attenuation factors which correct each term in the tangent slab equation for the geometric attenuation associated with a finite slab. In this equation, the first bracketed term is the attenuation factor associated with the wall radiation and the second is that associated with the radiation from the shock layer.

As discussed previously, the dominant absorption processes in the precursor are those causing photoionization and photodissociation of the gas, which occur in the ultraviolet frequency range. Since the radiation from the wall is in the infrared frequency range, it was expected to have little effect on the gas in the precursor. Therefore, for this study the shock layer attenuation factor was applied to all of the radiative terms. It is believed that this is a reasonable engineering approximation and should have minimal effect on the results of this study. Utilizing this attenuation factor, the radiative flux in the precursor can be expressed as

$$q_\nu = AF_\nu \, q_\nu^{TS} \tag{17}$$

where AF_ν is the attenuation factor and q_ν^{TS} is the radiative flux at the point using the tangent slab approximation.

In the species continuity and energy equations, the terms involving the radiation appear as a divergence of the flux and are defined to account for the absorption and emission of radiation at a point. However, simple differentiation of equation (17) yields

$$\frac{\partial q_\nu}{\partial x} = AF_\nu \frac{\partial q_\nu^{TS}}{\partial x} + q_\nu^{TS} \frac{\partial AF_\nu}{\partial x} \tag{18}$$

In this expression, the first term on the right hand side is the change in the radiative flux due to the emission and absorption of radiation, but the second term is the change due to the geometry of the problem and should not affect the gas. Thus, it is neglected. Notice that if the second term was included in the species continuity and energy equations, an essentially transparent radiation would appear to be absorbed due to the spatial variation of the attenuation factor.

A detailed derivation of the equations in this section is given in Appendix C.

Radiative Processes

In order to properly account for the effects of absorption and emission of radiation on the energy of a gas, it is necessary to have an understanding of how each radiative process physically changes the particles involved. The effects of the absorption and emission of radiative energy on the internal energy modes depends on the type of radiative process involved as well as the frequency of the photon absorbed or emitted. Radiative processes can be separated into three categories: free-free, bound-bound and bound-free. While the free-free and bound-bound processes cause an increase in the energy of the gas with no chemical change, the bound-free processes are associated with chemical reactions in the gas, such as photoionization or photodissociation.

Free-free or Bremsstrahlung emission and absorption involves a free electron passing near a positive ion. This electron while passing through the coulomb field of the ion can emit radiative energy and through this processes suffer a decrease in kinetic energy. Similarly, the electron can absorb a photon of radiative energy which causes an

increase in its kinetic energy. It follows that the emission and absorption of radiative energy through the free-free process affects only the kinetic energy of the free electrons. Since there is no restriction on the kinetic energy which can be lost or gained by an electron, this is a continuous process and can produce photons at any frequency.

Bound-bound emission and absorption is associated with a change in the internal energy state of the particle involved. In atoms, bound-bound emission and absorption is associated with a change in the electronic energy state of the atom; thus, emission and absorption of "line" radiation by atoms only affects the electronic energy of the gas. Since the electronic states are quantized and transitions between certain states are restricted due to quantum mechanical considerations, these bound-bound transitions only affect discrete frequencies.

The emission and absorption of radiation due to bound-bound transitions in molecules is similar to that in atomic transitions. However, since molecules have three distinct modes of internal energy storage, electronic, vibrational and rotational, each or all can be affected by the emission and absorption of radiation. As with atoms, the absorption or emission of radiation by a molecule causes a change in the electronic state of the molecule. However, within each electronic state of a molecule there are a number of vibrational levels, as well as a number of rotational states within each vibrational level. Bound-bound molecular transitions involve a change from the original electronic, vibrational and rotational states to a new set of states and although the electronic state must always change, the vibrational and rotational states could feasibly remain unchanged.

Bound-bound molecular radiation is generally grouped into distinct bands. Each molecular band is associated with a transition between a pair of electronic states. However, these transitions can originate from any vibrational/rotational combination within the original electronic state and can end with certain restrictions governed by a set of quantum mechanical rules in almost any vibrational/rotational combination within the final electronic state. Since the internal energy states are quantized, the radiation associated with each pair of original and final vibrational/rotational combinations appears at distinct frequencies and causes lines as in atomic bound-bound transitions. However, due to the large number of possible vibrational/rotational combinations within each electronic state, these lines tend to overlap and in most cases can be treated as a continuum process which occurs within a limited frequency range. Figure 4 is an energy diagram for the nitrogen molecule and shows the well known molecular bands of this molecule.

The balance of energy in a molecule emitting or absorbing radiation through a molecular band is given by

$$E_{elct}^{low} + E_{vib}^{low} + E_{rot}^{low} + h\nu = E_{elct}^{upp} + E_{vib}^{upp} + E_{rot}^{upp} \qquad (19)$$

In this equation, the "low" values are the values for the lower energy state before the absorption of the photon and the "upp" values are those for the upper energy state after the absorption of the photon. If it is known through which molecular band the photon is absorbed, the difference between the final and initial electronic energies of the molecule, $\Delta E_{elct}=E_{elct}^{upp}-E_{elct}^{low}$, is known from knowledge of the two electronic states involved. The change in the individual vibrational and rotational energies can not easily

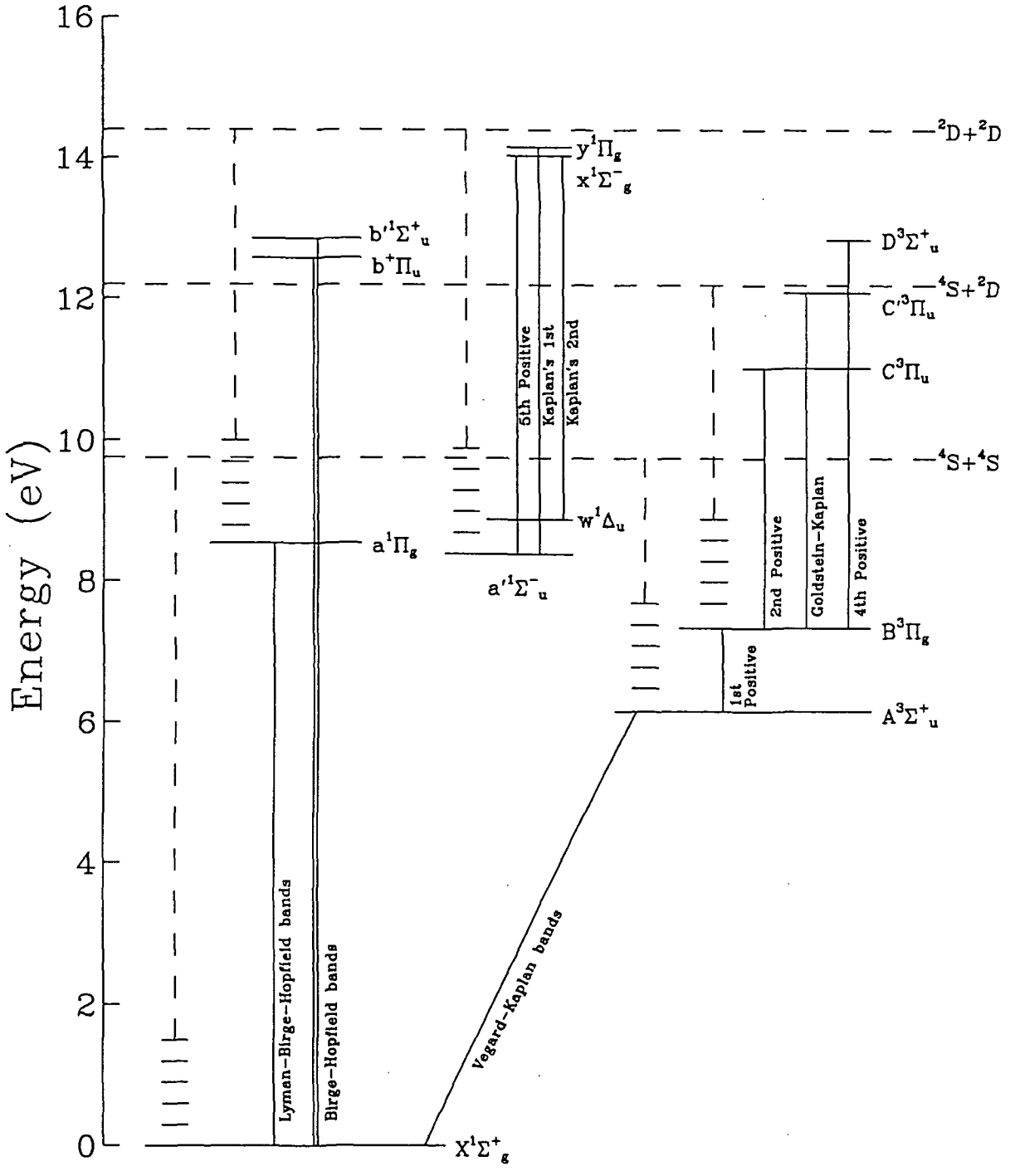

Figure 4: Energy Diagram for Molecular Nitrogen

be determined without knowing the exact upper and lower energy levels of the two energy modes associated with the particular frequency of the absorbed photon. However, the sum of the changes in these two modes can easily be obtained by manipulating the above equation to give

$$\Delta E_{vib} + \Delta E_{rot} = h\nu - \Delta E_{elct} \tag{20}$$

If the vibrational and rotational terms can be considered together, then the effects of absorption on these modes can be found using this relation.

As previously mentioned, bound-free radiative processes are associated with photochemical reactions within the gas. As with free-free emission and absorption, the bound-free transitions are continuum processes. However, since the chemical reaction associated with a bound-free process requires a finite quantity of energy to occur, each bound-free process will have a lower limit on the frequency of photon which can be emitted or absorbed which corresponds to the energy required for the chemical reaction. Since the bound-free processes can emit or absorb photons of any frequency above this lower limit, they are continuum processes. Bound-free radiative processes can be divided into two groups depending on the type of chemical reaction involved, photoionization or photodissociation. The effects of photoionization on the gas will first be considered.

While each species has one specific value for the ionization energy, the photon energy necessary for photoionization is dependent upon the electronic state of the particle absorbing the photon. Thus, the energy balance for a particle being ionized by the absorption of a photon is given by

$$h\nu + E_{elct} = I + ke_{e^-} \tag{21}$$

In this equation, $h\nu$ is the energy of the photon absorbed, E_{elct} is the electronic energy of the particle absorbing the photon, I is the ionization energy of this particle and ke_{e^-} is the kinetic energy of the electron freed in the ionization process. The limiting case which governs the minimum photon energy necessary for photoionization occurs when the freed electron has zero kinetic energy, $ke_{e^-}=0$. If the particle in this case is in the ground electronic state, $E_{elct}=0$, then the photon energy must be equal to the ionization energy of the particle. Further, if the particle is in an excited electronic state, then the photon energy required is less than the ionization energy by the energy of the electronic state of the particle and ionization from each successively higher electronic state requires decreasing photon energies. However, each successively higher electronic state is less populated; thus, the number of ionizations from the highly excited states is small. Also, as given by equation (21), if the photon energy is greater than that required the excess energy appears as kinetic energy in the departing electron.

The photoionization process affects the distribution of energy through the various energy modes in several ways. Globally the energy of the gas increases by the photon energy, $h\nu$; however, the electronic energy of the gas decreases by the quantity E_{elct} due to the loss of the electronically excited particle. This particle splits into an ion and a free electron, which requires energy I, accounted for in the zero-point energy of the created ion. Any excess energy in the process increases the kinetic energy of the free electrons through the kinetic energy of the created free electron.

Photodissociation is a slightly more complex process than photoionization in that it involves the absorption of a photon by a molecule and the subsequent splitting of the

molecule into its atomic components. The discussion herein will deal only with the photodissociation of diatomic molecules since the gas involved in this study, nitrogen, forms diatomic molecules. Figure 5 shows the potential energy curves for the nitrogen molecule.

The process of photodissociation is very similar to the absorption of radiation through the bound-bound molecular bands. As in the bound-bound process, the molecule absorbs a photon and transitions from its original electronic state to a higher state. However, if the photon absorbed is of sufficient energy the molecule will dissociate out of this upper state. If the upper electronic state in the dissociation transition has a potential well, as would be the case for a dissociation transition from the ground electronic state, $X^1\sum_g^+$, through the $A^+\sum_u^+$ excited state, then the continuum radiation associated with this transition will adjoin the bound-bound molecular band associated with these two electronic states. On the other hand, if the upper electronic state in this process is continuous, or has no potential well, the continuum radiation will be independent of any molecular band. This situation would exist for the case of a transition from one of the lower electronic states of molecular nitrogen to either the $^5\sum_g^+$ or the $^7\sum_u^+$ excited state. This is also the case if the minimum of the potential well on the upper electronic state is at a much greater internuclear distance than that of the lower electronic state. However, the nitrogen molecule does not have a potential curve representing this case.

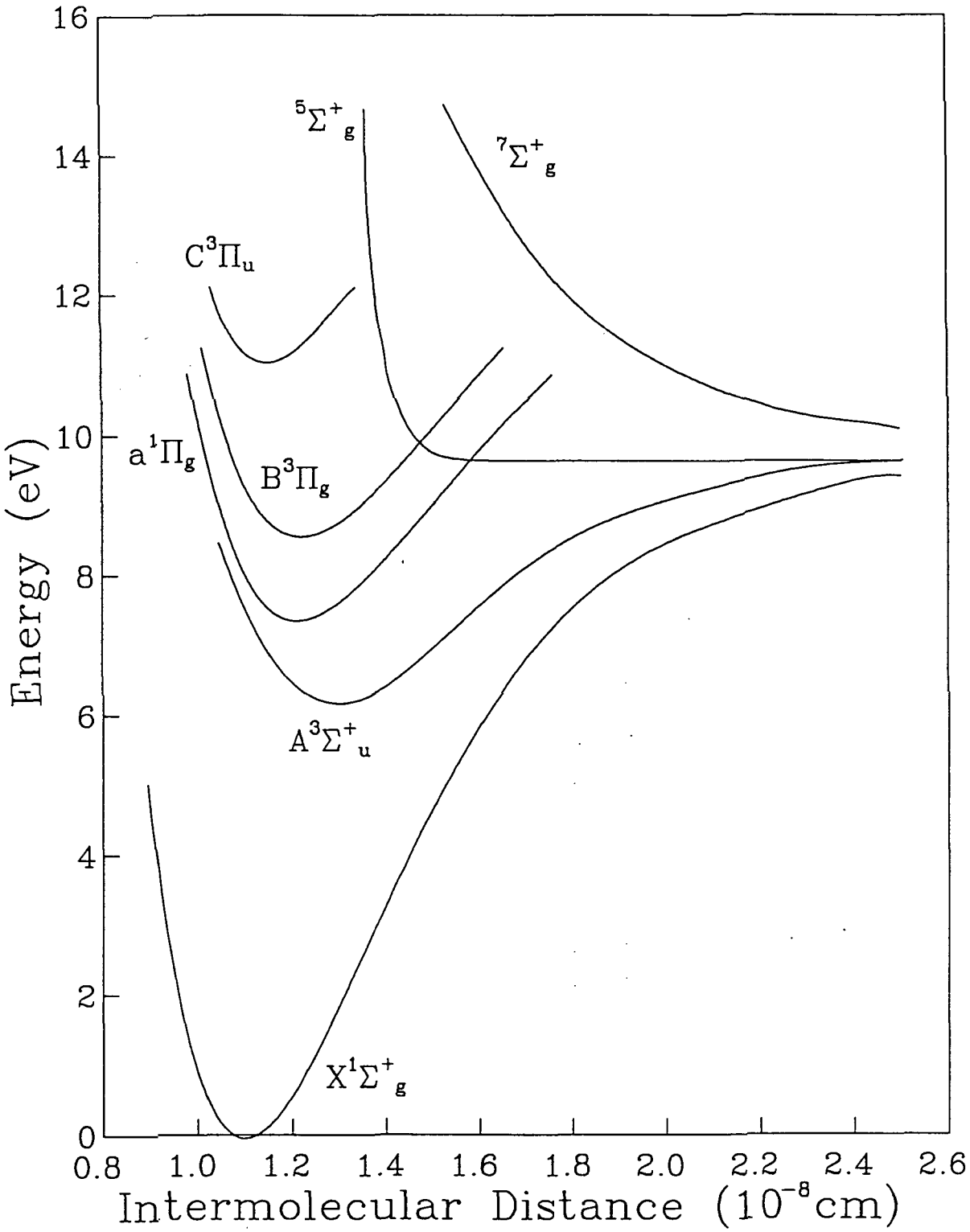

Figure 5: Potential Energy Curves for Molecular Nitrogen

The balance of energy between the initial molecule and the two atoms created in a photodissociation process is given by

$$E_{elct}^{molc} + E_{vib}^{molc} + E_{rot}^{molc} + h\nu = D + E_{elct}^{atm1} + E_{elct}^{atm2} + ke_{atoms} \qquad (22)$$

In this equation, the "molc" values are the initial values for the molecule before the absorption of the photon. The energy of the photon absorbed is $h\nu$, the dissociation energy of the molecule is D, the electronic energies of the two atoms formed are $E_{elct}^{atm\ 1}$ and $E_{elct}^{atm\ 2}$ and ke_{atoms} is the combined kinetic energy of the two atoms. In this process, the total energy of the gas increases by the energy of the photon absorbed. However, the vibrational and rotational energy modes lose energy by the quantities E_{vib}^{molc} and E_{rot}^{molc}, respectively; also, the effect of the photodissociation process on the electronic energy of the gas is given by

$$\Delta E_{elct} = E_{elct}^{atm1} + E_{elct}^{atm2} - E_{elct}^{molc} \qquad (23)$$

If it is known out of which electronic energy state the molecule dissociates, then this term can be evaluated since the electronic states of the atoms created are governed by the electronic state through which the molecule dissociates. The process of splitting the two atoms uses the quantity of energy D; this energy is accounted for in the zero point energies of the two atoms created. Finally, any excess energy above that necessary to cause the dissociation and excitation of the two atoms appears as kinetic energy of these atoms.

Photodissociation of the nitrogen molecule generally occurs through a process called predissociation,[35] which is a radiationless process in which a molecule transitions

from a discreet electronic state to a dissociated state. The Franck-Condon principle dictates that for such a transition to occur, the potential curves for the discreet and dissociated states must intersect. Therefore, if a molecule is in a discreet electronic state which intersects a dissociated state and its vibrational level is great enough that the energy of the molecule is greater than the energy at the point where the two states intersect, then the molecule will transition into the dissociated state.

Predissociation of the nitrogen molecule is known to exist from the $a^1\Pi_g$, $B^3\Pi_g$ and $C^3\Pi_u$ excited states. The $a^1\Pi_g$ and $B^3\Pi_g$ states dissociate through transitions into the repulsive ${}^5\Sigma_g^+$ state while the $C^3\Pi_u$ state dissociates through a ${}^3\Pi_u$ state which is not shown in Figure 5.[35] So, if a nitrogen molecule in the ground state absorbs a photon in the Lyman-Birge-Hopfield band with sufficient energy to place it in the $a^1\Pi_g$ state above the point of intersection with the ${}^5\Sigma_g^+$ state, then the molecule will transition into the repulsive state and dissociate into two ground state nitrogen atoms. Likewise, similar phenomena occur for a molecule in the $A^3\Sigma_u^+$ state absorbing via the 1st positive band to the $B^3\Pi_g$ state and transitioning to the repulsive ${}^5\Sigma_g^+$ state or a molecule in the $B^3\Pi_g$ state absorbing through the 2nd positive band into the $C^3\Pi_u$ state and then dissociating through the ${}^3\Pi_u$ state. All three of these dissociation processes produce two nitrogen atoms in the ground electronic state.

For the relatively cool nitrogen present in the precursor, Herzberg[26] states that dissociation occurs primarily through the Lyman-Birge-Hopfield band and the subsequent predissociation out of the $a^1\Pi_g$ state. Therefore, for this study predissociation out of the $B^3\Pi_g$ and $C^3\Pi_u$ states was neglected in an effort to reduce the numerical computations

required. It was noted during the course of this study that the absorption in the 1st and 2nd positive bands which are involved in predissociation out of the $B^3\Pi_g$ and $C^3\Pi_u$ states was negligible compared to that in the Lyman-Birge-Hopfield band.

The radiative processes included in the calculation of the emission and absorption in the shock layer and precursor are given in Table 2. The radiative processes included in the shock layer are those which were originally accounted for in the modified version of RADICAL; these processes include not only the continuum processes, but also the atomic lines associated with the nitrogen atom. Since only continuum processes were included in the precursor, the continuum mechanisms originally included in RADICAL were retained; also, the photoionization of molecular nitrogen, the Lyman-Birge-Hopfield molecular band and the dissociation of molecular nitrogen through a continuum adjoining the Lyman-Birge-Hopfield band were added to the processes in RADICAL.

The absorption coefficients for photoionization of molecular nitrogen and the Lyman-Birge-Hopfield molecular band were determined using theoretical expressions derived according to Zel'dovich and Raizer[36]. For the photoionization process, the absorption coefficient was found to be given by the expression

$$k_\nu = 1.9986x10^{-14}\frac{N_{N_2}}{(h\nu)^3}\sum_{j=j^*}^{\infty}\frac{1}{j^3}e^{-(x_1-x_j)} \qquad (24)$$

$$x_j = \frac{(I_{N_2}-E_{elct_j})}{kT}$$

where the photon energy, $h\nu$, is given in electron volts. The lower limit on the summation over the electronic states in this equation is governed by the requirement that

Table 2: Radiative Processes Included in the Shock Layer and Precursor

	Radiative Process	Frequency Range (eV)
Shock Layer:		
	Free-Free, Bremsstrahlung	$0.0 \leq h\nu$
N	- Low Frequency Ionization (Highly excited states)	$0.0 \leq h\nu$
	- High Frequency Ionization (Ground and first two excited states)	$10.8 \leq h\nu$
	- Atomic Lines	--
N_2	- Birge-Hopfield Molecular Band	$6.50 \leq h\nu \leq 12.77$
	- 1st Positive Molecular Band	$0.75 \leq h\nu \leq 4.5$
	- 2nd Positive Molecular Band	$0.75 \leq h\nu \leq 4.5$
N_2^+	- 1st Negative Molecular Band	$2.23 \leq h\nu \leq 4.46$
Precursor:		
	Free-Free, Bremsstrahlung	$0.0 \leq h\nu$
N	- Low Frequency Ionization (Highly excited states)	$0.0 \leq h\nu$
	- High Frequency Ionization (Ground and first two excited states)	$10.8 \leq h\nu$
N_2	- Ionization Continuum (Ground and first three excited states)	$8.24 \leq h\nu$
	- Birge-Hopfield Molecular Band	$6.5 \leq h\nu \leq 12.77$
	- 1st Positive Molecular Band	$0.75 \leq h\nu \leq 4.5$
	- 2nd Positive Molecular Band	$0.75 \leq h\nu \leq 4.5$
	- Lyman-Birge-Hopfield Molecular Band	$4.77 \leq h\nu \leq 9.78$
	- Dissociation Continuum (Adjoining Lyman-Birge-Hopfield molecular band)	$9.78 \leq h\nu$
N_2^+	- 1st Negative Molecular Band	$2.23 \leq h\nu \leq 4.46$

the photon energy be greater than the binding energy for the state. Otherwise, the photon has insufficient energy to cause photoionization.

For this study, the summation in equation (24) was limited to the lowest four electronic states of the nitrogen molecule; however, in the cool precursor the populations of all except the ground electronic state were small. It should be noted that equation (24) provides values near the ionization threshold on the same order of magnitude as those predicted by Zel'dovich and Raizer[27] as well as those predicted by Marr[29].

The absorption coefficient for the Lyman-Birge-Hopfield molecular band was found to be given by

$$k_\nu = 9.1458x10^{16} \frac{N_{N_2}}{T} e^{-\frac{(113{,}314.97 - 11{,}610.14\ h\nu)}{T}} \qquad (25)$$

This equation was obtained from equation (5.113) of Zel'dovich and Raizer using an absorption oscillator strength of $3.7x10^{-6}$ from Allen[37] and then correcting to match experimental predictions given by Watanabe[28]. The absorption coefficient for the dissociation continuum adjoining this molecular band was assumed to be given by the expression

$$k_\nu = 4.97x10^{-20}\ N_{N_2} \qquad (26)$$

The constant in this equation was taken from the data presented by Watanabe for absorption through this process in cool air.

Through the course of this research, several numerical studies were performed to determine the importance of various absorption processes in the precursor. For instance, originally predissociation was allowed through both the 1st and 2nd positive

molecular bands of nitrogen as discussed above. However, it was found through the course of this study that there was no significant absorption of radiation through these bands. Therefore, the effects of these dissociation processes were removed to decrease the computational effort required.

Likewise, the Vegard-Kaplan band of molecular nitrogen was originally included in the precursor region for the frequency range from 2.45 eV to 5.84 eV. However, it was later found that there was insignificant absorption in this band; also, there was little evidence in the literature of the existence of this band in cool air. Similarly, although the Birge-Hopfield band was important in the high temperature shock layer, studies through the course of this work indicated that it was insignificant in the precursor; likewise, there was no reference in the literature to absorption through this band in cool air. It was also found that although photoionization was allowed for the ground as well as for the lower three electronic states of molecular nitrogen, ionization out of the ground state was much greater than that out of the excited states. Likewise, there was very little ionization out of the excited states of atomic nitrogen.

Consequently, the dominant processes found in the precursor region of this gas were absorption through the Lyman-Birge-Hopfield molecular band, the adjoining dissociation continuum and the ground state ionization continuum of molecular nitrogen. There was no significant emission of radiation in the precursor and the molecular bands and ionization continuum associated with the excited electronic states were negligible. These observations are consistent with the predictions for the absorption spectrum of cool air from previous literature[26,27,28,29]

SHOCK LAYER FORMULATION

In order to properly model the precursor ahead of a shock wave, it is necessary to know the spectral details of the radiation which passes from the shock layer through the shock front and into the precursor. However, to calculate these spectral details the conditions of the gas in the shock layer must be known in detail. For the flight conditions of interest in this study, a number of important phenomena such as chemical and thermal nonequilibrium must be included to properly model the shock layer; also, since the effects of radiation are of primary importance in the precursor, it is desirable that they be included in the shock layer. The inclusion of these three phenomena can significantly affect the shock layer conditions which would in turn affect the radiation and hence the precursor.

For this portion of the flow field, a viscous shock layer, VSL, scheme based on a highly modified version of the NASA code VSL3DNQ[22] was used. The VSL approach is basically a set of assumptions which when applied to the steady Navier-Stokes equations yield a more manageable set of equations which are valid in the region between the shock wave and the body. The benefit to using the viscous shock layer approach is that the VSL equations are solved by using a space marching technique starting at the stagnation streamline and moving aft around the body. This approach in general allows the equations to be solved faster than other techniques which require each cross flow plane, or the entire flow field, to be solved simultaneously. The VSL approach also alleviates the problems associated with solving the viscous and inviscid portions of the flow field separately and then matching the two solutions at the interface between them.

The viscous shock layer equations are commonly used to calculate the viscous flow conditions around blunt bodies and the case of interest in this study, an aerocapture vehicle entering the earth's atmosphere from an outer planet such as Mars, involves a blunt body entering at hypersonic speeds.

The VSL equations appropriate for the shock layer conditions in this study are as follows[22]:

Continuity

$$\frac{\partial}{\partial \xi_1}\left(\rho u_1 \sqrt{g}\right) + \frac{\partial}{\partial \xi_2}\left(\rho u_2 \sqrt{g}\right) + \frac{\partial}{\partial \xi_3}\left(\rho u_3 \sqrt{g}\right) = 0 \tag{27}$$

ξ_1-Momentum

$$\begin{aligned} &\rho u_1 \frac{\partial u_1}{\partial \xi_1} + \rho u_2 \frac{\partial u_1}{\partial \xi_2} + \rho u_3 \frac{\partial u_1}{\partial \xi_3} + \rho\left[u_1^2\begin{Bmatrix}1\\11\end{Bmatrix} + 2u_1u_2\begin{Bmatrix}1\\12\end{Bmatrix} + 2u_1u_3\begin{Bmatrix}1\\13\end{Bmatrix}\right. \\ &\left. + u_2^2\begin{Bmatrix}1\\22\end{Bmatrix} + 2u_2u_3\begin{Bmatrix}1\\23\end{Bmatrix} + u_3^2\begin{Bmatrix}1\\33\end{Bmatrix}\right] + \frac{1}{g}\left[g_{33}\frac{\partial p}{\partial \xi_1} - g_{13}\frac{\partial p}{\partial \xi_3}\right] \\ &= \epsilon^2\left[\frac{\partial \mu}{\partial \xi_2}\frac{\partial u_1}{\partial \xi_2} + \mu\frac{\partial^2 u_1}{\partial \xi_2^2}\right] + \mu\epsilon^2\left[3\frac{\partial u_1}{\partial \xi_2}\begin{Bmatrix}1\\21\end{Bmatrix} + \frac{\partial u_1}{\partial \xi_2}\begin{Bmatrix}3\\23\end{Bmatrix} + 2\frac{\partial u_3}{\partial \xi_2}\begin{Bmatrix}1\\23\end{Bmatrix}\right] \end{aligned} \tag{28}$$

ξ_2-Momentum

$$\begin{aligned} &\rho u_1 \frac{\partial u_2}{\partial \xi_1} + \rho u_2 \frac{\partial u_2}{\partial \xi_2} + \rho u_3 \frac{\partial u_2}{\partial \xi_3} + \rho\left[u_1^2\begin{Bmatrix}2\\11\end{Bmatrix} + 2u_1u_2\begin{Bmatrix}2\\12\end{Bmatrix} + 2u_1u_3\begin{Bmatrix}2\\13\end{Bmatrix}\right. \\ &\left. + u_2^2\begin{Bmatrix}2\\22\end{Bmatrix} + 2u_2u_3\begin{Bmatrix}2\\23\end{Bmatrix} + u_3^2\begin{Bmatrix}2\\33\end{Bmatrix}\right] + \frac{\partial p}{\partial \xi_2} = 0 \end{aligned} \tag{29}$$

ξ_3-Momentum

$$\rho u_1\frac{\partial u_3}{\partial \xi_1} + \rho u_2\frac{\partial u_3}{\partial \xi_2} + \rho u_3\frac{\partial u_3}{\partial \xi_3} + \rho\left[u_1^2\begin{Bmatrix}2\\11\end{Bmatrix} + 2u_1u_2\begin{Bmatrix}2\\12\end{Bmatrix} + 2u_1u_3\begin{Bmatrix}2\\13\end{Bmatrix}\right.$$

$$\left. + u_2^2\begin{Bmatrix}3\\22\end{Bmatrix} + 2u_2u_3\begin{Bmatrix}3\\23\end{Bmatrix} + u_3^2\begin{Bmatrix}3\\33\end{Bmatrix}\right] + \frac{1}{g}\left[g_{11}\frac{\partial p}{\partial \xi_3} - g_{13}\frac{\partial p}{\partial \xi_1}\right] \qquad (30)$$

$$= \epsilon^2\left[\frac{\partial \mu}{\partial \xi_2}\frac{\partial u_3}{\partial \xi_2} + \mu\frac{\partial^2 u_3}{\partial \xi_2^2}\right] + \mu\epsilon^2\left[\frac{\partial u_3}{\partial \xi_2}\begin{Bmatrix}1\\21\end{Bmatrix} + 2\frac{\partial u_1}{\partial \xi_2}\begin{Bmatrix}3\\12\end{Bmatrix} + 3\frac{\partial u_3}{\partial \xi_2}\begin{Bmatrix}3\\23\end{Bmatrix}\right]$$

Energy

$$\rho u_1 C_p\frac{\partial T}{\partial \xi_1} + \rho u_2 C_p\frac{\partial T}{\partial \xi_2} + \rho u_3 C_p\frac{\partial T}{\partial \xi_3} - \left[u_1\frac{\partial p}{\partial \xi_1} + u_2\frac{\partial p}{\partial \xi_2} + u_3\frac{\partial p}{\partial \xi_3}\right]$$

$$= \epsilon^2\frac{\partial}{\partial \xi_2}\left(K\frac{\partial T}{\partial \xi_2}\right) + \epsilon^2\frac{k}{\sqrt{g}}\frac{\partial \sqrt{g}}{\partial \xi_2}\frac{\partial T}{\partial \xi_2} + \epsilon^2\sum_{i=1}^{N_s} C_{p_i}\frac{\mu L_e}{Pr}\frac{\partial C_i}{\partial \xi_2}\frac{\partial T}{\partial \xi_2} - \sum_{i=1}^{N_s} h_i\dot{w}_i \qquad (31)$$

$$+ \epsilon^2\mu\left[g_{11}\left(\frac{\partial u_1}{\partial \xi_2}\right)^2 + 2g_{13}\frac{\partial u_1}{\partial \xi_2}\frac{\partial u_3}{\partial \xi_2} + g_{33}\left(\frac{\partial u_3}{\partial \xi_2}\right)^2\right]$$

Species Continuity

$$\rho u_1\frac{\partial C_i}{\partial \xi_1} + \rho u_2\frac{\partial C_i}{\partial \xi_2} + \rho u_3\frac{\partial C_i}{\partial \xi_3} = \frac{\epsilon^2}{\sqrt{g}}\frac{\partial}{\partial \xi_2}\left(\sqrt{g}\frac{\mu L_e}{P_r}\frac{\partial C_i}{\partial \xi_2}\right) + \dot{w}_i \qquad (32)$$

These equations are cast in a nonorthogonal, body-oriented coordinate system, Figure 6. The above equations were derived by nondimensionalizing the steady Navier-Stokes equations for a reacting gas and performing an order of magnitude analysis. In this

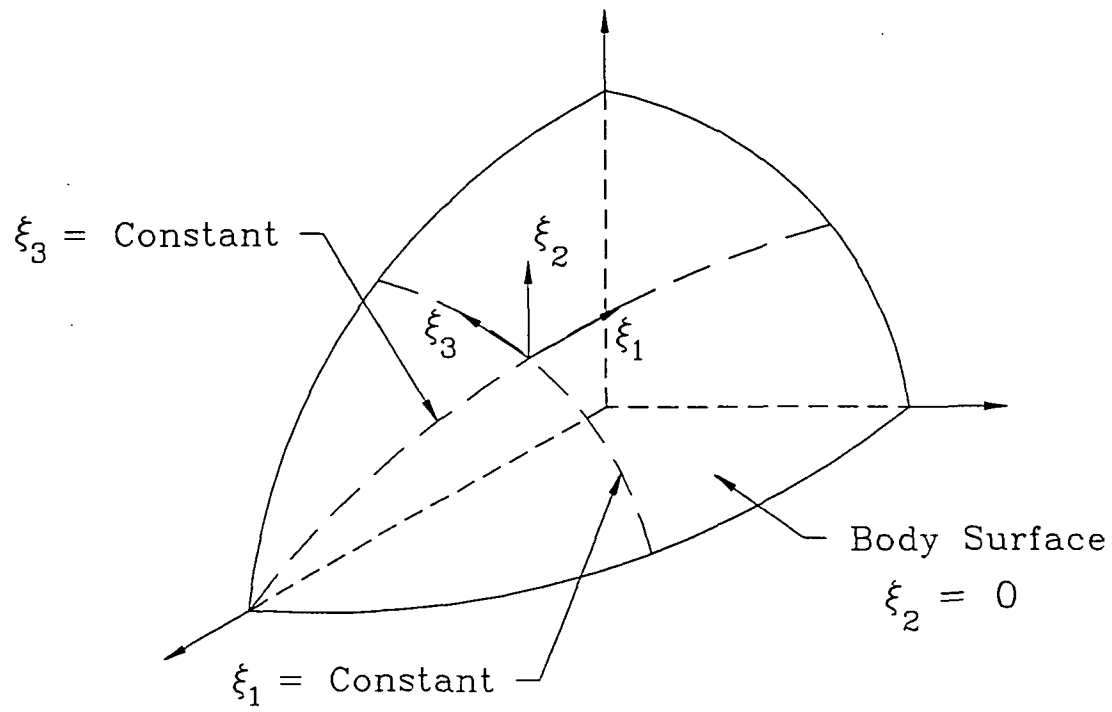

Figure 6: Coordinate System for the Viscous Shock Layer Program

analysis, the normal velocity, u_2, and coordinate, ξ_2, were assumed to be of the order ϵ where

$$\epsilon = \sqrt{\frac{\mu_{ref}}{\rho_\infty U_\infty R_N}} \tag{33}$$

and only terms in the Navier-Stokes equations of order ϵ or less were retained while the higher order terms were neglected.

The effects of thermal nonequilibrium in the shock layer were also included using a quasi-equilibrium electron energy equation[38],

$$T_e = T - \frac{1.23357x10^{-10}}{T_e^{0.5} SX[e^-] m_e} \left[\dot{w}_{e,eN} E_{I_N} + \dot{w}_e \frac{5}{2} k T_e \right] \tag{34}$$

where

$$SX = N_N S_{eN} + N_{N^+} S_{eN^+} + N_{N_2} S_{eN_2} \tag{35}$$

This equation was derived from the full free electron energy equation by Carlson and Gally[38] by neglecting the derivative terms as well as the diffusion terms. The collisional reaction terms in this equation and in the species continuity equations were calculated using the collisional cross sections of Gnoffo, Gupta and Shinn[31]; also, for the shock layer flow field calculations a lewis number, L_e, of of one was used.

The VSL program used in this study was modified extensively by Carlson and Gally[23]. These modifications primarily involved the nonequilibrium chemistry and the

effects of thermal nonequilibrium. However, they also modified the code to allow the shock layer and radiation calculations to be coupled to the gas dynamics, thus incorporating the effects of the absorption and emission of radiation into the flow field solution.

GLOBAL SOLUTION SCHEME

The computational methods used in the calculation of flow field conditions in the precursor, the flow field conditions in the shock layer and the radiative transfer were described in previous sections of this text. The means by which these three individual methods and programs were coupled together to calculate the entire flow field, shock layer and precursor, as well as the radiative transfer will now be discussed. The process of calculating the coupled flow field and radiative transfer was accomplished through a global iteration scheme involving all three of the programs discussed previously. This global iteration scheme is illustrated graphically in Figure 7.

The solution process was initiated by first neglecting the effects of the absorption of radiation in the precursor. For these conditions, the VSL program was used to calculate the flow field conditions in the shock layer including nonequilibrium chemistry and radiative/gas dynamic coupling. This shock layer solution was then utilized to determine the radiative transfer in the precursor portion of the flow field.

The radiative transfer in the shock layer and the precursor was first calculated with RADICAL using the shock layer solution and assuming that the flow field conditions in the precursor were constant at the freestream values. The absorption coefficients and radiative flux values from these radiation calculations were then used to compute the flow field conditions in the precursor region and this new precursor solution was compared to the previous flow field conditions. If the change between the two precursor solutions was greater than a preselected convergence criteria, the radiative transfer was calculated using the updated precursor flow field. This iteration scheme was

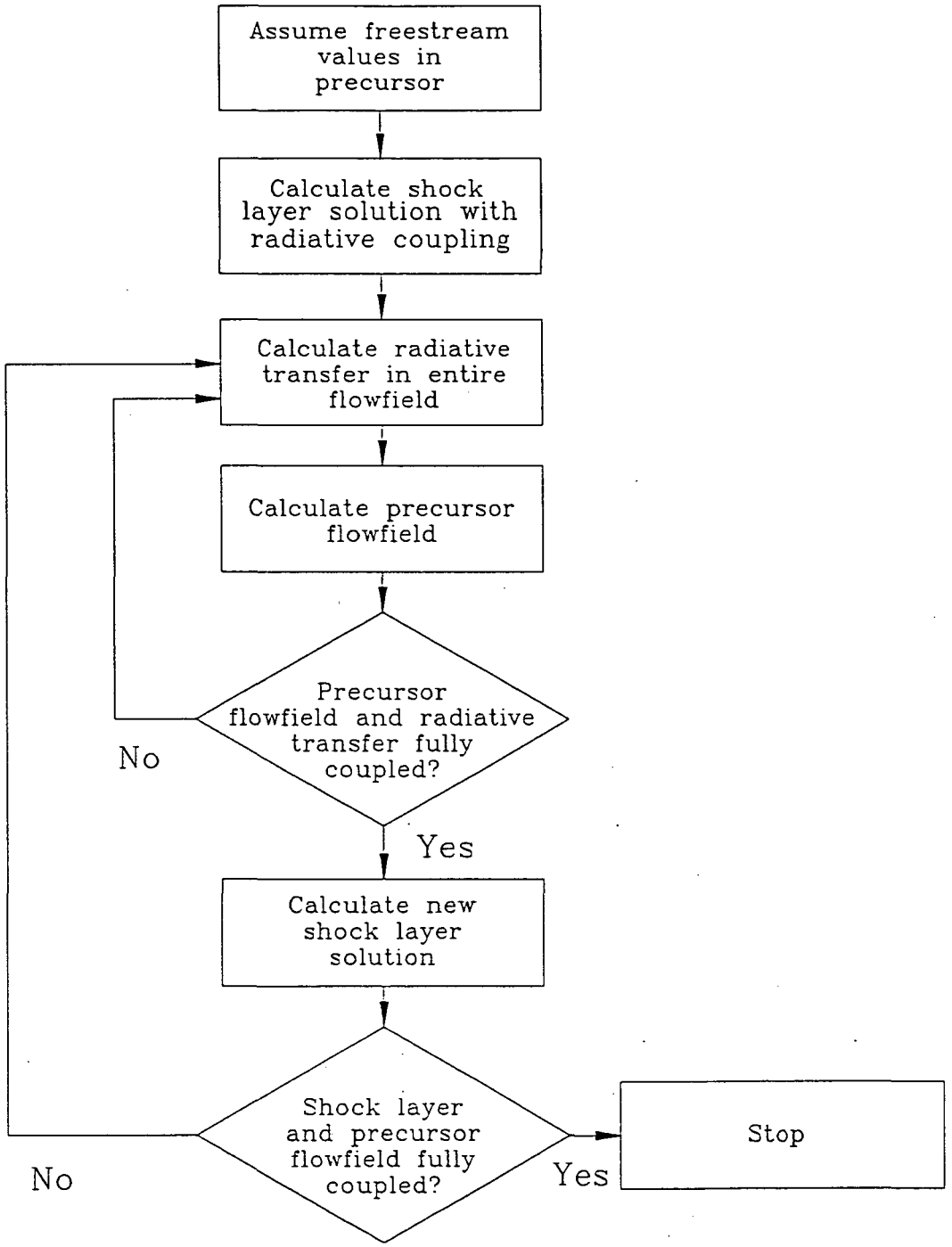

Figure 7: Block Diagram of the Global Iteration Scheme

repeated until the radiative transfer and the precursor flow field were fully coupled and converged.

After calculating the coupled precursor flow field and radiative transfer, a new shock layer solution was calculated including the effects of the precursor ahead of the shock. These calculations were performed with the VSL program utilizing the precursor results directly in front of the shock as freestream conditions. This new shock layer solution was then compared to the original solution to determine the effects of the precursor on the shock layer. If this comparison showed significant changes in the shock layer flow field and the radiative transfer through the shock layer from the initial results, then the precursor flow field was calculated again using the new shock layer solution. This process, which was repeated until convergence, allowed a solution to be calculated for the entire flow field which fully coupled the precursor and the shock layer.

RESULTS

This section outlines the results obtained for a total of six test cases at three altitudes, 72 Km, 75 Km and 80 Km. The atmospheric conditions for these three altitudes are given in Table 3. These cases are representative of "typical" conditions for an aerobrake vehicle entering the earth's atmosphere upon returning from Mars. The freestream conditions for these six cases are given in Table 4.

All of the results discussed in this section were obtained for the stagnation streamline of a 2.3 meter nose radius vehicle. The shock layer calculations were made using 52 points between the shock wave and the body and allowing for atomic local thermodynamic nonequilibrium as well as radiation/gasdynamic coupling. The radiation calculations were made using 74 continuum frequency points selected to provide good spectral detail in the ultraviolet absorption region of interest in the precursor. A wall temperature of ~~2970~~ 1650 °K was used in both the shock layer and the radiation calculations. The precursor flow field was calculated using a convergence requirement of 0.05 percent and the changes allowed between each point in the precursor were confined to the range from 1 to 10 percent.

The discussion of these results is divided into two sections. The first is a detailed discussion of case 1, 72 Km altitude and a freestream velocity of 16 Km/sec, which was the most extreme case for the precursor. The second section is a discussion of two parametric studies, the first over a range of altitudes and the second over a range of velocities. In that section, the variation of the precursor flow field properties with variations in the freestream velocity and altitude are discussed.

Table 3: Atmospheric Conditions for Three Altitudes; 72 Km, 75 Km and 80Km

Altitude (Km)	Temperature, T_∞ (°K)	Pressure, p_∞ (dyn/cm^2)	Density, ρ_∞ (g/cm^3)
72	211.87	41.87	6.659×10^{-8}
75	200.15	25.75	4.335×10^{-8}
80	180.65	10.72	1.999×10^{-8}

Table 4: Freestream Conditions, Shock Standoff Distances and Radiative Fluxes

Case	Velocity, V_∞ (Km/sec)	Altitude (Km)	Shock Standoff Distance, X_{shock} (cm)	Radiative Flux Through Shock, (W/cm^2)
1	16	72	6.60	1,385.0
2	16	75	6.72	776.2
3	16	80	7.25	264.5
4	14	80	8.69	126.9
5	12	80	10.70	65.9
6	10	80	11.14	54.2

Detailed Discussion of Case 1 (Alt = 72 Km, V_∞ = 16 Km/sec)

Figures 8 to 14 show the heavy particle temperature, electron/electronic temperature, total enthalpy, electron/electronic energy, pressure, density and velocity variations through the precursor for case 1. Likewise, Figures 15 to 19 show the variations in the five species mass fractions through the precursor; also, the radiative flux through the shock front and the shock standoff distance for this case are given in Table 4. The radiation emitted from the shock layer for case 1 was the greatest of all the cases considered. Thus, this case experienced the largest flow field perturbations in the precursor region.

Figure 8 shows that the heavy particle temperature increased steadily through the precursor region as the shock front was approached from upstream. However, for this case the change in the heavy particle temperature was still less than one percent. On the other hand, there was a large increase in the electron/electronic temperature throughout the precursor region as shown in Figure 9. The large values for the electron/electronic temperature far from the shock were a result of photoionization in this region caused by photons at frequencies much greater than the ionization threshold; the large amount of excess energy in this photoionization process resulted in the creation of electrons with a very high kinetic energy. However, as can be seen in Figure 19, although the electron/electronic temperature was high far from the shock the electron mass fraction in this region was extremely small.

The electron/electronic temperature increased steadily ahead of the shock to a maximum value of approximately 6,300 °K at a distance of 40 shock standoff distances

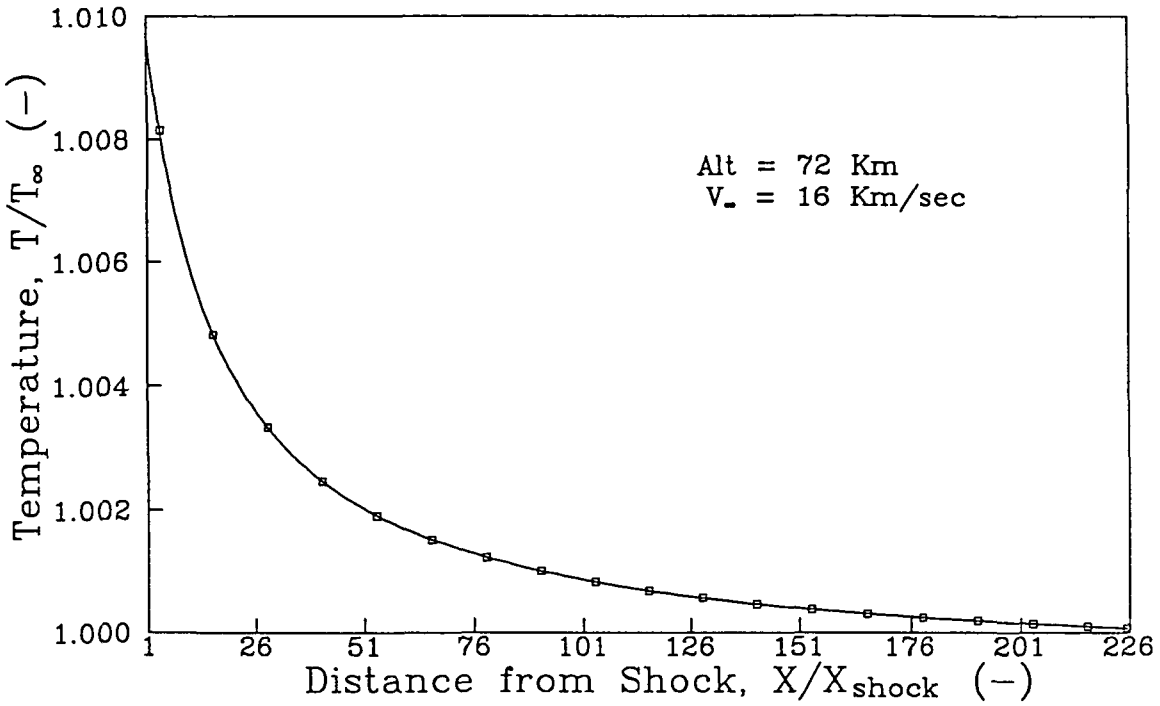

Figure 8: Heavy Particle Temperature in the Precursor Region;
(Alt = 72 Km, V_∞ = 16 Km/sec)

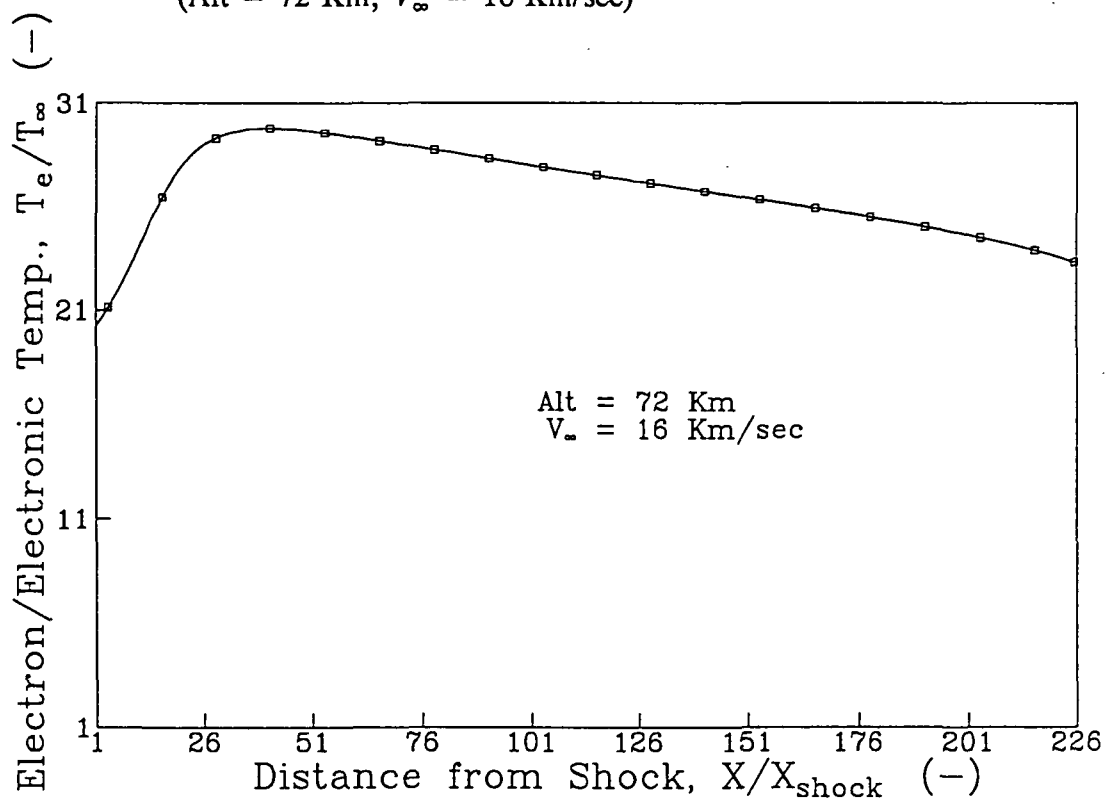

Figure 9: Electron/Electronic Temperature in the Precursor Region;
(Alt = 72 Km, V_∞ = 16 Km/sec)

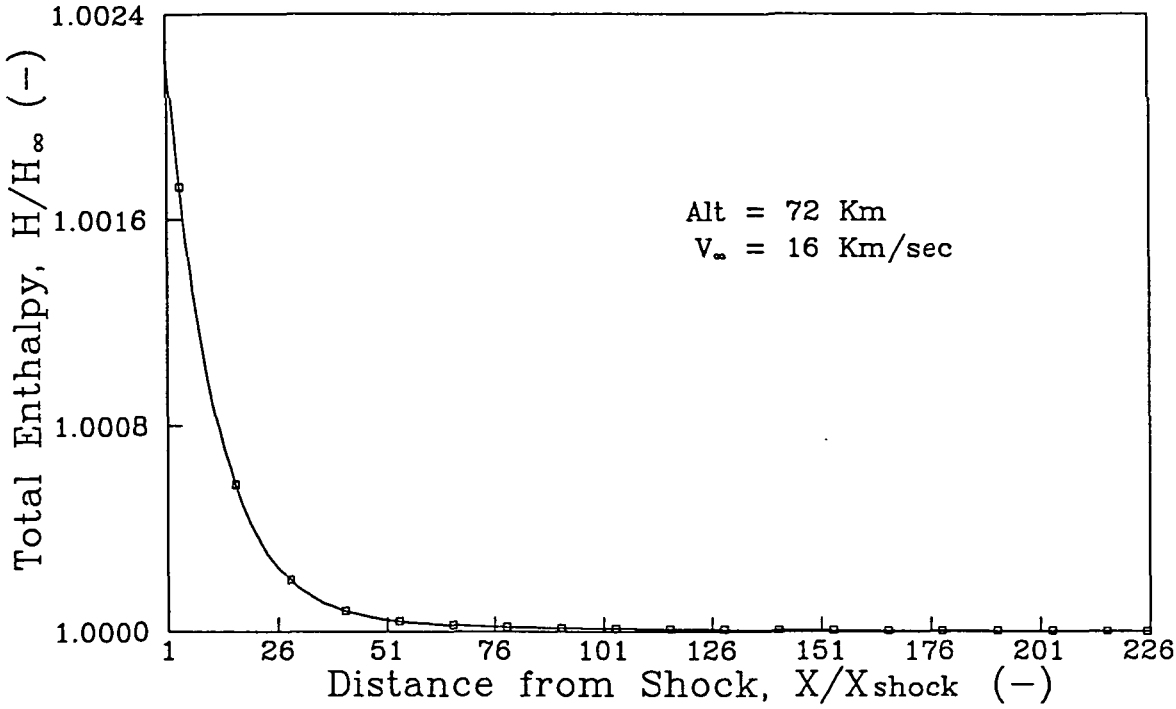

Figure 10: Total Enthalpy in the Precursor Region;
(Alt = 72 Km, V_∞ = 16 Km/sec)

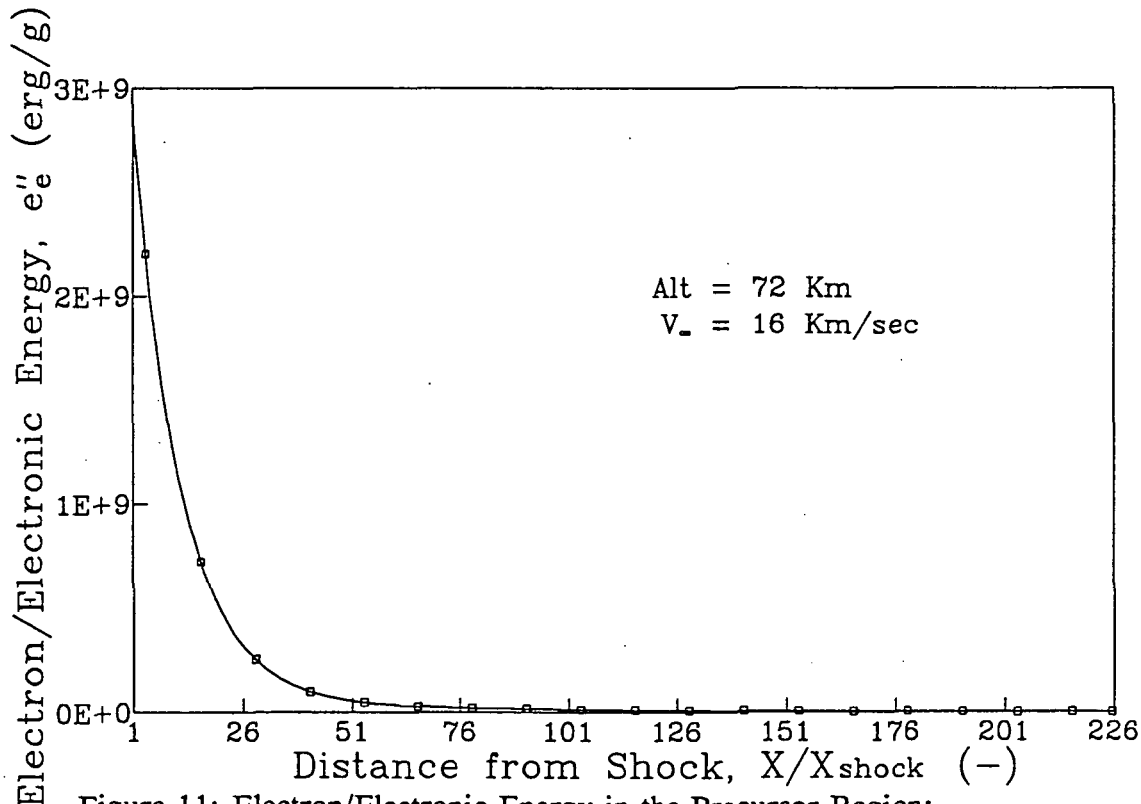

Figure 11: Electron/Electronic Energy in the Precursor Region;
(Alt = 72 Km, V_∞ = 16 Km/sec)

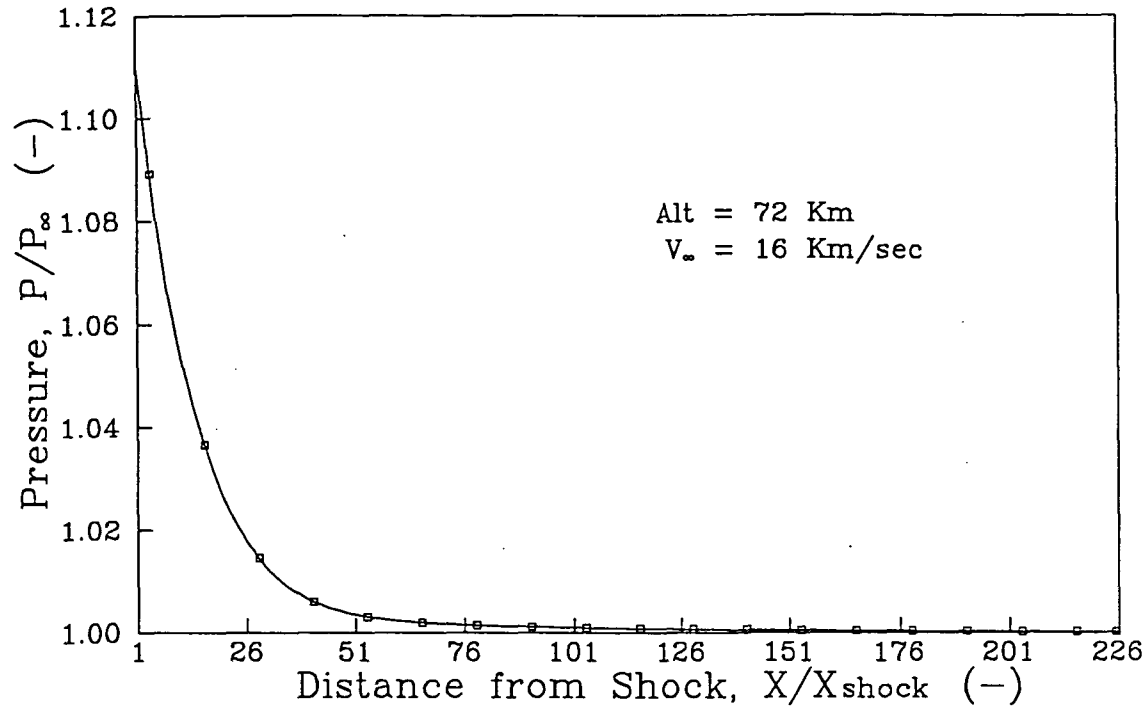

Figure 12: Pressure in the Precursor Region;
(Alt = 72 Km, V_∞ = 16 Km/sec)

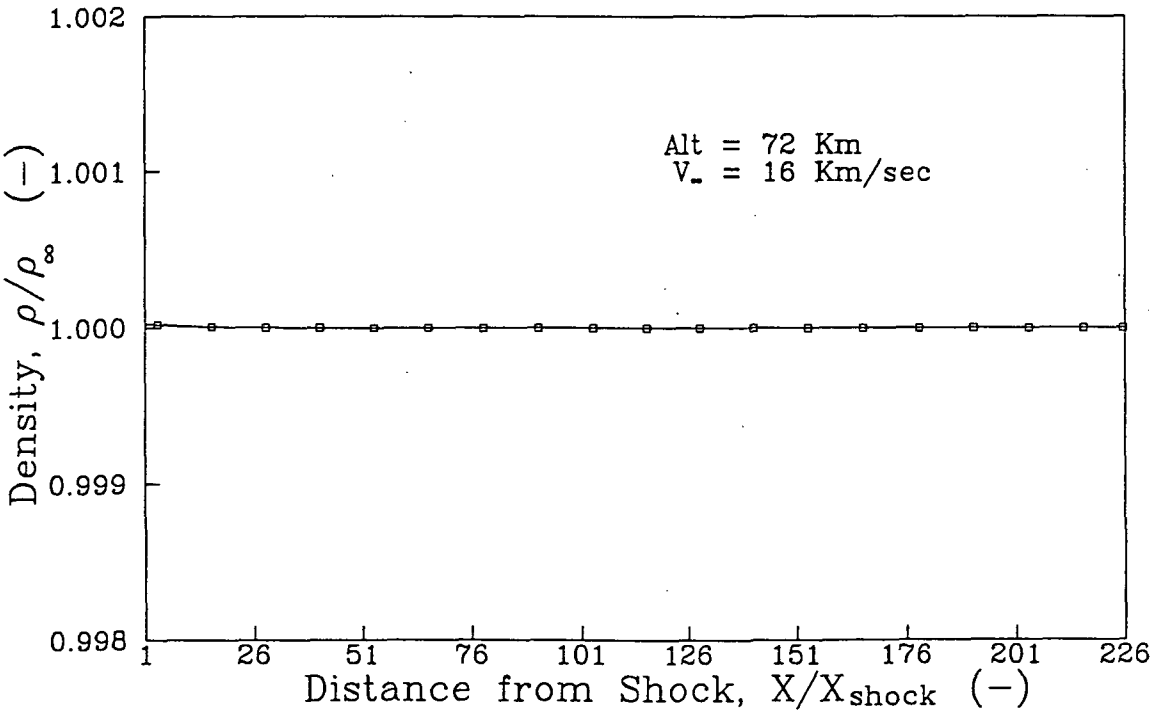

Figure 13: Density in the Precursor Region;
(Alt = 72 Km, V_∞ = 16 Km/sec)

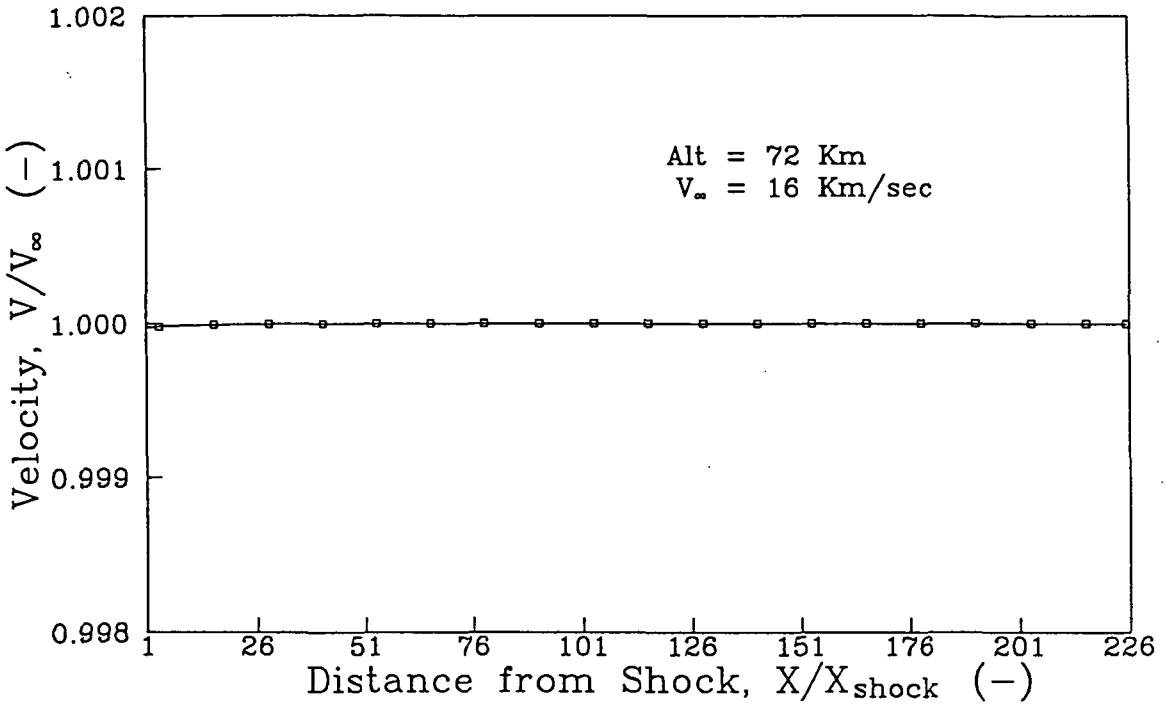

Figure 14: Velocity in the Precursor Region;
(Alt = 72 Km, V_∞ = 16 Km/sec)

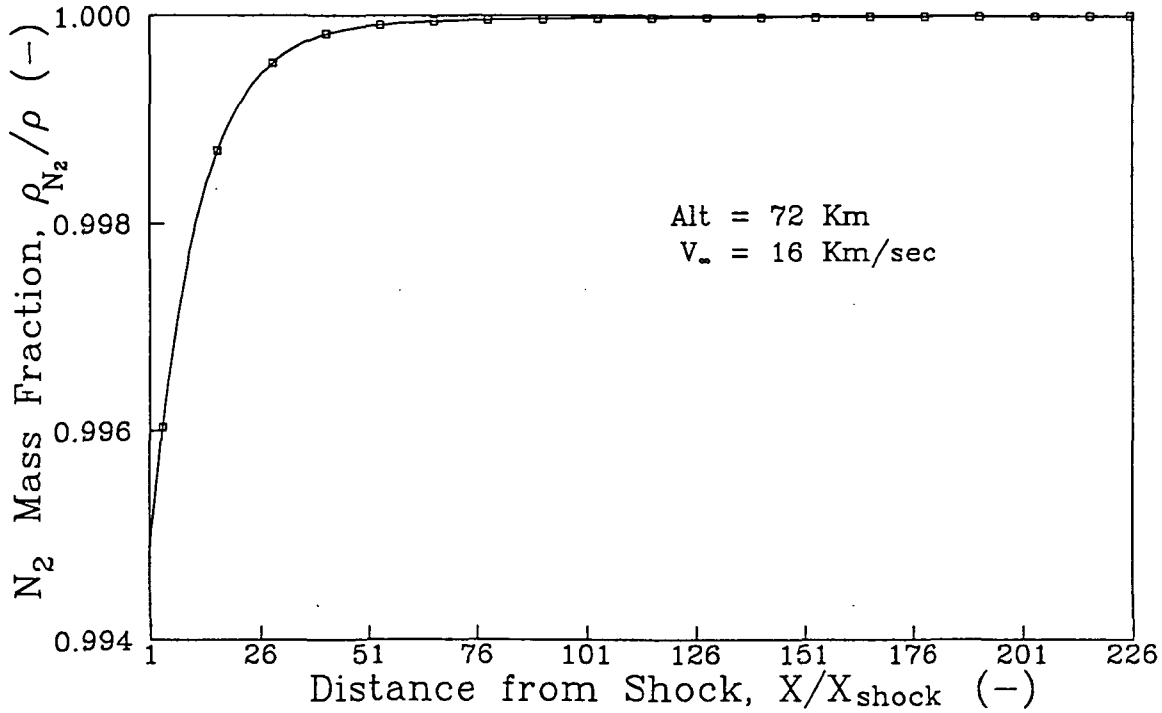

Figure 15: N_2 Mass Fraction in the Precursor Region;
(Alt = 72 Km, V_∞ = 16 Km/sec)

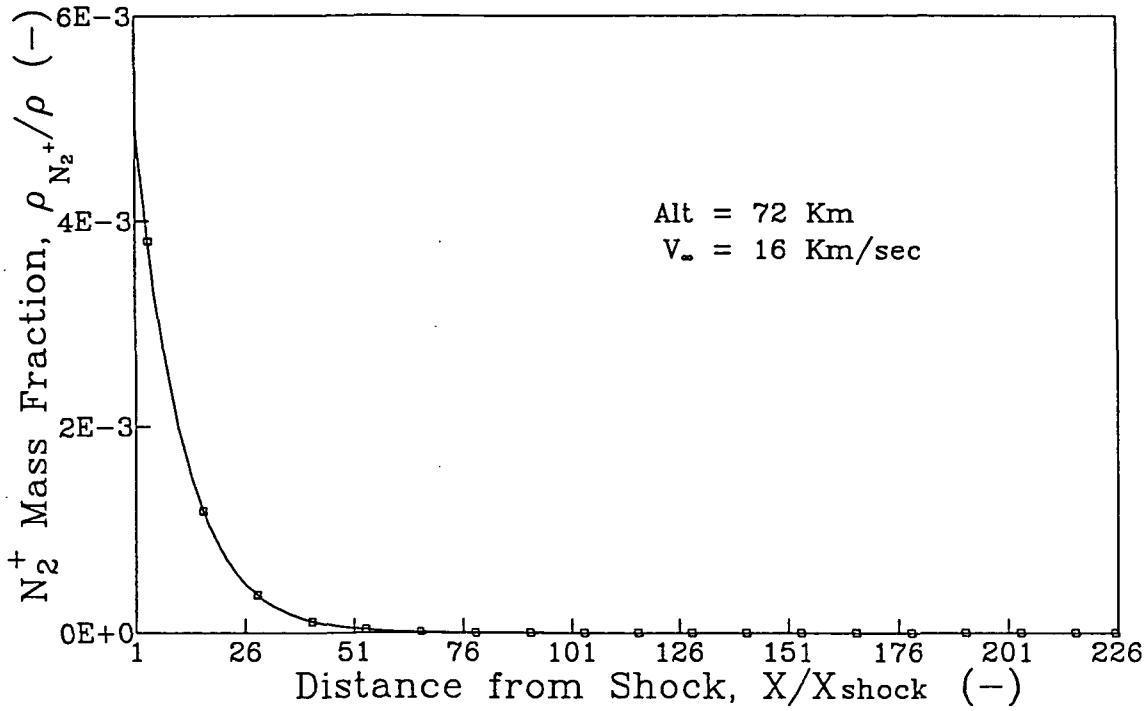

Figure 16: N_2^+ Mass Fraction in the Precursor Region;
(Alt = 72 Km, V_∞ = 16 Km/sec)

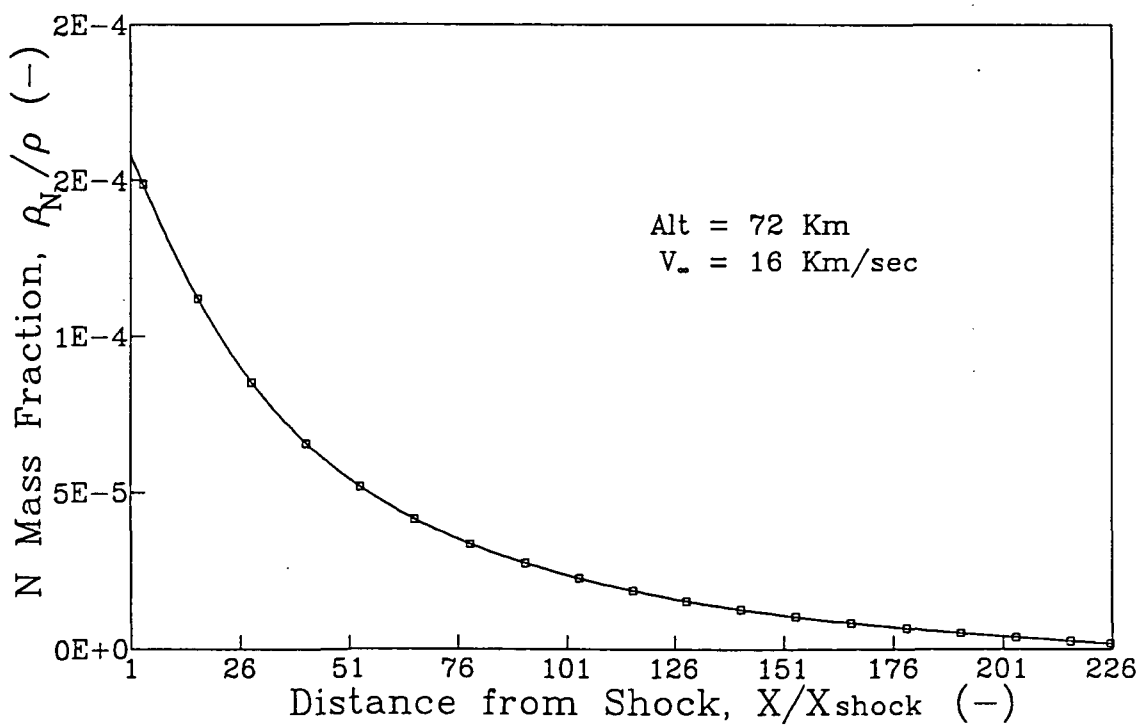

Figure 17: N Mass Fraction in the Precursor Region;
(Alt = 72 Km, V_∞ = 16 Km/sec)

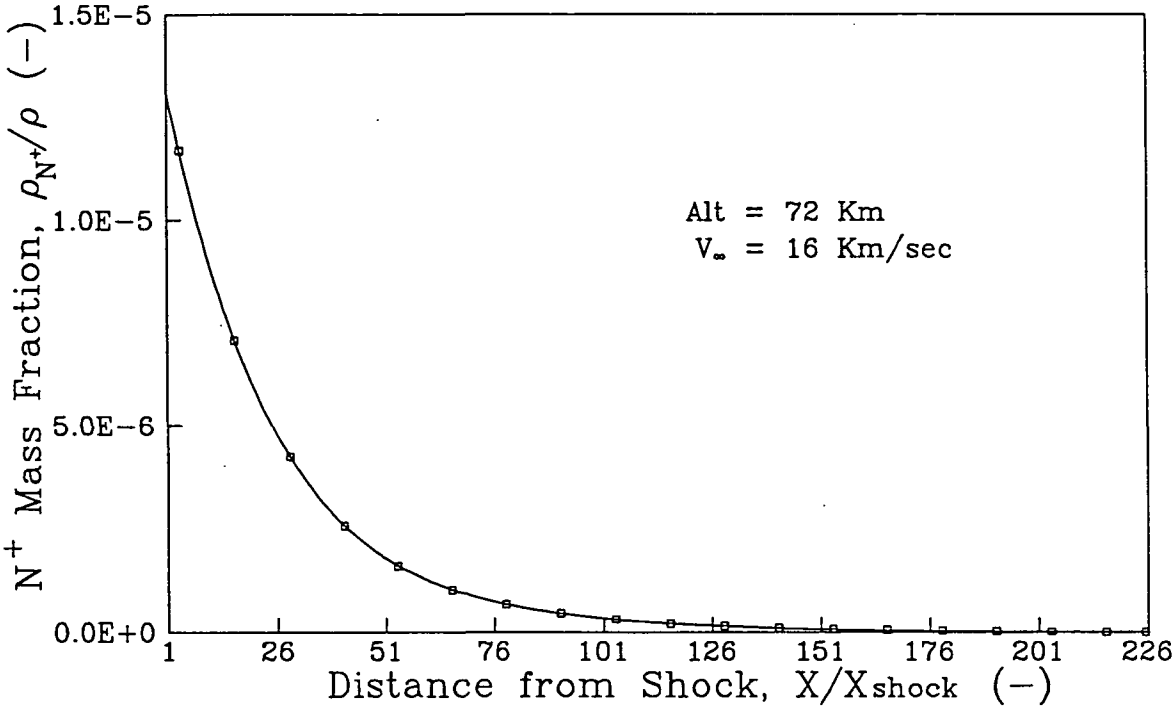

Figure 18: N^+ Mass Fraction in the Precursor Region;
(Alt = 72 Km, V_∞ = 16 Km/sec)

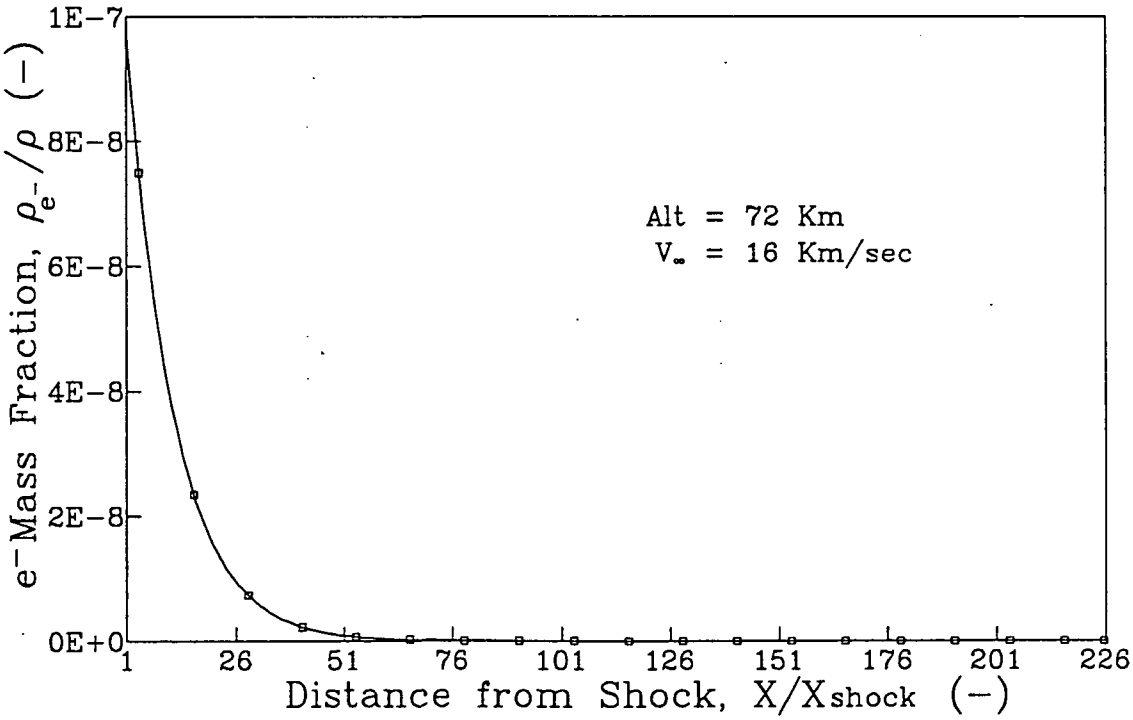

Figure 19: e^- Mass Fraction in the Precursor Region;
(Alt = 72 Km, V_∞ = 16 Km/sec)

ahead of the body. It then decreased rapidly to a value of 4,290 °K immediately ahead of the shock front. This decrease in the electron/electronic temperature was a result of the production of "low" energy electrons through photoionization caused by photons of frequencies only slightly larger than the ionization threshold. The production of these "low" energy electrons caused a decrease in the average energy per electron, hence a decrease in the electron/electronic temperature. That this decrease in the electron/electronic temperature was a result of the production of "low" energy electrons rather than due to a transfer of energy from the electrons through elastic collisions can be seen in Figure 11. If energy transfer through the elastic collisions were responsible, there would have been a decrease in the electron/electronic energy corresponding to the decrease in the electron/electronic temperature. The region of decrease in the electron/electronic temperature also coincided with the region of rapid increase in the number of electrons on the gas, Figure 19.

The photons with energies near the ionization energy were absorbed rapidly in front of the shock since the strongest absorption region for a photoionization process is at frequencies near the ionization threshold. The higher energy photons in the weaker absorption range, far from the threshold, escaped to distances further from the shock where they were absorbed causing the creation of high energy electrons as discussed above. It should be noted that a similar decrease in the precursor electron temperature was also predicted by Foley and Clarke[19] for argon.

Like the heavy particle temperature, the total enthalpy of the gas increased continuously towards the shock. The increase in the total enthalpy of the gas in the

precursor was less than 0.25 percent; thus, for this case the increase in the enthalpy of the gas due to the absorption of radiation was negligible. However, as can be seen in Figure 11, the change in the electron/electronic energy was not negligible. This energy increased from a value of essentially zero in the freestream to a value on the order of 10^9 immediately ahead of the shock front. It should be noted at this point that 99 percent of the radiative energy absorbed in the precursor affected the electron/electronic energy of the gas and only 1 percent of the energy affected the heavy particle translational, vibrational and rotational energies of the gas. Likewise, of the increase in the electron/electronic energy, 96 percent was involved with an increase in the zero point energy of the gas. Therefore, the majority of the energy absorbed in the precursor was involved with the ionization and dissociation of the gas.

The pressure in the precursor, which was displayed in Figure 12, showed the same continuous increase towards the shock as did in the heavy particle temperature. However, due to the elevated kinetic energy of the electrons, the pressure increased by 11 percent. Figures 13 and 14 show that in the precursor region, the density and velocity of the gas were essentially constant. This behavior verifies what was shown by Tiwari and Szema[20,34] and assumed by many other researchers.[13,14,16,33]

Considering the mass fractions of the five species it can be seen in Figures 15 to 19 that the dominant chemical reaction in the precursor was the photoionization of molecular nitrogen. The mass fractions of the ionized nitrogen molecule was at least an order of magnitude greater than those for the nitrogen atom and the ionized nitrogen

atom; although, there were significant quantities of all three species immediately ahead of the shock.

Due to the fact that the dominant change in the precursor region was caused by the photoionization of molecular nitrogen, the thickness of the precursor was considered to be the distance through which this reaction had an effect. By this definition, Figures 16 and 19 show that for this case the shock precursor thickness was in the range of 75 shock standoff distances, or 495 cm. Although there was a slight heating of the gas as well as the production of nitrogen atoms through photodissociation at greater distances from the shock, their effects were small compared to the changes within 495 cm of the shock.

Figure 20 shows the frequency variation of the radiative flux at the shock front and in the precursor 495 cm ahead of the shock. The radiative flux at the latter point in the precursor is shown both corrected using the shock layer attenuation factor and uncorrected. Comparing the uncorrected flux at 495 cm in the precursor to the flux through the shock front shows the changes through this region due to the absorption of radiation; it can be seen that the dominant absorption in the precursor was at frequencies greater than the ionization threshold for molecular nitrogen, 15.59 eV. Although there was absorption at frequencies less than this threshold due to photodissociation of molecular nitrogen and photoionization of atomic nitrogen, the amount of energy absorbed in these processes was small compared to that absorbed in the photoionization of molecular nitrogen. This result agrees with the previous statement in discussion of the mass fractions that the dominant reaction was molecular ionization.

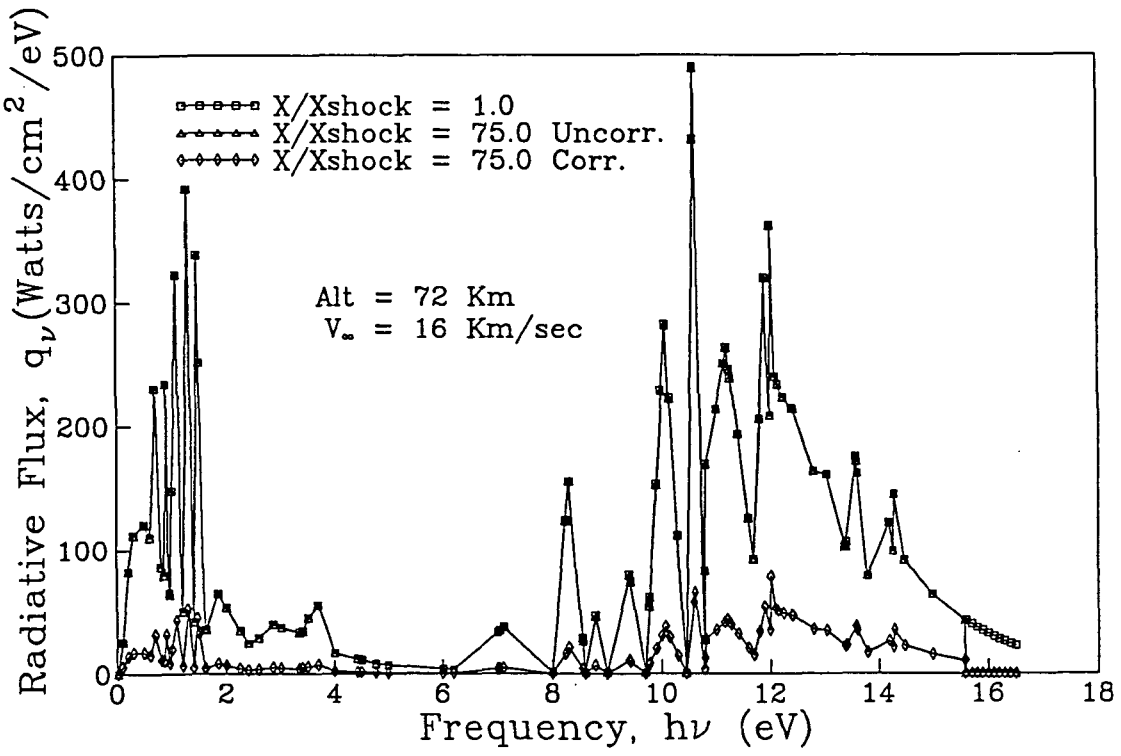

Figure 20: Radiative Flux Through the Shock Front;
(Alt = 72 Km, V_∞ = 16 Km/sec)

Comparing the radiative flux at 495 cm in the precursor that was corrected for geometric attenuation to that through the shock front shows that although only a small portion of the radiation was absorbed, very little radiation reached this point in the precursor. As can be seen from the figure, the geometric attenuation of the radiation dominated over absorption by the precursor gas.

The radiation propagating through the shock wave from the shock layer into the precursor was distributed over a wide range of frequencies, Figure 20. As can be seen from this figure, a large portion of the radiative energy was in the infrared frequency range ($h\nu \leq 5$ eV). Most of the radiation in this region was emitted by the entry body itself; although, embedded within the continuum radiation from the body were a number of atomic lines. Also, the peak of radiation near 3.5 eV was due to three molecular bands, the 1st negative band of N_2^+ and the 1st and 2nd positive bands of N_2. There was also a large quantity of radiative energy in the ultraviolet frequency range. The radiation in the frequency range from 8 to 10 eV was due to the atomic lines of nitrogen. That above 10 eV was due primarily to the Birge-Hopfield band of molecular nitrogen as well as the ionization continuum and lines of atomic nitrogen. Through the visible frequency ranges ($5 \text{ eV} \leq h\nu \leq 8$ eV) there was very little radiative energy.

Figures 21 to 29 show the heavy particle temperature, electron temperature, pressure, density and mass fractions in the shock layer for case 1 both neglecting and including the effects of the precursor region ahead of the shock front. As can be seen in these figures, the inclusion of the changes in the gas ahead of the shock layer had

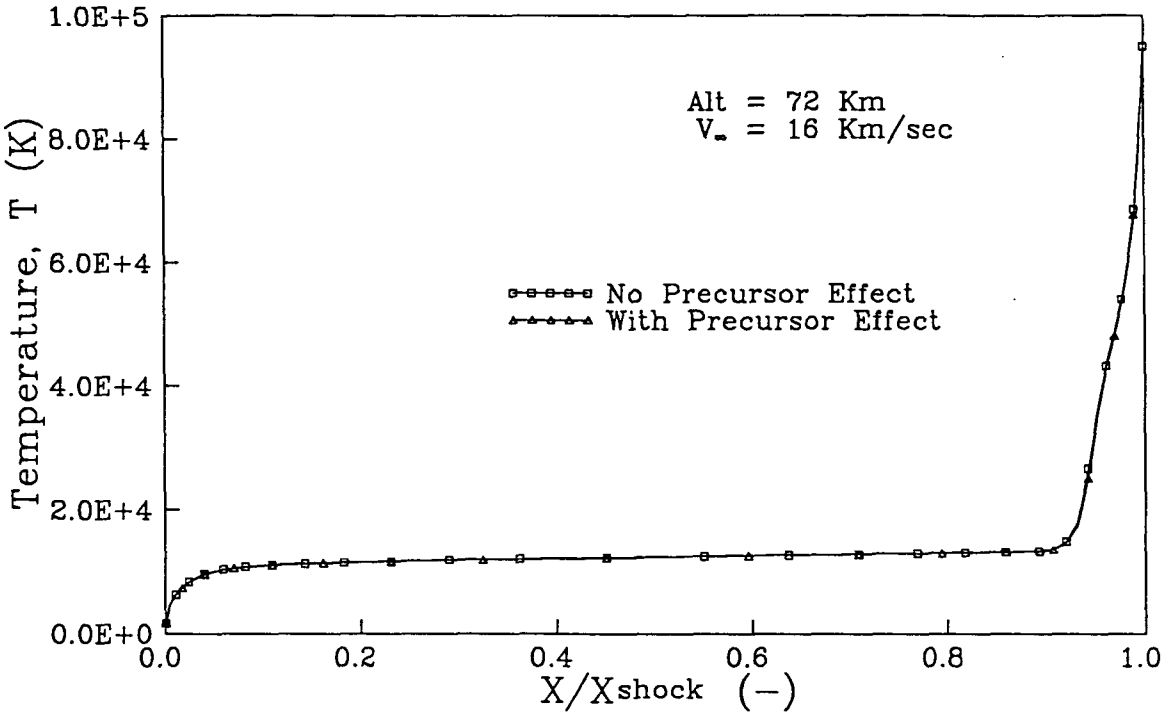

Figure 21: Heavy Particle Temperature in the Shock Layer;
(Alt = 72 Km, V_∞ = 16 Km/sec)

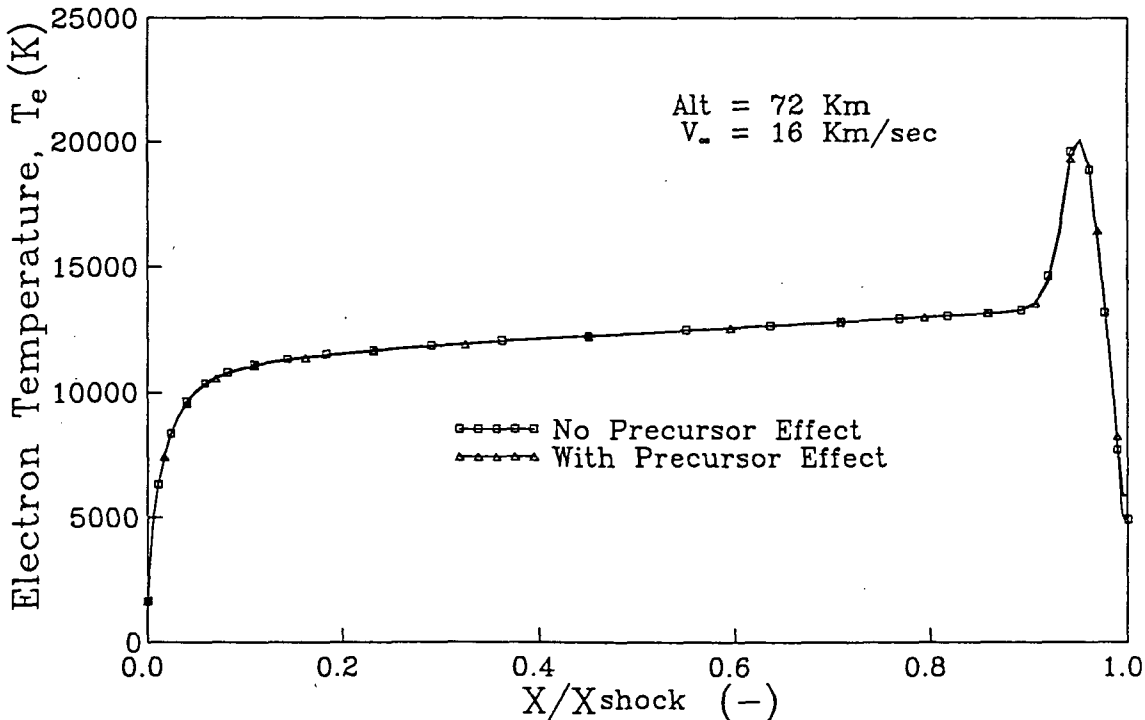

Figure 22: Electron Temperature in the Shock Layer;
(Alt = 72 Km, V_∞ = 16 Km/sec)

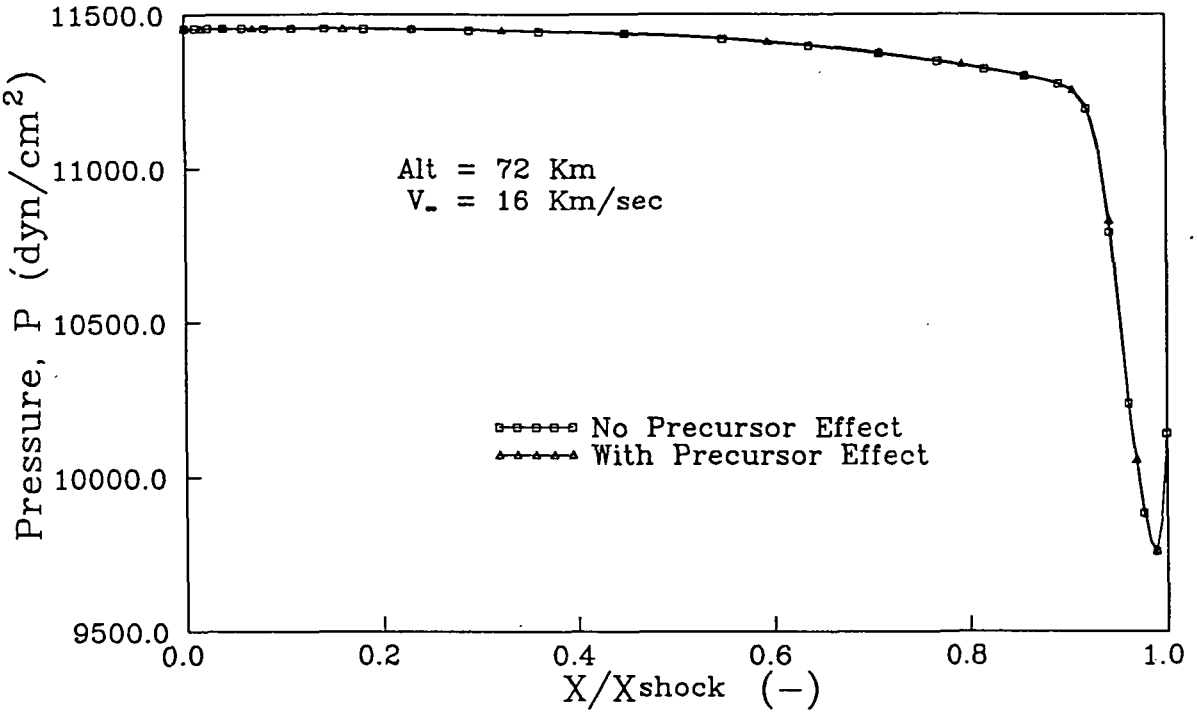

Figure 23: Pressure in the Shock Layer;
(Alt = 72 Km, V_∞ = 16 Km/sec)

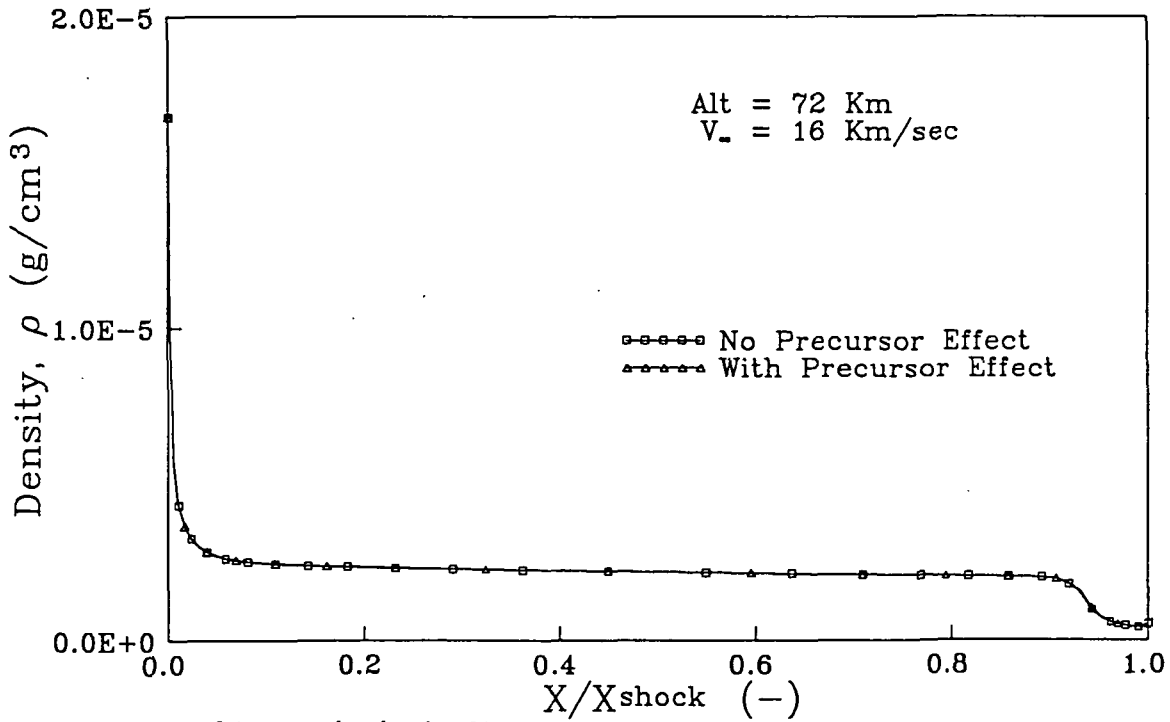

Figure 24: Density in the Shock Layer;
(Alt = 72 Km, V_∞ = 16 Km/sec)

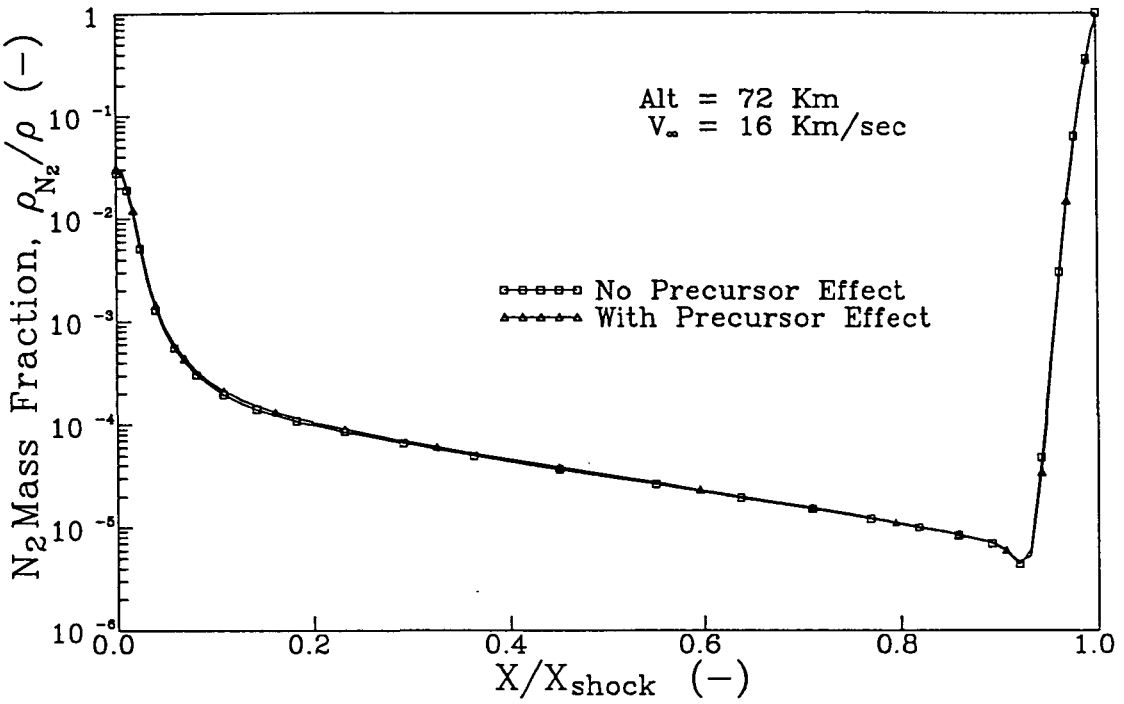

Figure 25: N_2 Mass Fraction in the Shock Layer;
(Alt = 72 Km, V_∞ = 16 Km/sec)

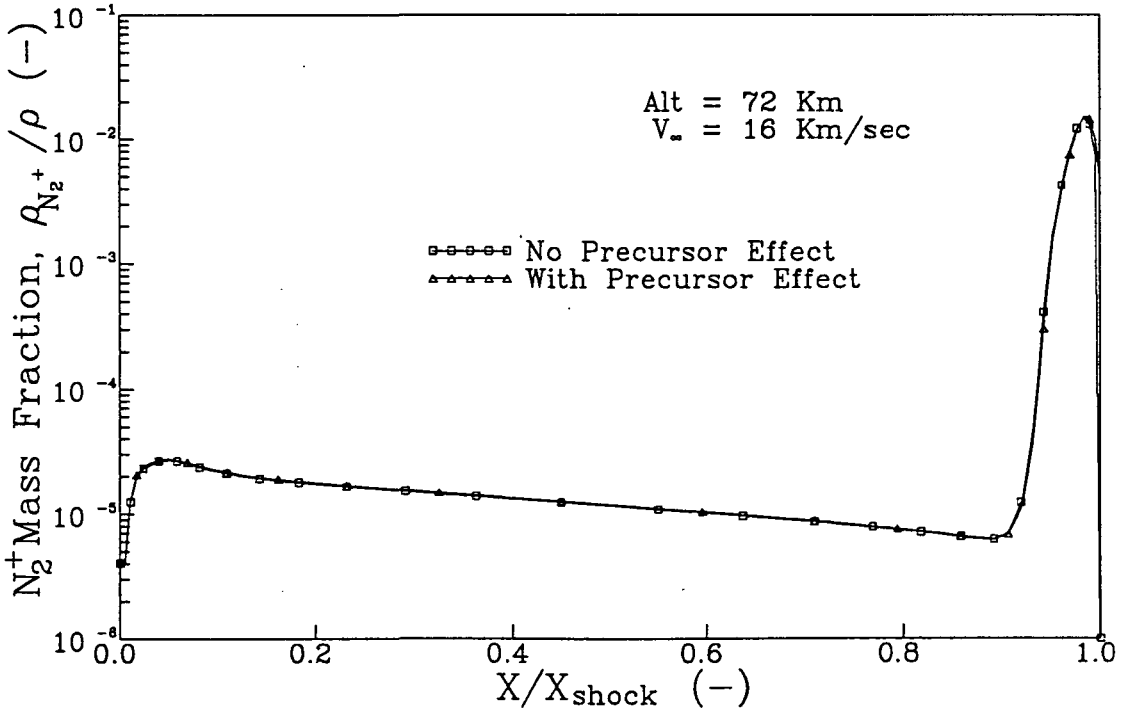

Figure 26: N_2^+ Mass Fraction in the Shock Layer;
(Alt = 72 Km, V_∞ = 16 Km/sec)

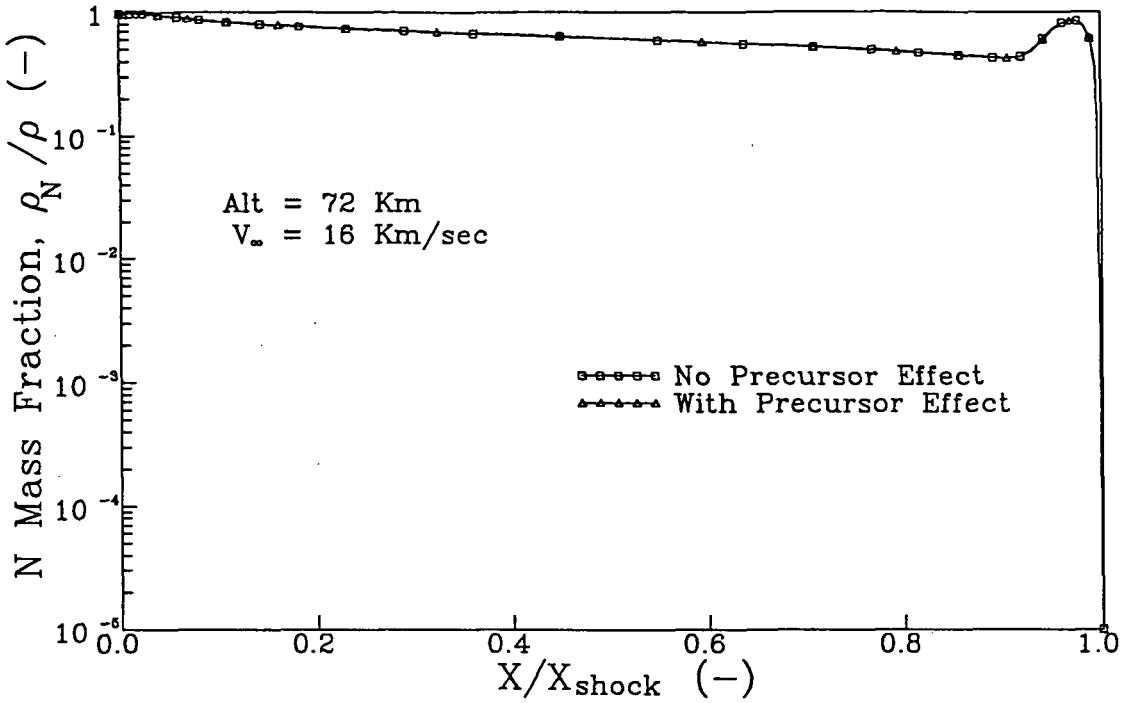

Figure 27: N Mass Fraction in the Shock Layer;
(Alt = 72 Km, V_∞ = 16 Km/sec)

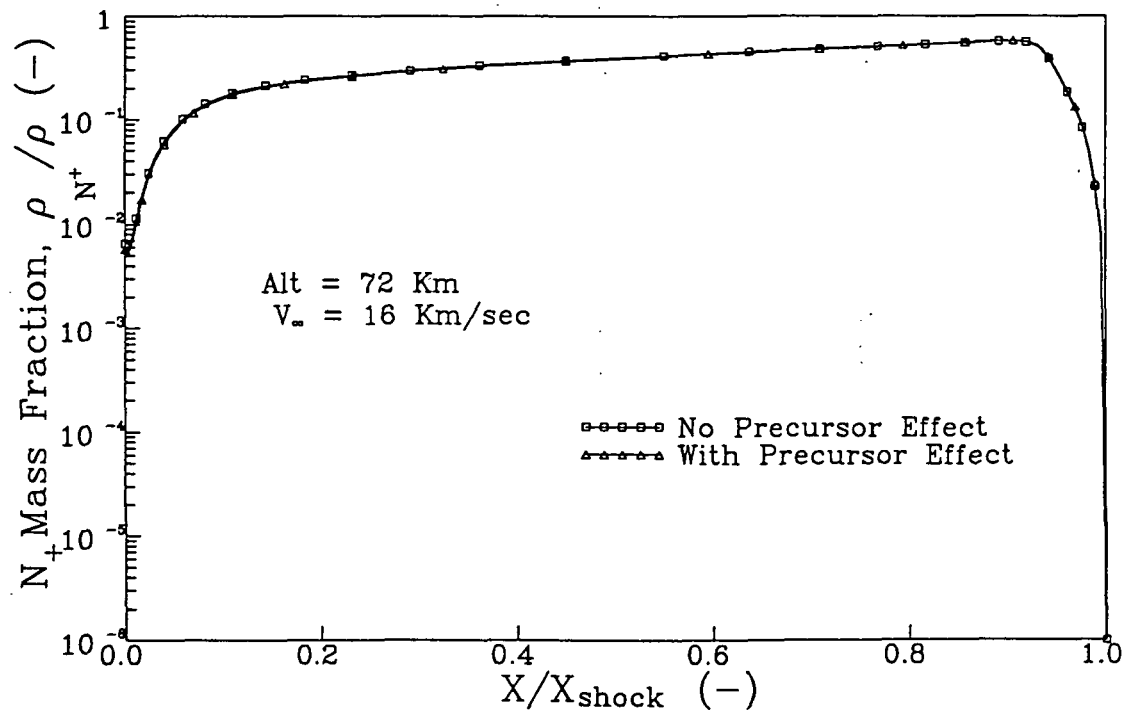

Figure 28: N^+ Mass Fraction in the Shock Layer;
(Alt = 72 Km, V_∞ = 16 Km/sec)

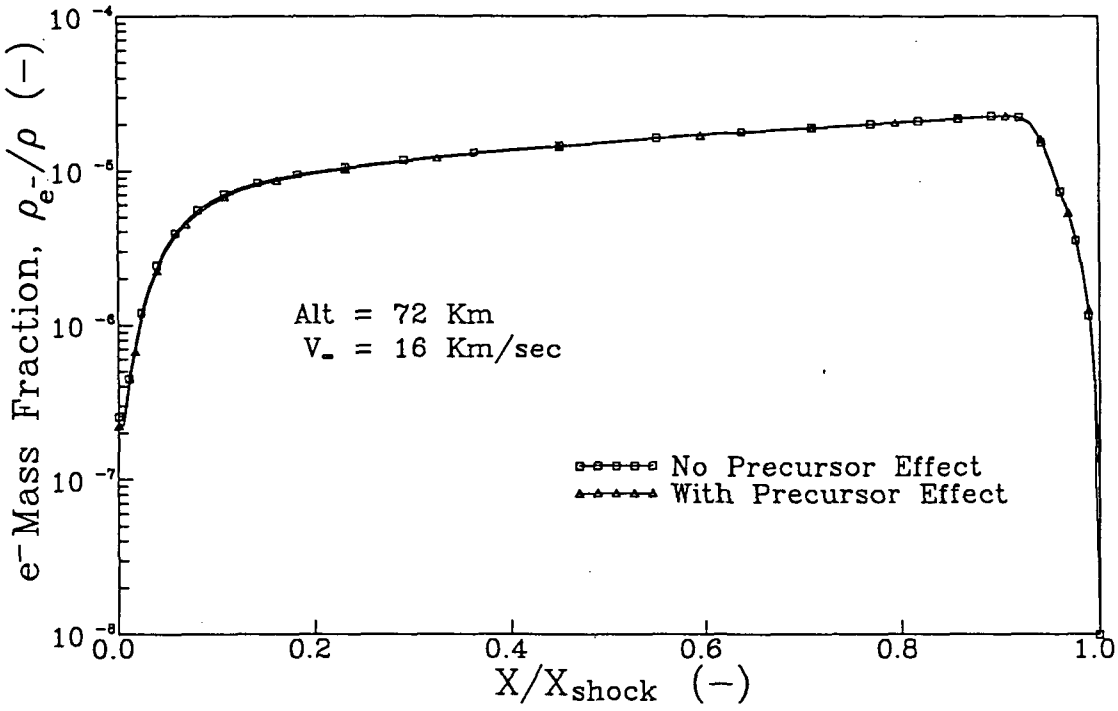

Figure 29: e^- Mass Fraction in the Shock Layer;
(Alt = 72 Km, V_∞ = 16 Km/sec)

negligible effect on the gas in the shock layer. Likewise, there was no measurable change in the radiative heat transfer to the body.

The primary change due to the inclusion of the precursor was in the conditions of the gas immediately behind the shock wave. These effects can be seen more clearly in Figures 30 to 35 which show the electron temperature and the mass fractions in the chemically reacting nonequilibrium region. Neglecting the precursor, the mass fractions for the free electrons, ions and atoms were zero upon crossing the shock; however, including the effects of the precursor these mass fractions had nonzero values. Likewise, including the effects of the precursor resulted in a slight increase in the electron temperature in the region immediately behind the shock front.

The case discussed above was representative of all of the cases calculated for this study and the remaining cases, being less extreme, had even less effect on the shock layer and radiative heat transfer to the body. Therefore, for the entry conditions of interest to an aerocapture vehicle entering the earth's atmosphere upon return from Mars, the precursor region can reasonably be neglected in the calculation of the shock layer.

Parametric Studies

Figures 36 to 45 show the heavy particle temperature, electron/electronic temperature, total enthalpy, electron/electronic energy, pressure and mass fractions for cases 1, 2 and 3. All three of these cases were at a velocity of 16 Km/sec; however, each case was at a different altitude, 72 Km, 75 Km and 80 Km. The shock standoff

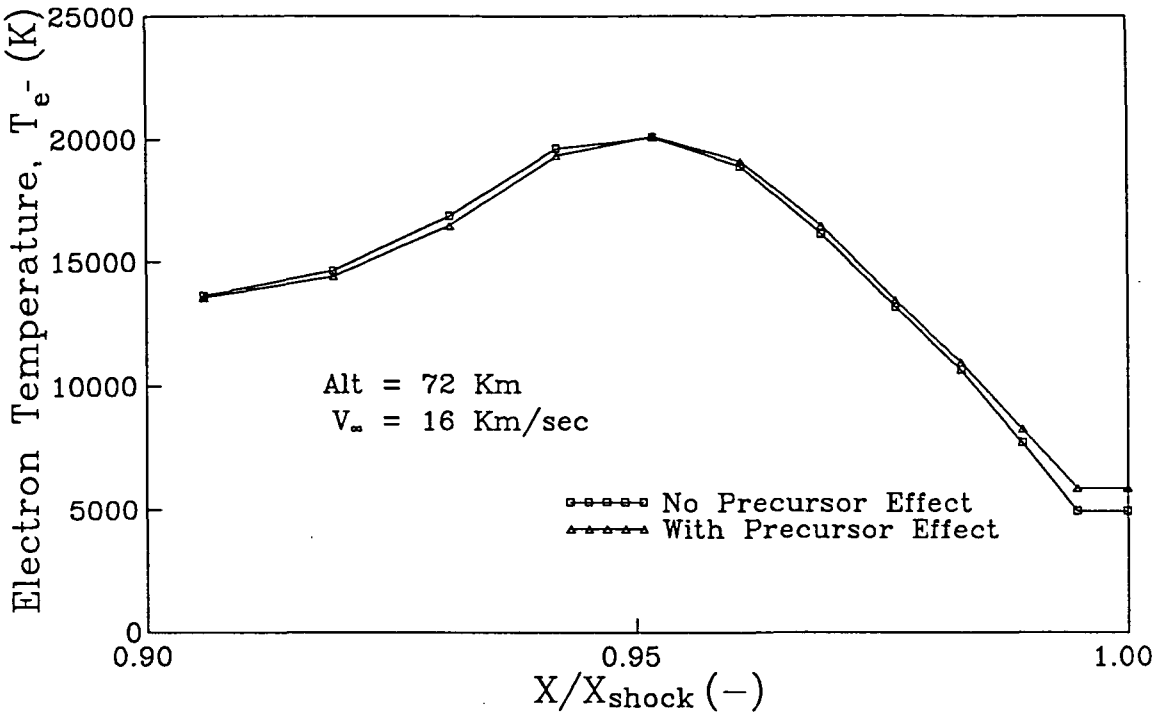

Figure 30: Electron Temperature in the Nonequilibrium Region of the Shock Layer; (Alt = 72 Km, V_∞ = 16 Km/sec)

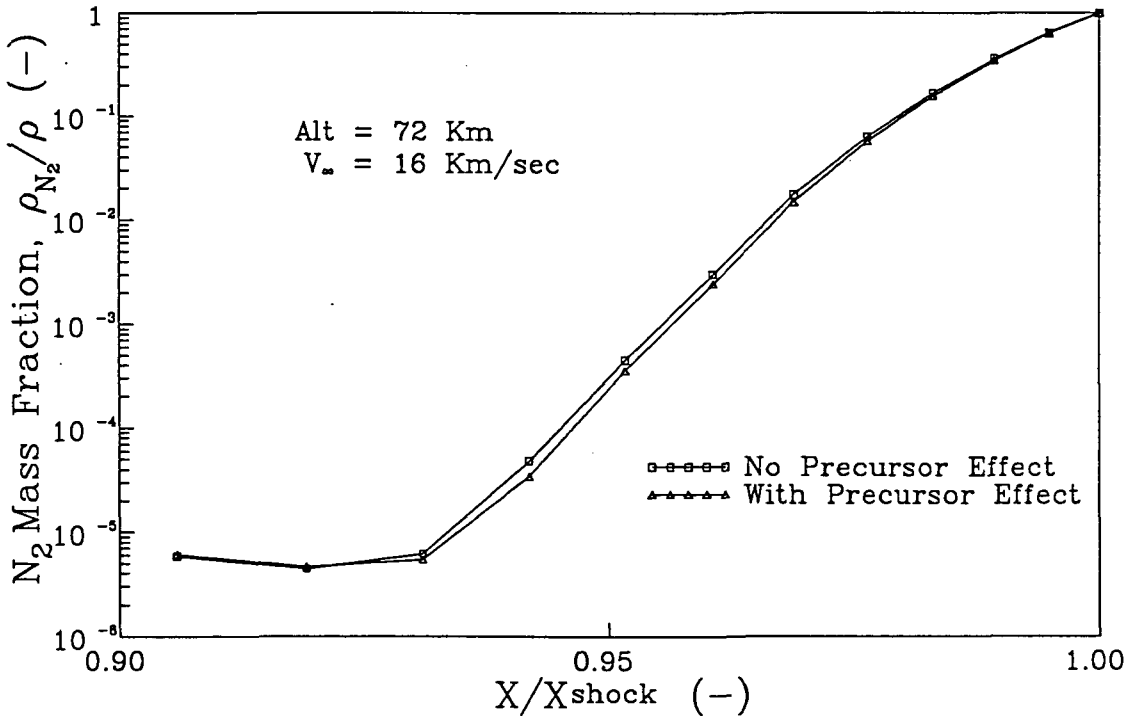

Figure 31: N_2 Mass Fraction in the Nonequilibrium Region of the Shock Layer; (Alt = 72 Km, V_∞ = 16 Km/sec)

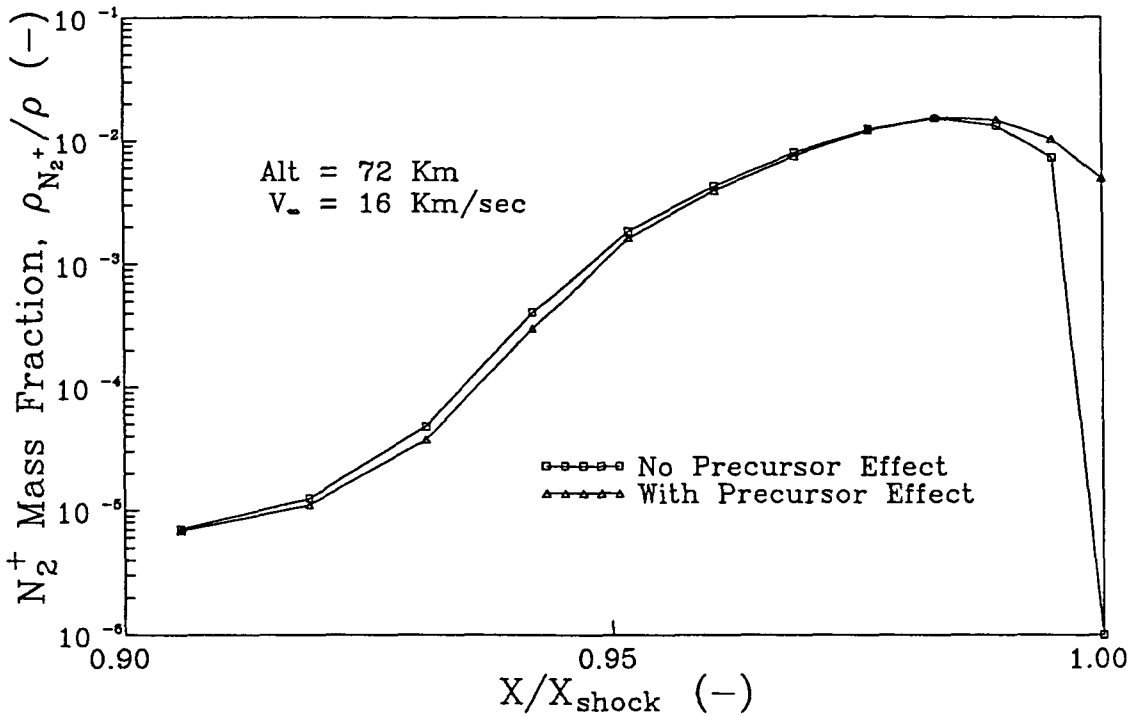

Figure 32: N_2^+ Mass Fraction in the Nonequilibrium Region of the Shock Layer; (Alt = 72 Km, V_∞ = 16 Km/sec)

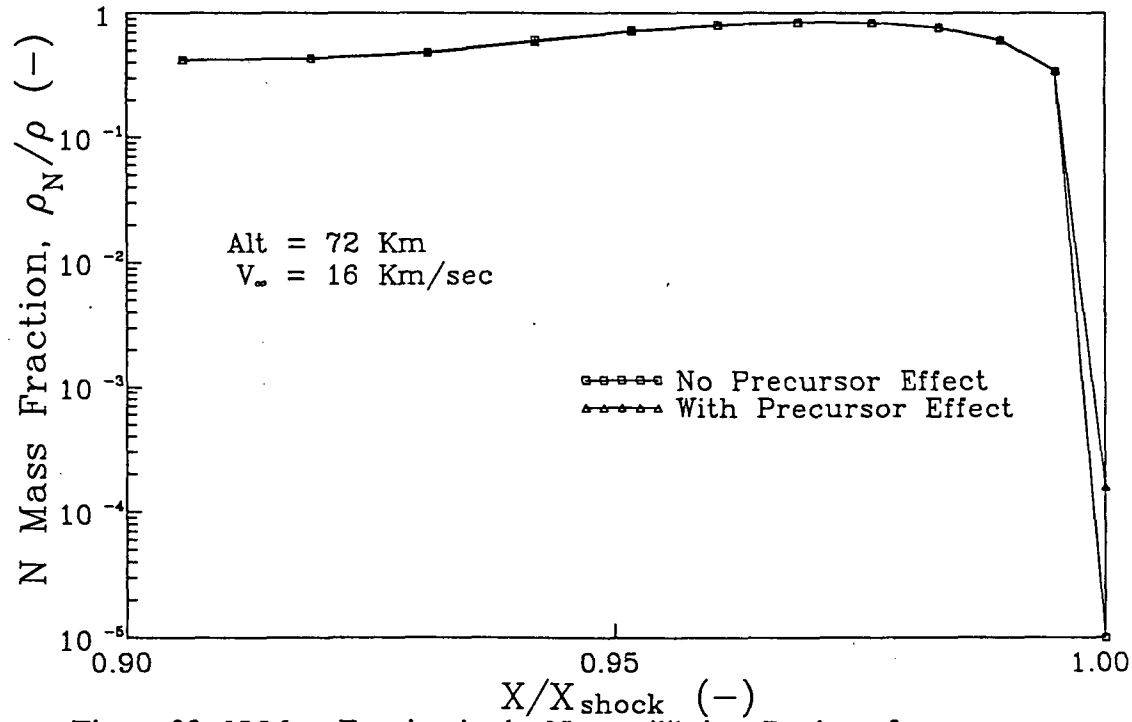

Figure 33: N Mass Fraction in the Nonequilibrium Region of the Shock Layer; (Alt = 72 Km, V_∞ = 16 Km/sec)

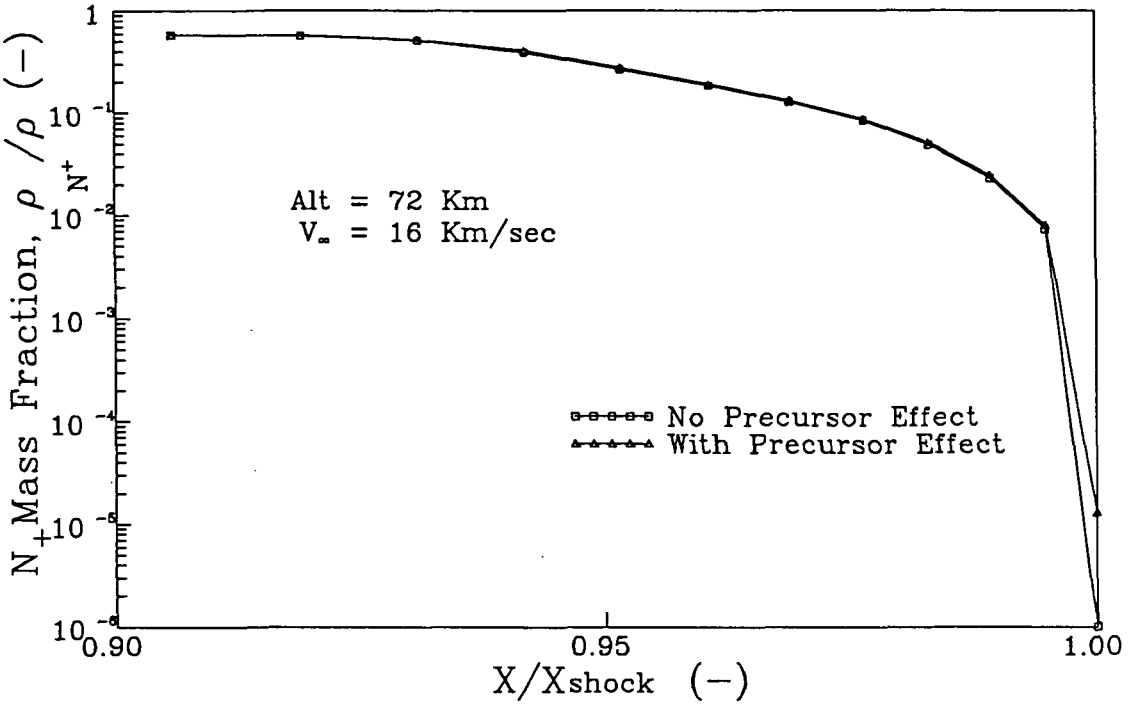

Figure 34: N^+ Mass Fraction in the Nonequilibrium Region of the Shock Layer; (Alt = 72 Km, V_∞ = 16 Km/sec)

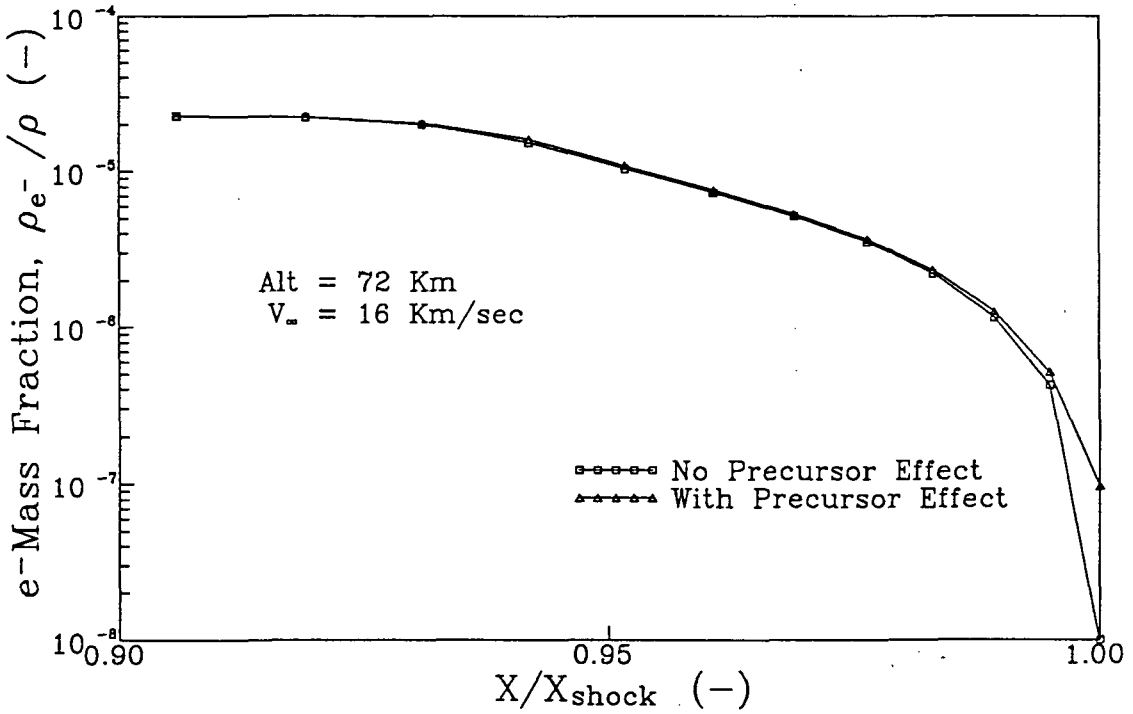

Figure 35: e^- Mass Fraction in the Nonequilibrium Region of the Shock Layer; (Alt = 72 Km, V_∞ = 16 Km/sec)

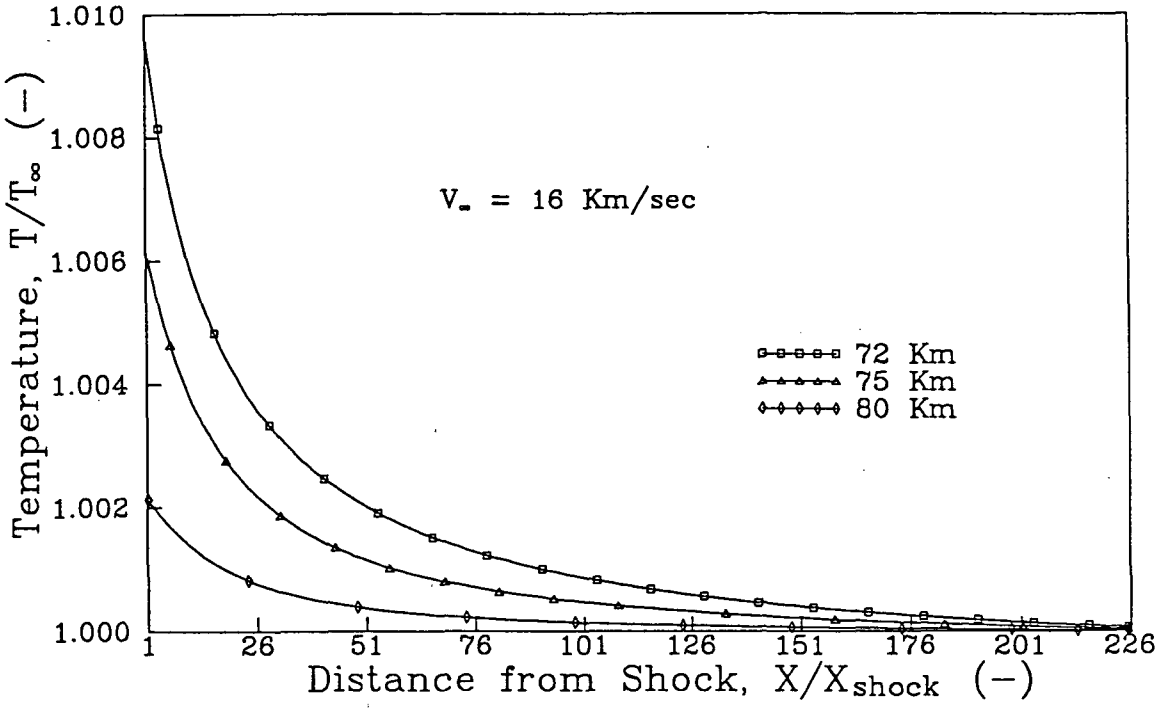

Figure 36: The Variation of Heavy Particle Temperature with Altitude in the Precursor Region; (Alt = 72, 75 and 80 Km, V_∞ = 16 Km/sec)

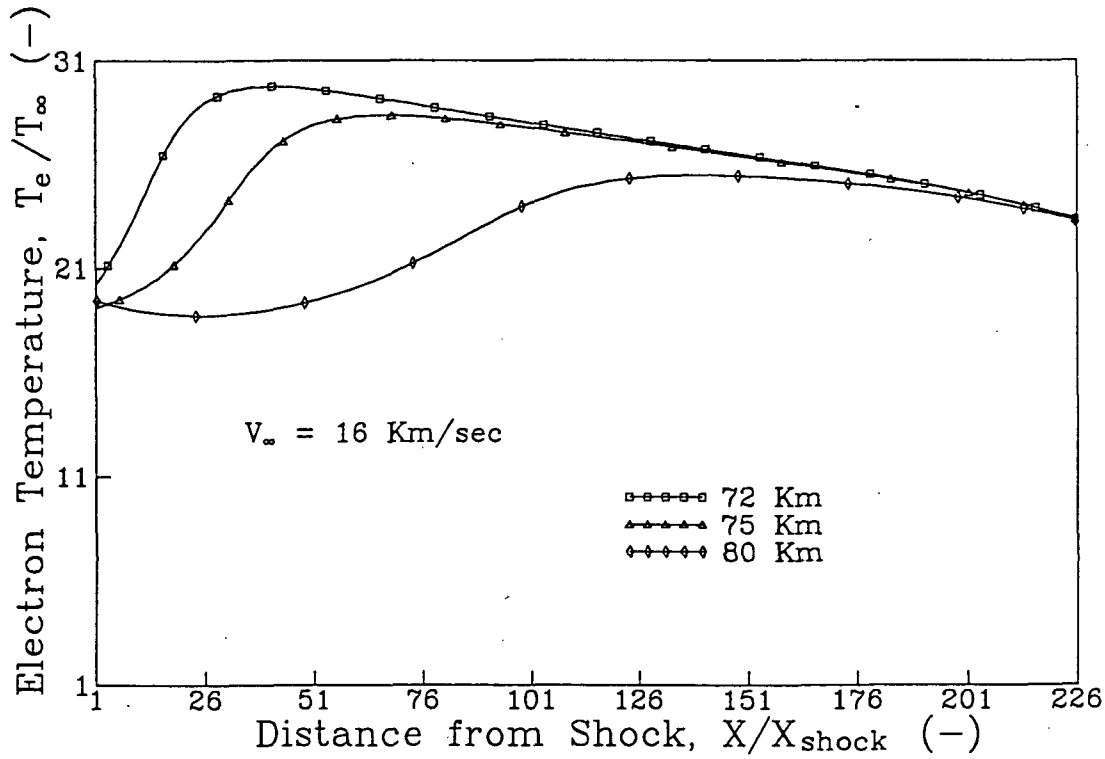

Figure 37: The Variation of Electron/Electronic Temperature with Altitude in the Precursor Region; (Alt = 72, 75 and 80 Km, V_∞ = 16 Km/sec)

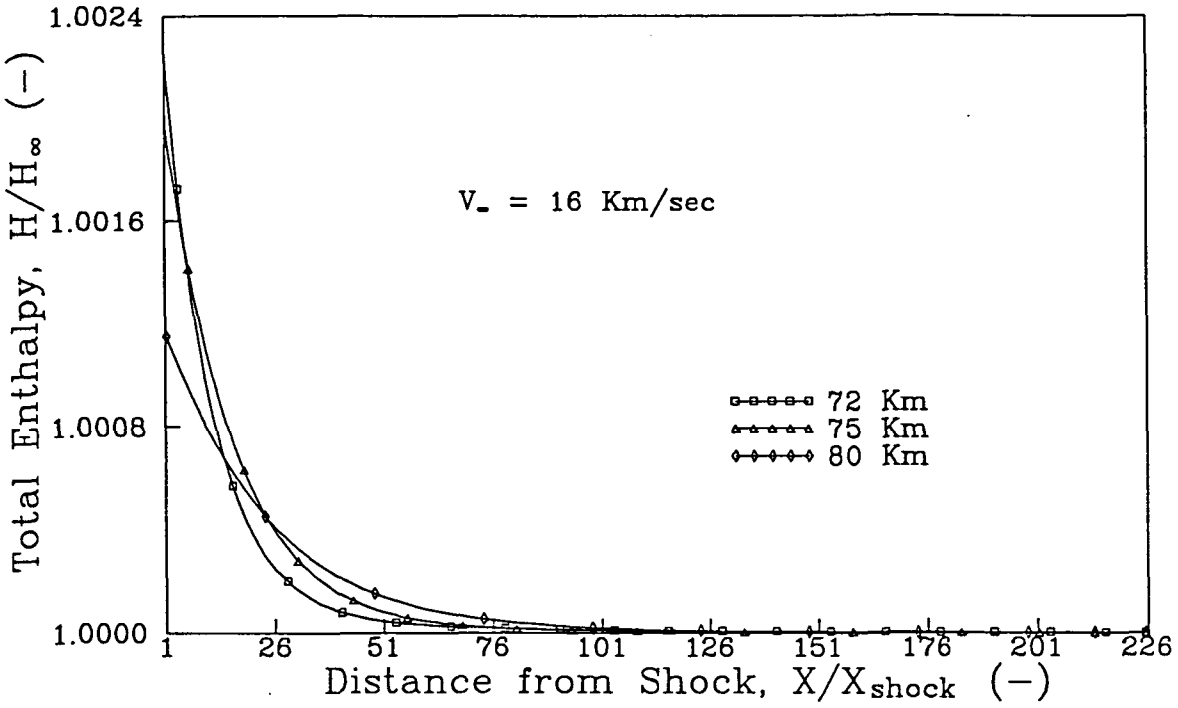

Figure 38: The Variation of Total Enthalpy with Altitude in the Precursor Region; (Alt = 72, 75 and 80 Km, V_∞ = 16 Km/sec)

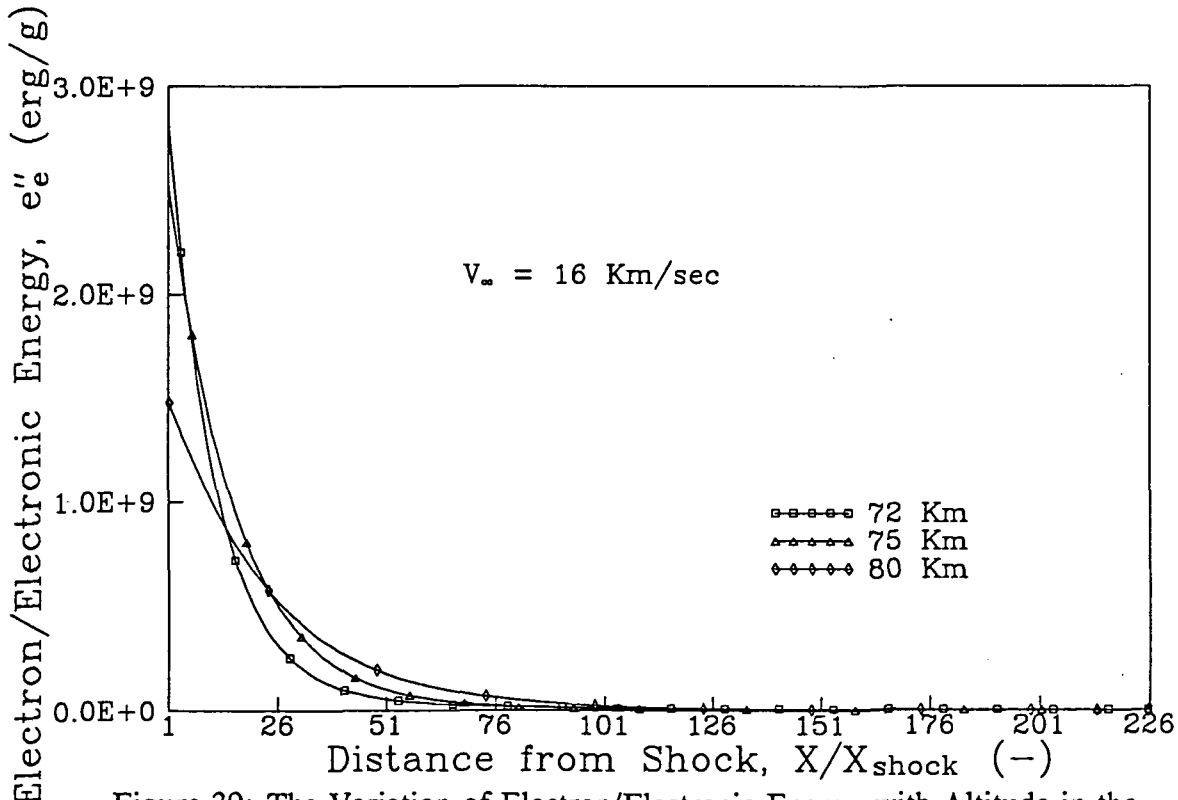

Figure 39: The Variation of Electron/Electronic Energy with Altitude in the Precursor Region; (Alt = 72, 75 and 80 Km, V_∞ = 16 Km/sec)

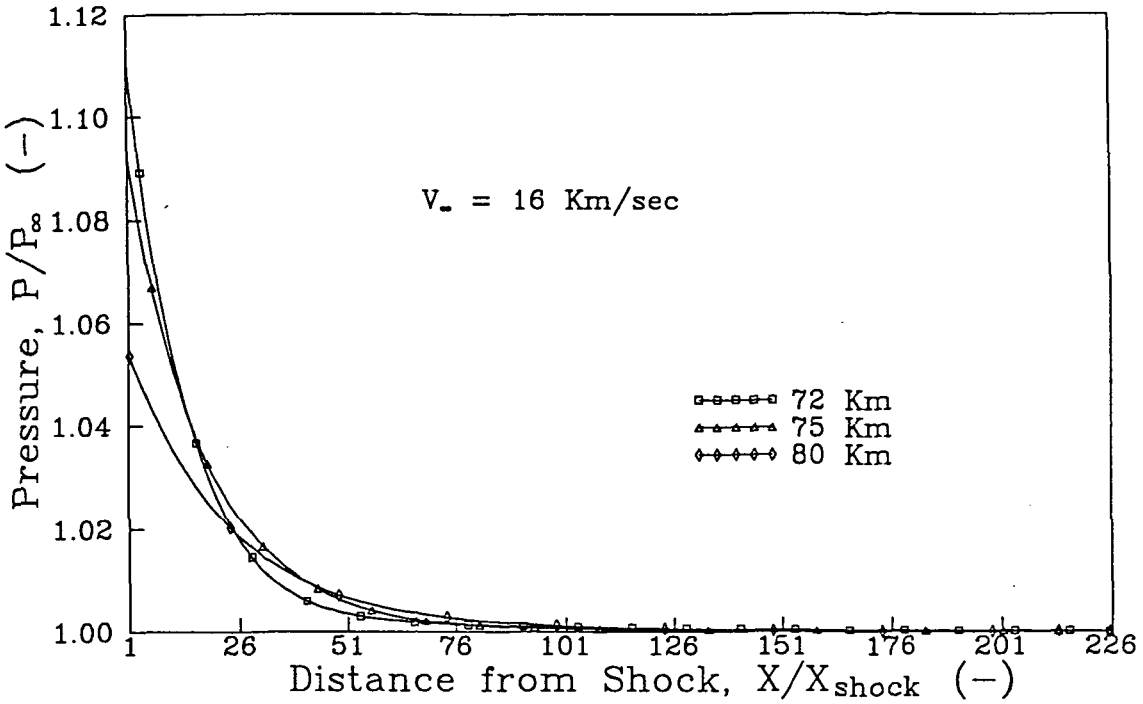

Figure 40: The Variation of Pressure with Altitude in the Precursor Region; (Alt = 72, 75 and 80 Km, V_∞ = 16 Km/sec)

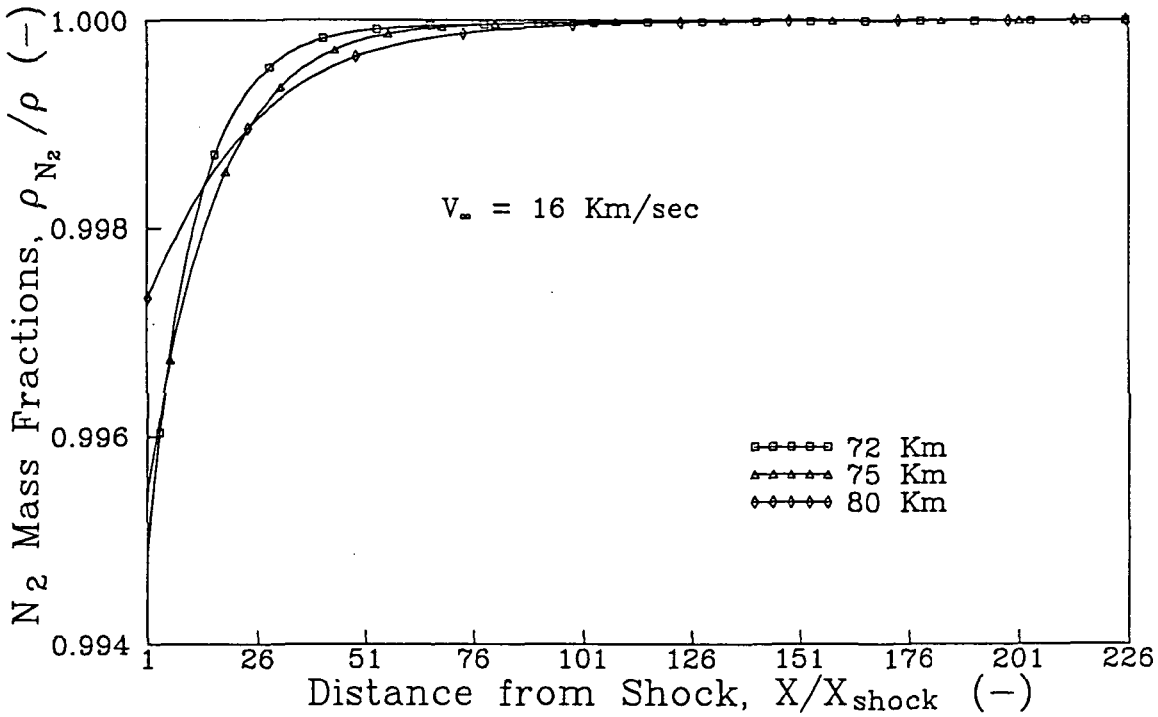

Figure 41: The Variation of N_2 Mass Fraction with Altitude in the Precursor Region; (Alt = 72, 75 and 80 Km, V_∞ = 16 Km/sec)

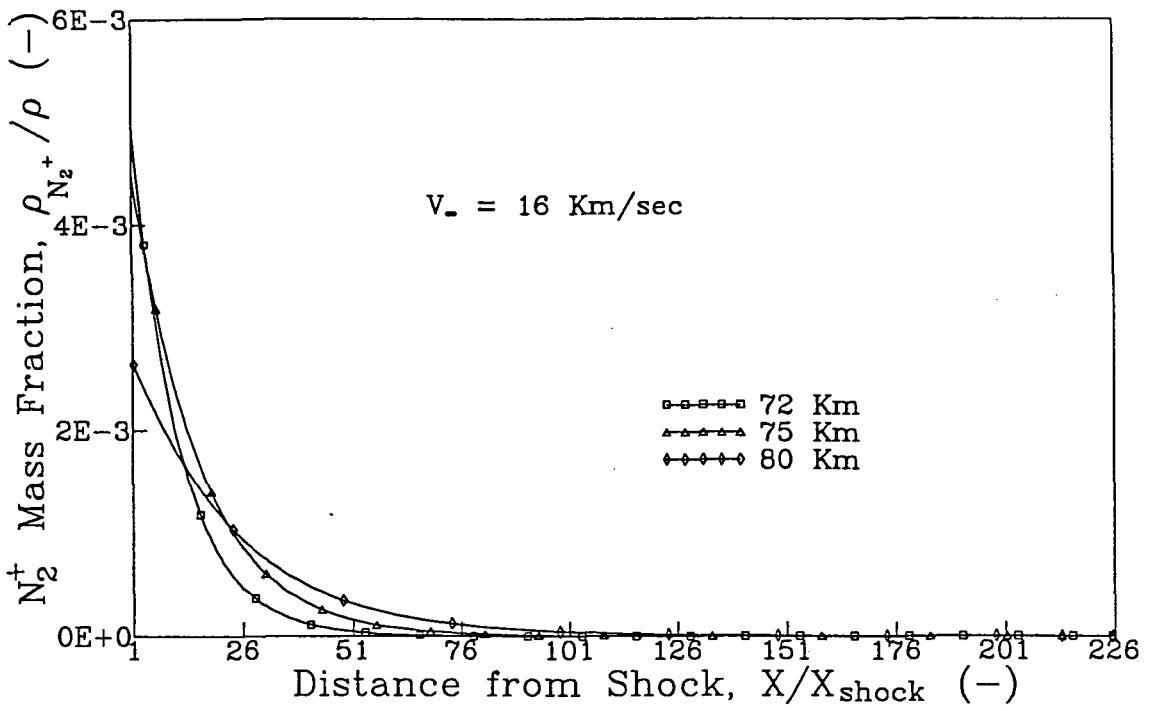

Figure 42: The Variation of N_2^+ Mass Fraction with Altitude in the Precursor Region; (Alt = 72, 75 and 80 Km, V_∞ = 16 Km/sec)

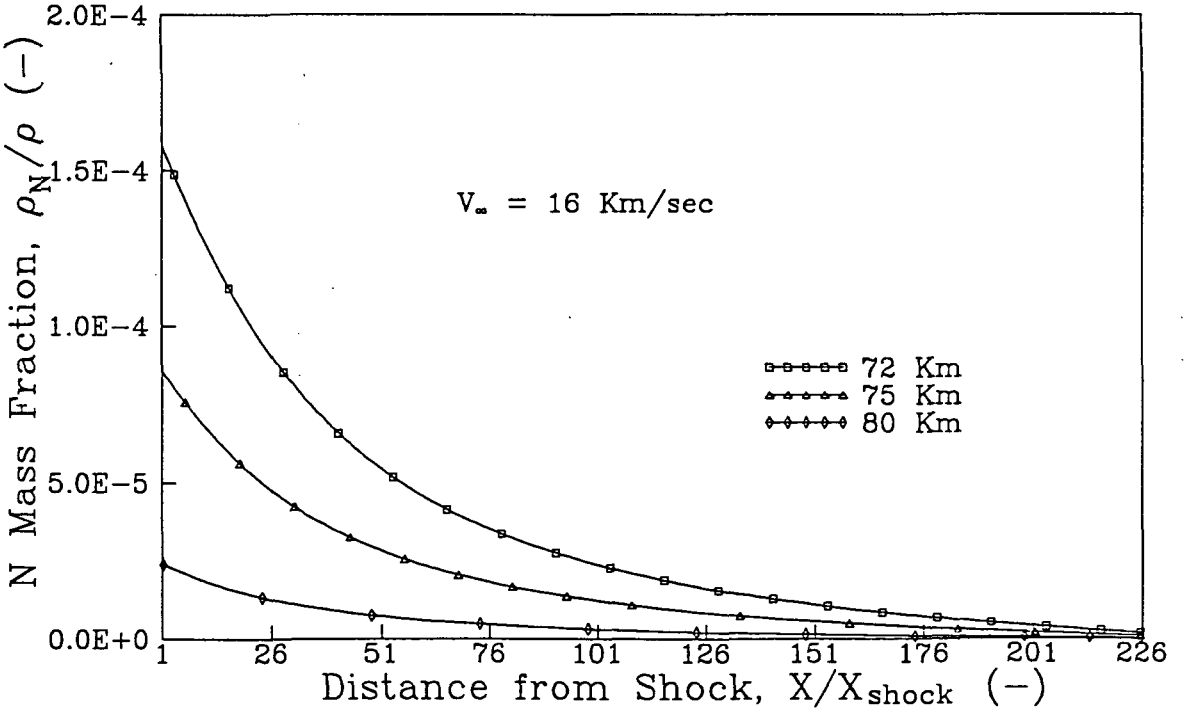

Figure 43: The Variation N Mass Fraction with Altitude in the Precursor Region; (Alt = 72, 75 and 80 Km, V_∞ = 16 Km/sec)

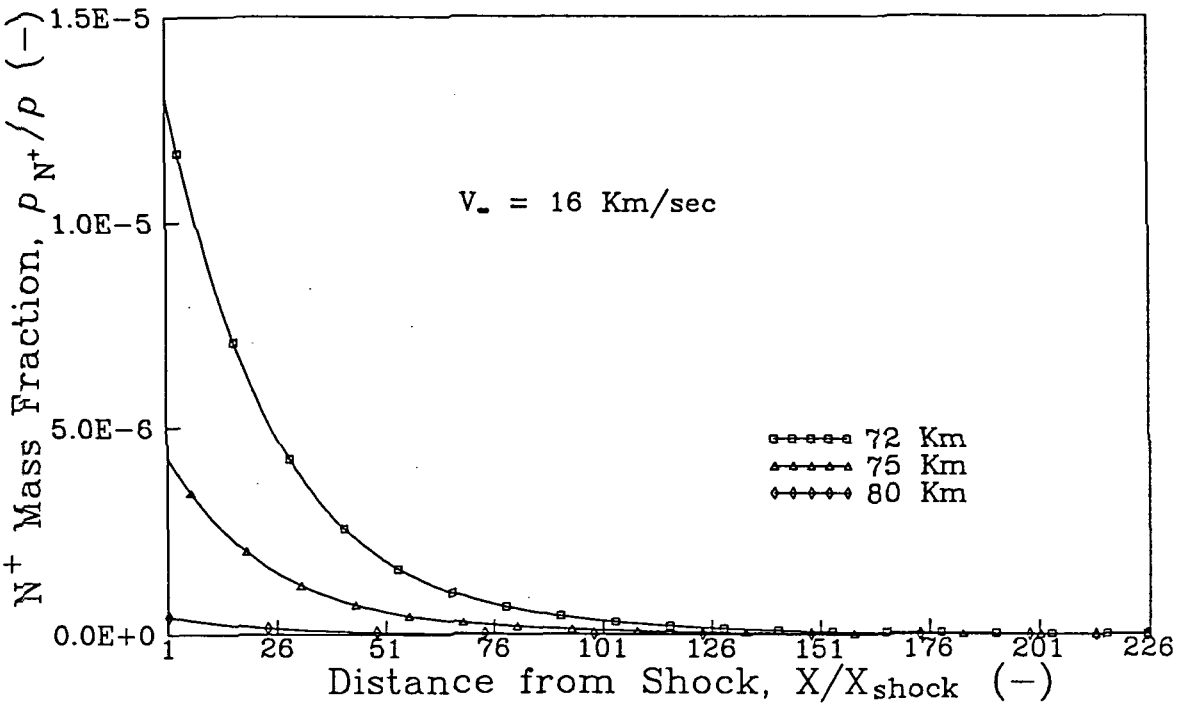

Figure 44: The Variation of N^+ Mass Fraction with Altitude in the Precursor Region; (Alt = 72, 75 and 80 Km, V_∞ = 16 Km/sec)

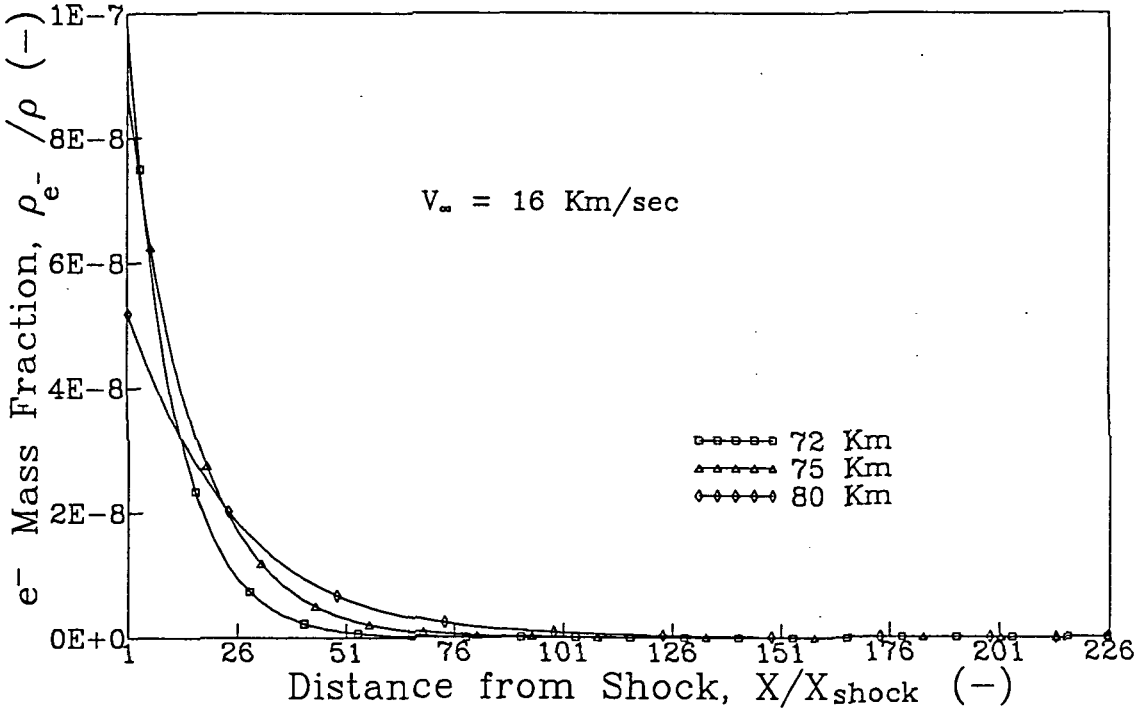

Figure 45: The Variation of e^- Mass Fraction with Altitude in the Precursor Region; (Alt = 72, 75 and 80 Km, V_∞ = 16 Km/sec)

distance and radiative transfer through the shock wave for each of these cases are given in Table 4.

From these figures, it can be seen that at a constant velocity as the altitude decreased the magnitude of the changes in the precursor increased. This inverse relationship between the magnitude of the changes in the precursor and altitude corresponded with the trends observed by Dobbins[25] as well as those observed by Tiwari and Szema[34] and was a result of two factors. First and foremost, as shown in Figure 46, with the decrease in altitude the radiative flux through the shock increased due to an increase in the extent of the equilibrium region in the shock layer. Second, with the increase in density at the lower altitudes, a larger percentage of the radiation passing through the shock was absorbed before being attenuated due to geometry.

It should also be noted that as the altitude decreased, the length of the precursor region decreased. This change was a result of the increased density at lower altitudes, which caused the radiative mean free path to decrease. Hence, the radiation was absorbed in a shorter distance ahead of the shock. This trend was also predicted by previous studies.[15,34]

Figures 47 to 56 give the heavy particle temperature, electron/electronic temperature, total enthalpy, electron/electronic energy, pressure and mass fractions for cases 3, 4, 5 and 6. All of these cases were at an altitude of 80 Km and the freestream velocities ranged from 10 to 16 Km/sec. From these figures, it can be seen that at a constant altitude, as the freestream velocity increased the magnitude of the changes in the precursor also increased. This trend was a result of the increase in the equilibrium

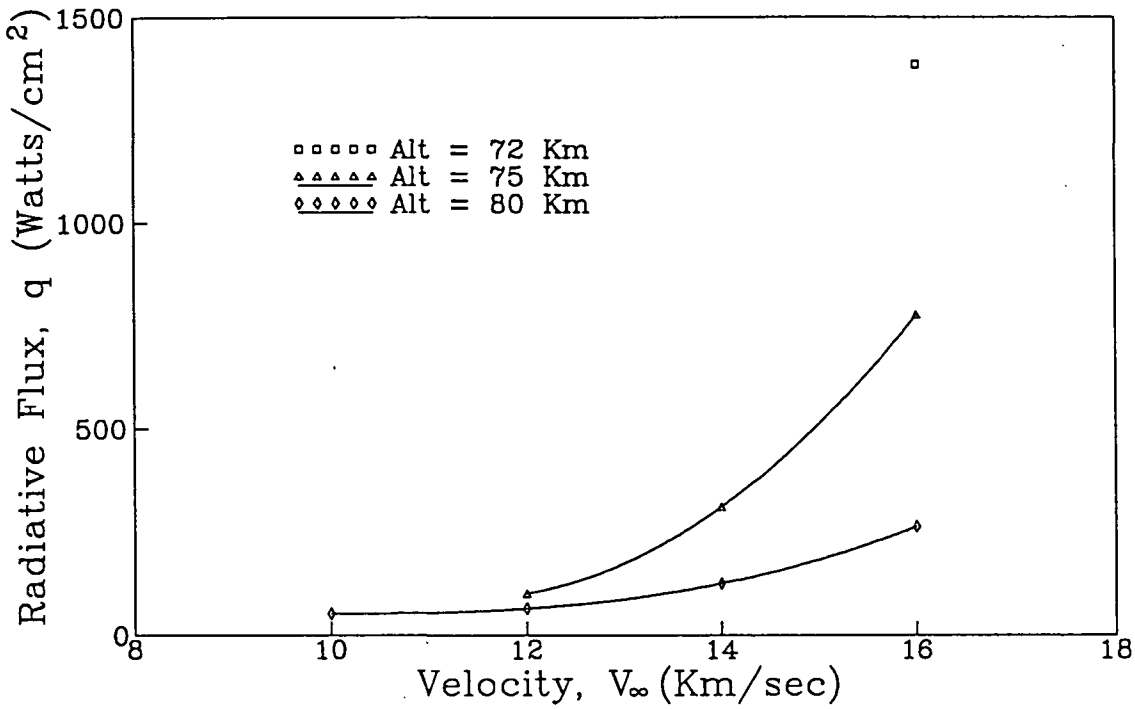

Figure 46: Variation of the Radiative Flux Through the Shock with Velocity and Altitude

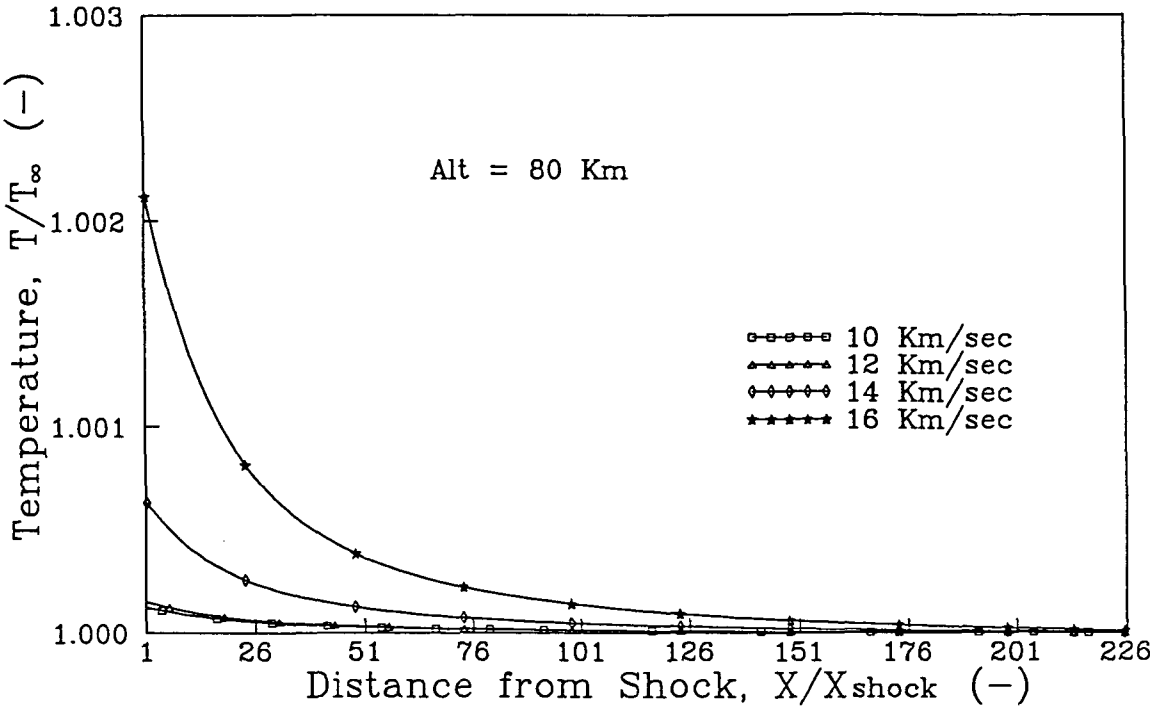

Figure 47: The Variation of Heavy Particle Temperature with Velocity in the Precursor Region; (Alt = 80 Km, V_∞ = 10, 12, 14 and 16 Km/sec)

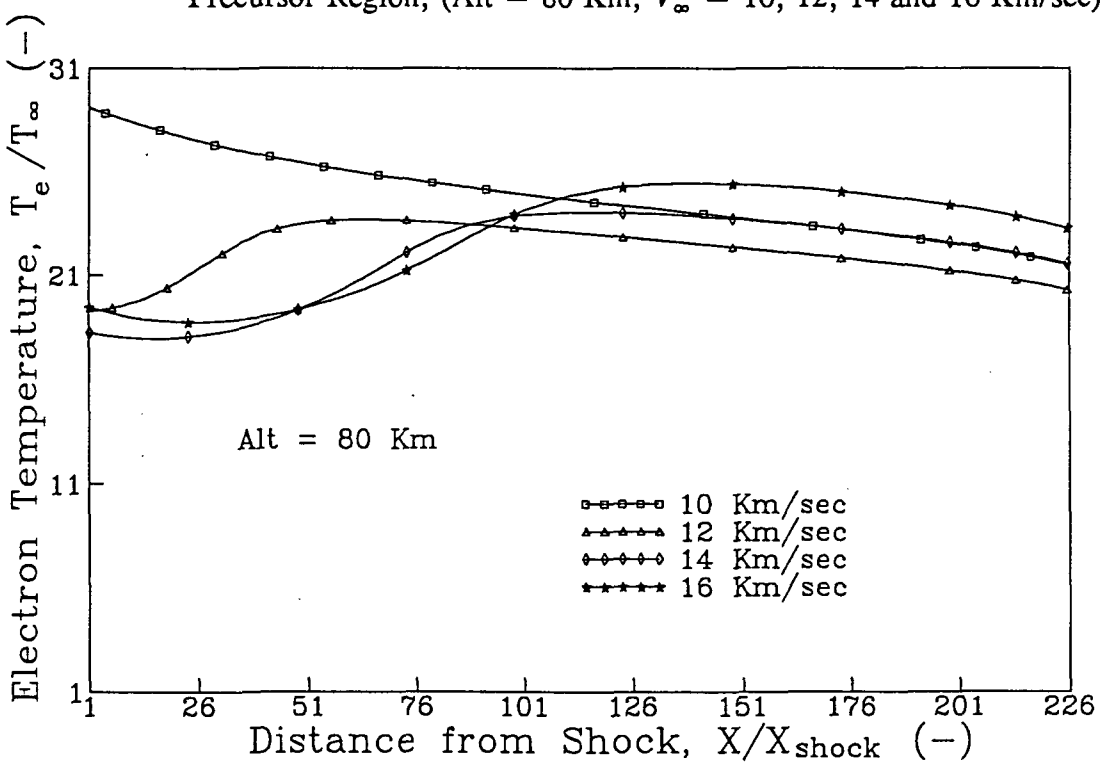

Figure 48: The Variation of Electron/Electronic Temperature with Velocity in the Precursor Region; (Alt = 80 Km, V_∞ = 10, 12, 14 and 16 Km/sec)

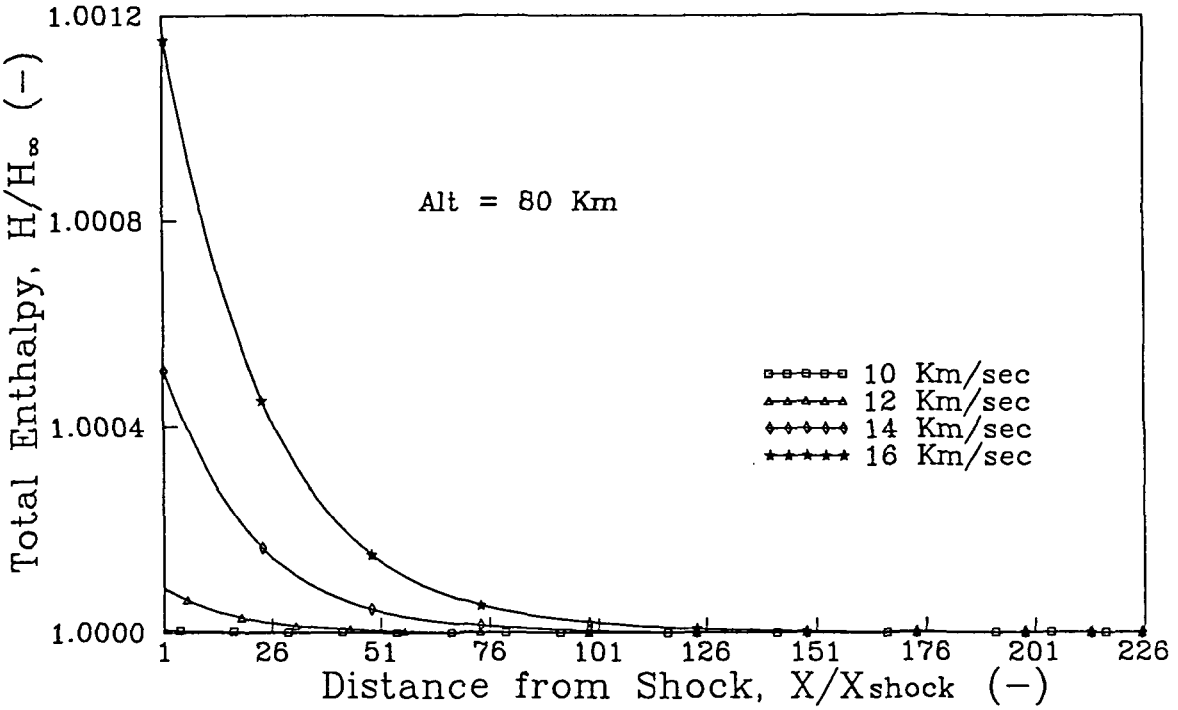

Figure 49: The Variation of Total Enthalpy with Velocity in the Precursor Region; (Alt = 80 Km, V_∞ = 10, 12, 14 and 16 Km/sec)

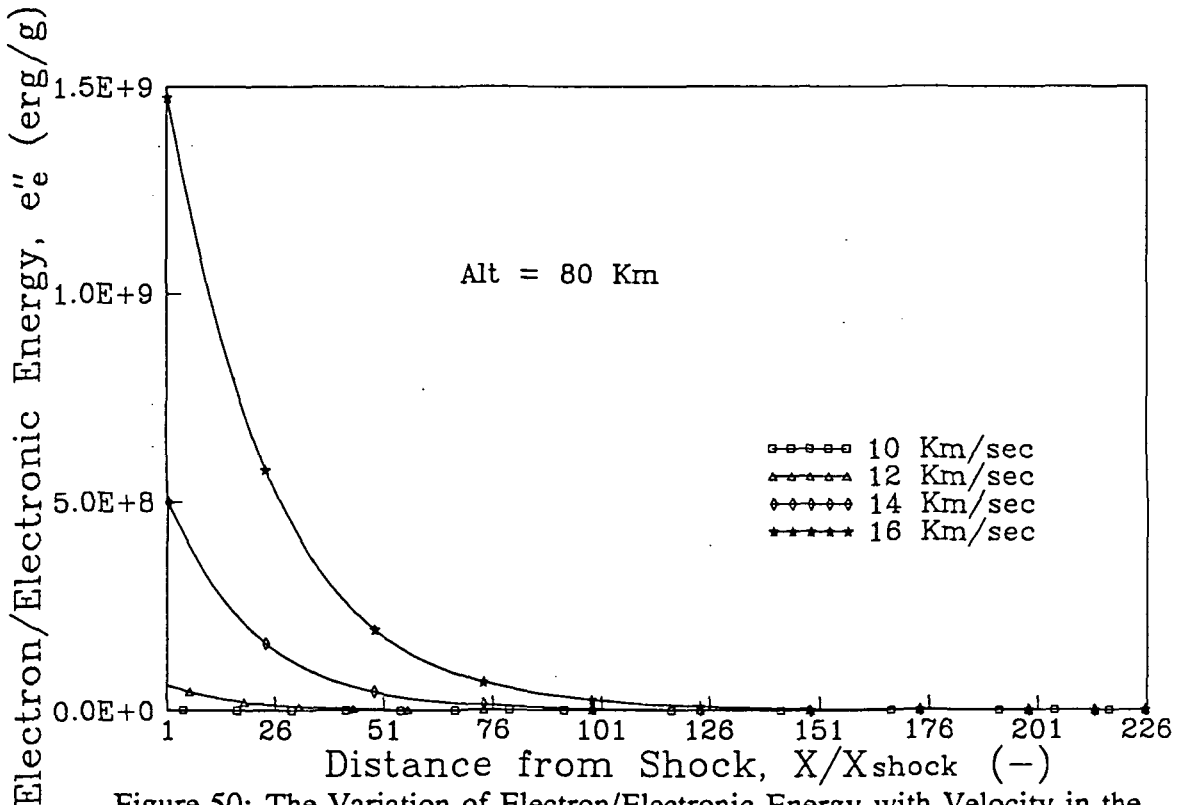

Figure 50: The Variation of Electron/Electronic Energy with Velocity in the Precursor Region; (Alt = 80 Km, V_∞ = 10, 12, 14 and 16 Km/sec)

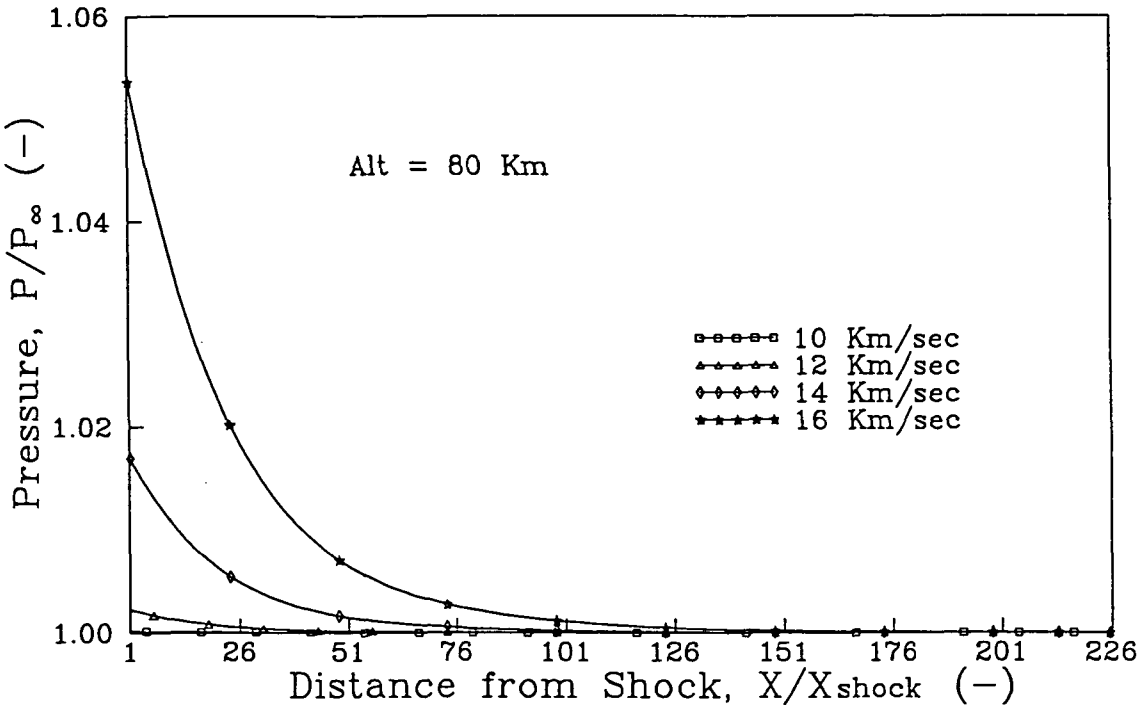

Figure 51: The Variation of Pressure with Velocity in the Precursor Region; (Alt = 80 Km, V_∞ = 10, 12, 14 and 16 Km/sec)

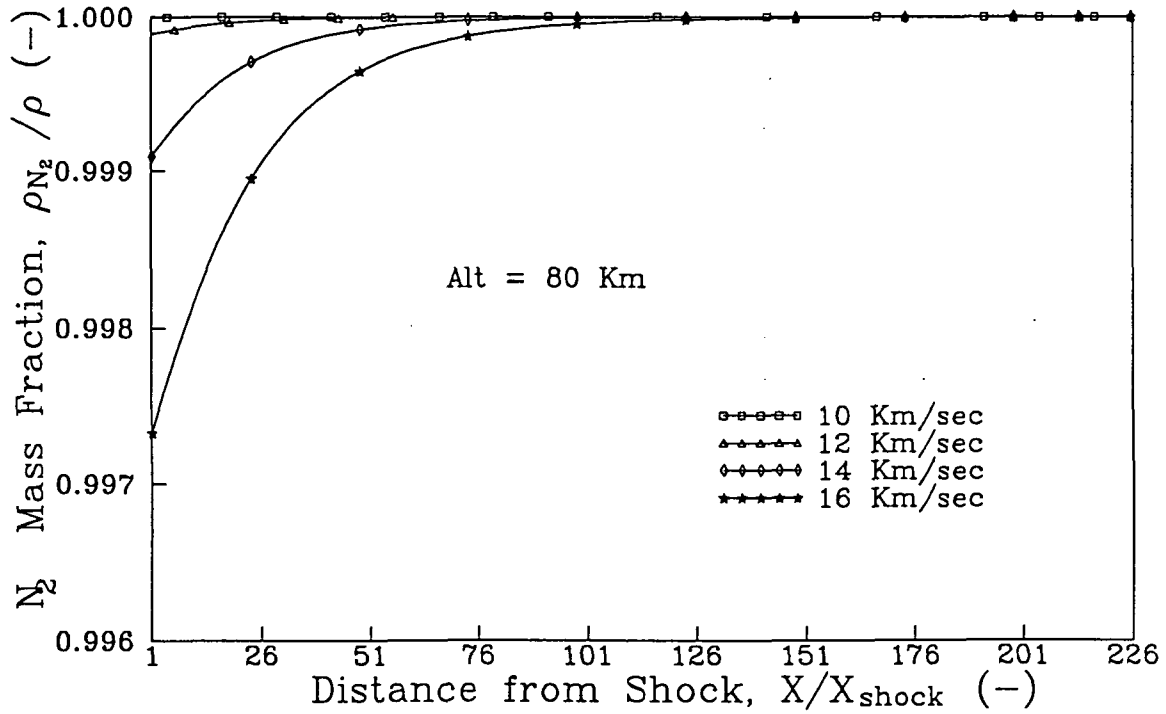

Figure 52: The Variation of N_2 Mass Fraction with Velocity in the Precursor Region; (Alt = 80 Km, V_∞ = 10, 12, 14 and 16 Km/sec)

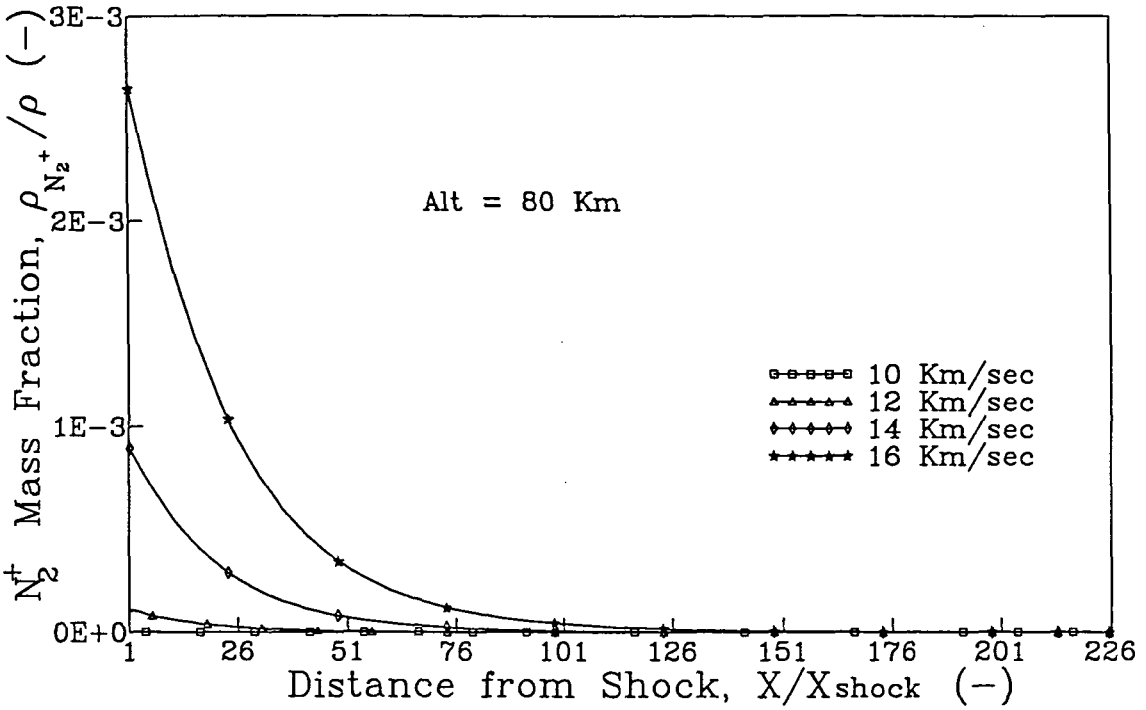

Figure 53: The Variation of N_2^+ Mass Fraction with Velocity in the Precursor Region; (Alt = 80 Km, V_∞ = 10, 12, 14 and 16 Km/sec)

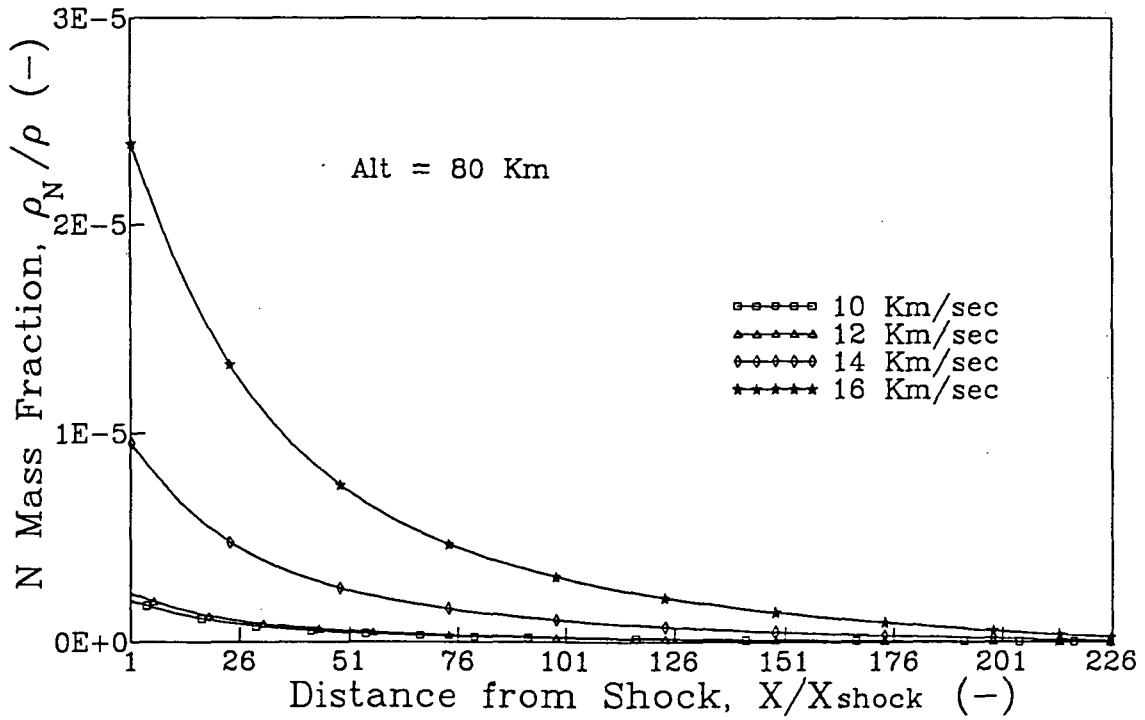

Figure 54: The Variation N Mass Fraction with Velocity in the Precursor Region; (Alt = 80 Km, V_∞ = 10, 12, 14 and 16 Km/sec)

C-2

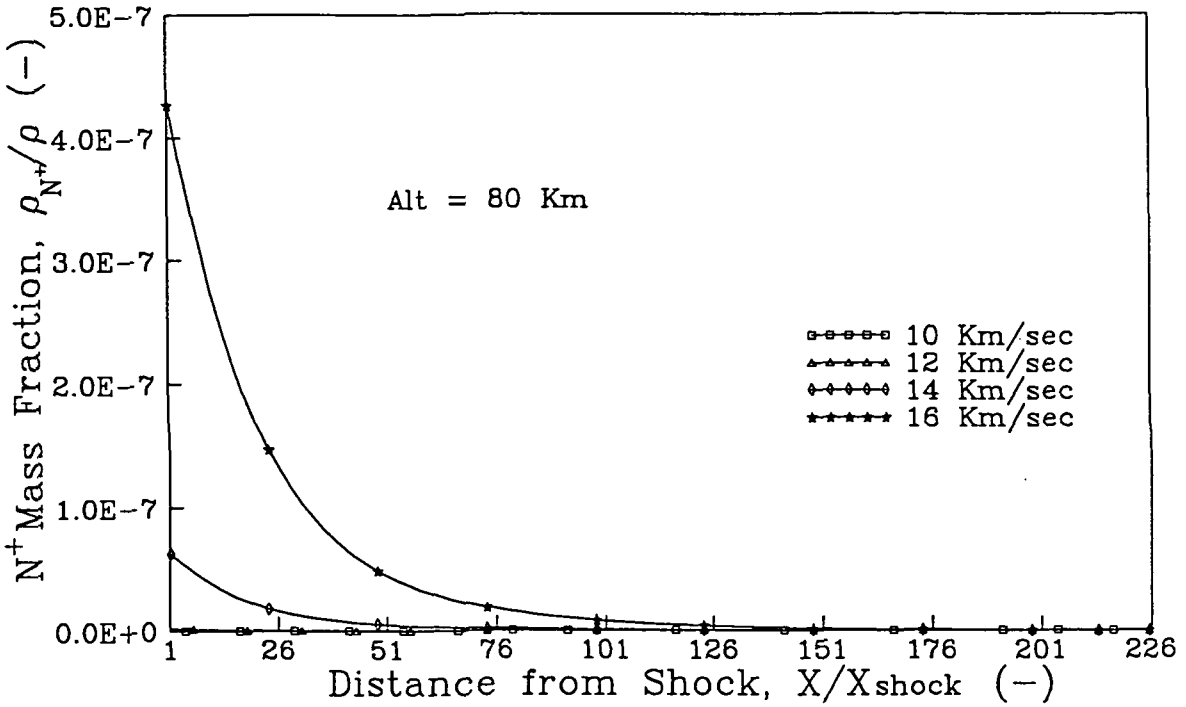

Figure 55: The Variation of N^+ Mass Fraction with Velocity in the Precursor Region; (Alt = 80 Km, V_∞ = 10, 12, 14 and 16 Km/sec)

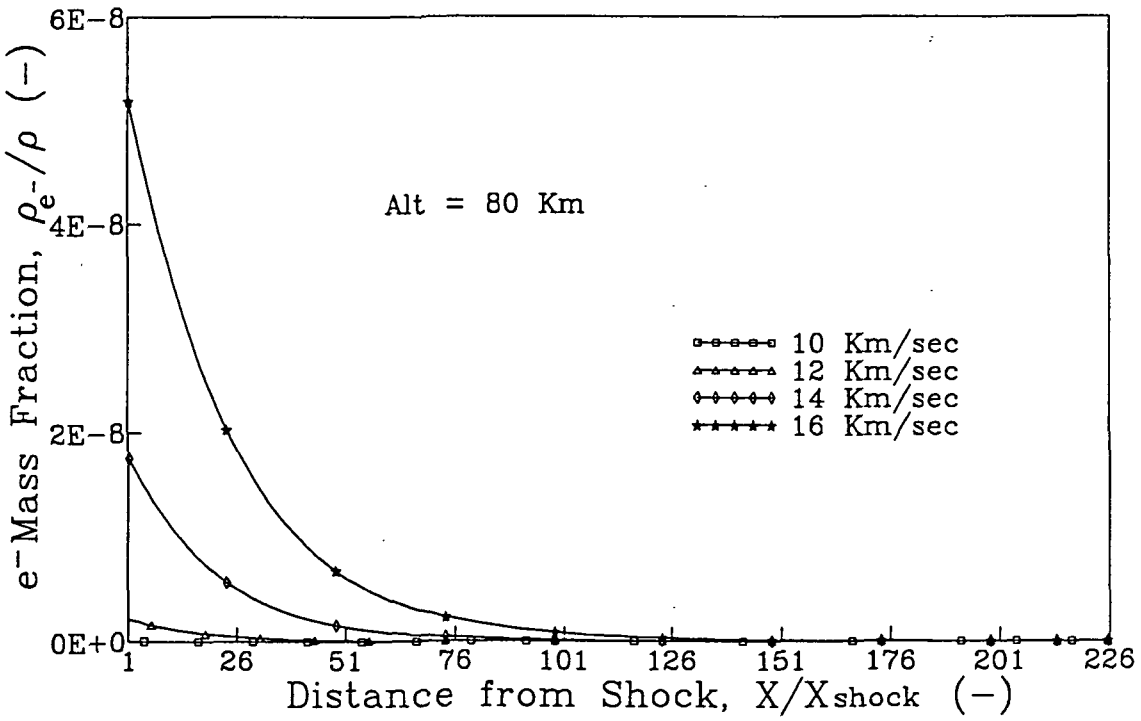

Figure 56: The Variation of e^- Mass Fraction with Velocity in the Precursor Region; (Alt = 80 Km, V_∞ = 10, 12, 14 and 16 Km/sec)

temperature in the shock layer as the velocity increased and the accompanying rise in the radiative flux through the shock front, shown in Figure 46; this trend is also in general agreement with the results and predictions of previous researchers.[13,25,34] It is also evident from these figures that the precursor thickness increased with velocity, again as a result of the increased radiative flux with velocity. As the radiative energy passing through the shock increased, a larger distance was required for this energy to be absorbed or attenuated ahead of the shock front.

The results presented in this section give the same general trends as those shown in previous research for monatomic gases and for hydrogen. Likewise, the electron number densities immediately ahead of the shock front are of the same order of magnitude as those measured by Omura and Presley for a nitrogen gas.[12,13] In their research, they measured electron number densities of $1x10^{12}$ /cm^3 for an 11.89 Km/sec case at a freestream pressure of 266 dyn/cm^2 in a nitrogen gas. The electron number density immediately ahead of the shock for case 5, p_∞ = 10.72 dyn/cm^2 and V_∞ = 12 Km/sec, was $5.5x10^{10}$ /cm^3. The trend of the results presented herein with changing altitude and hence freestream pressure, show that the order of magnitude difference in the pressure for these two sets of results could account for the order of magnitude difference in the electron number densities. If the electron number density for case 5 is scaled linearly with pressure to match the pressure for Omura and Presley's results, a value of $1.36x10^{12}$ is obtained. It should be noted, however, that Omura and Presley's

results for air indicate that the presence of oxygen in the gas will have significant effects on the electron production in the precursor. Their results indicated that including the effects of absorption by oxygen in the precursor results in an order of magnitude increase in the electron number densities ahead of the shock wave.

CONCLUSIONS AND RECOMMENDATIONS FOR FUTURE WORK

A method has successfully been developed to calculate the chemical and thermal nonequilibrium precursor flow field as well as the subsequent effects of this region on the shock layer and radiative flux to an entry vehicle body. The precursor flow field has been calculated for a series of test cases representing flow field conditions for a vehicle entering the earth's atmosphere upon returning from Mars. For these cases, it has been shown that the precursor region has negligible effect on the shock layer and radiative flux to the body. However, for an entry trajectory with a higher velocity or lower altitude than those considered in this study, the precursor could prove to be of significance. In any event, the effect of the hot radiating shock layer on the precursor is significant and leads to electron temperatures on the order of 6000°K and electron number densities as high as 7×10^{12} particles per cubic cm.

It is suggested that research be continued in order to further improve the model used to calculate the precursor conditions in this study. Research by other authors has shown that the absorption of radiation by oxygen in the precursor can be significant and it is recommended that oxygen be added to this model in the future. The radiative processes of oxygen which are expected to have the greatest influence in the precursor are dissociation through the continuum associated with the Schumann-Runge band and molecular ionization. In addition, collisional chemistry involving election impact reactions may be important in the region immediately in front of the shock layer as also may be line radiation absorption. These phenomena should also be included in future studies.

REFERENCES

1. Smith, G.L., "Radiation-Induced Precursor Flow Field Ahead of a Reentering Body", PhD Thesis, Virginia Polytechnic Institute, Blacksburg, VA, March 1968.

2. Williams, S.D., Pavlosky, J.E., and Curry, D.M., "A Preliminary TPS Design for MRSR-Aerobraking at Mars and at Earth", AIAA Paper 90-0052, Jan. 1990.

3. Lasher, L.E., and Wilson, K.H., "Effects of Shock Precursor Heating on Radiative Flux to Blunt Bodies", Lockheed Missiles and Space Co., Palo Alto, CA, NASA-CR-1265, 1969.

4. Tiwari, S.N., and Szema, K.Y., "Effects of Precursor Heating on Chemical and Radiative Nonequilibrium Viscous Flow Around a Jovian Entry Body", AIAA Paper 78-907, May 1978.

5. Wetzel, L., "Far-Flow Approximations for Precursor Ionization Profiles", *AIAA Journal*, Vol. 2, No. 7, July 1964, pp. 1208-1214.

6. Lederman, S., and Wilson, D.S., "Microwave Resonant Cavity Measurements of Shock Produced Electron Precursors", *AIAA Journal*, Vol. 5, No. 1, Jan. 1967, pp. 71-77.

7. Shreffler, R.G., and Christian, R.H., "Boundary Disturbances in High Explosive Shock Tube", *J. Appl. Phys.*, Vol. 25, No. 3, March 1954, pp. 324-331.

8. Voorhies, H.G., and Scott, F.R., "Optical Measurements in a Helium Shock Tube", *Bull. Amer. Phys. Soc.*, Vol. 4, June 1959, p. 40.

9. Weymann, H.D., "Electron Diffusion Ahead of Shock Waves in Argon", *Phys. of Fluids*, Vol. 3, No. 4, July 1960, pp. 545-548.

10. Weymann, H.D., and Troy, B., "Electron and Ion Density Profiles Ahead of Shock Waves in Argon", *Bull. Amer. Phys. Soc.*, Vol. 6, Feb. 1961, p. 212.

11. Zivanovic, S., "Investigation of Precursor Ionization in Front of Shock Waves of Hypersonic Projectiles", GM Defense Res. Labs, San Diego, CA, TR 63-217E, May 1963.

12. Omura, M., and Presley, L.L., "Electron Density Measurements Ahead of Shock Waves in Air", *AIAA Journal*, Vol. 7, No. 12, Dec. 1969, pp. 2363-2365.

13. Omura, M., and Presley, L.L., "Further Studies of Precursor Electron Densities Ahead of Shock Waves", *Proceedings of the 4th Plasma Sheath Symposium*, NASA-SP-252, Oct. 1970, pp. 335-358.

14. Murty, S.S.R., "Effects of Line Radiation on Precursor Ionization", *J. Quant. Spect. Rad. Trans.*, Vol. 8, Sept. 1968, pp. 531-554.

15. Nelson, H.F., and Goulard, R., "Structure of Shock Waves with Nonequilibrium Radiation and Ionization", *Phys. of Fluids*, Vol. 12, No. 8, Aug. 1969, pp. 1605-1617.

16. Nelson, H.F., "Nonequilibrium Structure of Argon Shock Waves", *Phys. of Fluids*, Vol. 16, No. 12, Dec. 1973, pp. 2132-2142.

17. Clarke, J.H., and Ferrari, C., "Gas Dynamics with Nonequilibrium Radiative and Collisional Ionization", *Phys. of Fluids*, Vol. 8, No. 12, Dec. 1965, pp. 2121-2139.

18. Pirri, A.N., and Clarke, J.H., "Radiative Ionization Patterns in Cold Precursor of Axisymmetric Detached Shock", *AIAA Journal*, Vol. 8, No. 9, Sept. 1970, pp. 1574-1581.

19. Foley, W.H., and Clarke, J.H., "Shock Waves Structured by Nonequilibrium Ionizing and Thermal Phenomena", *Phys. of Fluids*, Vol. 16, No. 3, March 1973, pp. 375-383.

20. Tiwari, S.N., and Szema, K.Y., "Radiation Induced Precursor Flow Field Ahead of a Jovian Entry Body", AIAA Paper 77-768, June 1977.

21. Tiwari, S.N., and Szema, K.Y., "Influence of Precursor Heating on Viscous Flow Around a Jovian Entry Body", AIAA Paper 78-190, Jan. 1978.

22. Thompson, R.A., "Comparison of Nonequilibrium Viscous Shock Layer Solutions with Windward Surface Shuttle Heating Data", AIAA Paper 87-1473, June 1987.

23. Carlson, L.A., "Nonequilibrium Radiation and Chemistry Models for Aerocapture Vehicle Flowfields", Texas A&M University, College Station, TX, TAMRF Rep. No. 6382-90-02, June 1990.

24. Nicolet, W.E., "Advanced Methods for Calculating Radiation Transport in Ablation Product Contaminated Boundary Layers", Aerotherm Corp., Mountain View, CA, NASA-CR-1656, Sept. 1970.

25. Dobbins, R.A., "Photoexcitation and Photoionization of Argon Ahead of a Strong Shock Wave", AIAA Paper 68-666, June 1968.

26. Herzberg, G., *Molecular Spectra and Molecular Structure, I. Spectra of Diatomic Molecules*, 2nd ed., Krieger, Malabar, FL, 1989.

27. Zel'dovich, Y.B., and Raizer, Y.P., *Physics of Shock Waves and High-Temperature Hydrodynamic Phenomena*, Vol. 2, Academic Press, New York, NY, 1967.

28. Watanabe, K., "Ultraviolet Absorption Processes in the Upper Atmosphere", *Advances in Geophys.*, Vol. 5, 1958, pp. 153-221.

29. Marr, G.V., *Photoionization Processes in Gases*, Academic Press, New York, NY, 1967.

30. Horton, T.E., "Radiative Coupled Nonequilibrium Flow Fields Associated with Aeroassisted Orbital Transfer", University of Mississippi, University, MS, NASA Contractor Rept. NAG-1-496, March 1986.

31. Gnoffo, P.A., Gupta, R.N., and Shinn, J.L., "Conservation Equations and Physical Models for Hypersonic Air Flows in Thermal and Chemical Nonequilibrium", NASA Langley Research Center, Hampton, VA, NASA-TP-2867, Feb. 1989.

32. Biberman, L.M., and Veklenko, B.A., "Radiative Processes Ahead of a Shock Wave Front", *Sov. Phys JETP*, Vol. 37, No. 10, Jan. 1960, pp. 117-120.

33. Ferrari, C., and Clarke, J.H., "On Photoionization Ahead of a Strong Shock Wave", *Supersonic Flow, Chemical Processes and Radiative Transfer*, Pergamon Press, New York, NY, 1964.

34. Tiwari, S.N., and Szema, K.Y., "Effects of Precursor Heating on Radiative and Chemically Reacting Viscous Flow Around a Jovian Entry Body", Old Dominion Univ. Research Foundation, Norfolk, VA, NASA-CR-3186, Nov. 1979.

35. Lofthus, A., "The Molecular Spectrum of Nitrogen: A Review of Investigations and a Compilation of Important Data on the Spectrum and Electronic States of Nitrogen", University of Oslo, Blindern, Norway, Dec. 1960.

36. Zel'dovich, Y.B., and Raizer, Y.P., *Physics of Shock Waves and High-Temperature Hydrodynamic Phenomena*, Vol. 1, Academic Press, New York, NY, 1966.

37. Allen, R.A., "Air Radiation Graphs: Spectrally Integrated Fluxes Including Line Contributions and Self Absorption", Avco Corporation, Everett, MA, NASA-CR-556, 1965.

38. Carlson, L.A., and Gally, T.A., "The Effect of Electron Temperature and Impact Ionization on Martian Return AOTV Flowfields", AIAA Paper 89-1729, June 1989.

39. Carlson, L.A., "Radiative Transfer, Chemical Nonequilibrium, and Two-Temperature Effects Behind a Reflected Shock Wave in Nitrogen", PhD Thesis, Ohio State University, Columbus, OH, 1969.

40. Lee, J.H., "Basic Governing Equations for the Flight Regimes of Aeroassisted Orbital Transfer Vehicles", AIAA Paper 84-1729, June 1984.

41. Vincenti, W.G., and Kruger, C.H., *Introduction to Physical Gas Dynamics*, Krieger, Malabar, FL, 1965.

APPENDIX A

DERIVATION OF THE ELECTRON/ELECTRONIC ENERGY EQUATION WITH RADIATIVE EFFECTS

For this derivation, the following notational scheme is used. The term, q, is the radiative flux vector. The negative of the change in this term, $-\partial q/\partial x$, is the total change in the energy of the gas per unit of time due to the absorption and emission of radiation. This change can be split into components, one for each individual energy mode of the gas, such that

$$-\frac{\partial q}{\partial x} = -\left(\frac{\partial q}{\partial x}\right)_{ke_{e^-}} -\left(\frac{\partial q}{\partial x}\right)_{tr} -\left(\frac{\partial q}{\partial x}\right)_{elct} -\left(\frac{\partial q}{\partial x}\right)_{vib} -\left(\frac{\partial q}{\partial x}\right)_{rot} -\left(\frac{\partial q}{\partial x}\right)_{e^\circ} \quad \text{(A-1)}$$

The terms on the right hand side of this equation represent the six possible modes of energy storage of the gas; free-electron kinetic, heavy particle translational, electronic, vibrational, rotational and the energy associated with the zero points of all species.

However, at times it is also convenient to consider the change in the radiative flux due to each photoprocess. Therefore, the total change in the radiative flux is also considered by dividing into the changes due to each individual photoprocess,

$$-\frac{\partial q}{\partial x} = -\left(\frac{\partial q}{\partial x}\right)^{FF} -\left(\frac{\partial q}{\partial x}\right)^{BF_{ion}} -\left(\frac{\partial q}{\partial x}\right)^{BF_{diss}} -\left(\frac{\partial q}{\partial x}\right)^{BB_{A\text{-}lines}} -\left(\frac{\partial q}{\partial x}\right)^{BB_{M\text{-}band}} \quad \text{(A-2)}$$

The five terms on the right hand side of this equation are the changes in the radiative flux due to absorption or emission through the free-free processes, bound-free ionization, bound-free dissociation, bound-bound atomic lines and bound-bound molecular bands respectively. As shown, the sum of the changes due to each individual process is the

total change in the radiative flux. Equations (A-1) and (A-2) represent two methods of dividing the radiative energy absorbed or emitted by the gas.

Utilizing the free electron energy equation derived by Carlson[39] and neglecting the diffusion, heat transfer and viscous terms since they are not being considered in this study, the electron energy equation including the effects of the absorption of radiation can be written as

$$\frac{D}{Dt}(\rho_{e^-} e_{e^-}) + \rho_{e^-} e_{e^-}\left(\frac{\partial}{\partial \bar{x}}\cdot \bar{V}\right) + \frac{\partial}{\partial \bar{x}}\cdot(\bar{V} p_{e^-}) - \bar{V}\cdot\frac{\partial}{\partial \bar{x}}(p_{e^-}) = \sum_{n=1}^{n_s} \xi_{e,n} + Q_e + \dot{w}_{e^-} \frac{V^2}{2} - \left(\frac{\partial}{\partial \bar{x}}\cdot \bar{q}\right)_{ke_{e^-}} + B_{e,elct} \tag{A-3}$$

The first term on the right in this equation is the increase in electron energy due to elastic collisions and the second term accounts for energy transfer due to inelastic collisions. The last two terms on the right hand side have been added to Carlson's equation to account for the change in electron kinetic energy due to the absorption or emission of radiation and the transfer of energy between the free electrons and the electronic states, respectively. It should be noted that unlike Lee[40] the radiation term included above is not the total change in the radiative flux; as discussed in the "Radiative Processes" section of the text, the absorption and emission of radiation affects not only the free electron energy but all of the energy modes. Likewise, Lee does not include a term allowing energy transfer between the electrons and the electronic states. However, if it is assumed that the free electrons and electronic states are not in equilibrium with each other then a mechanism should be included by which energy can be transfered between them.

By expanding the total derivative on the left hand side and combining terms, the free electron energy equation becomes

$$\frac{\partial}{\partial t}(\rho_e e_e) + \frac{\partial}{\partial \bar{x}} \cdot (\rho_e e_e \bar{V}) + p_e \frac{\partial}{\partial \bar{x}} \cdot \bar{V} = \sum_{n=1}^{n_s} \xi_{e,n} + Q_e + \dot{w}_e \frac{V^2}{2} - \left(\frac{\partial}{\partial \bar{x}} \cdot \bar{q} \right)_{ke_{e^-}} + B_{e,elct} \tag{A-4}$$

or

$$\frac{\partial}{\partial t}(\rho_e e_e) + \frac{\partial}{\partial \bar{x}} \cdot (\rho_e e_e \bar{V}) = - p_e \frac{\partial}{\partial \bar{x}} \cdot \bar{V} + \sum_{n=1}^{n_s} \xi_{e,n} + Q_e + \dot{w}_e \frac{V^2}{2} - \left(\frac{\partial}{\partial \bar{x}} \cdot \bar{q} \right)_{ke_{e^-}} + B_{e,elct} \tag{A-5}$$

This equation is in the form of a conservation of free electron energy per unit volume.

The equivalent equation for the electronic energy can be written as

$$\frac{\partial}{\partial t}\left(\sum_{n=1}^{n_s} \rho_n e_{elct_n} \right) + \frac{\partial}{\partial \bar{x}} \cdot \left(\sum_{n=1}^{n_s} \rho_n e_{elct_n} \bar{V} \right) = - \left(\frac{\partial}{\partial \bar{x}} \cdot \bar{q} \right)_{elct} - B_{e,elct} \tag{A-6}$$

Now, for the precursor region it is assumed that the free electrons and the electronic energy modes are in equilibrium with each other and thus governed by the same temperature; therefore, it is appropriate to use a combination electron/electronic energy equation. This approach is also advantageous since it eliminates the energy transfer

terms between the electrons and the electronic states which are neither well understood nor well defined. Combining equations (A-5) and (A-6) leads to

$$\frac{\partial}{\partial t}(\rho_{e^-} e_{e^-} + \sum_{n=1}^{n_s} \rho_n e_{elct_n}) + \frac{\partial}{\partial \bar{x}} \cdot (\rho_{e^-} e_{e^-} \bar{V} + \bar{V} \sum_{n=1}^{n_s} \rho_n e_{elct_n}) = p_{e^-} \frac{\partial}{\partial \bar{x}} \cdot \bar{V}$$
$$+ \sum_{n=1}^{n_s} \xi_{e,n} + Q_e + \dot{w}_{e^-} \frac{V^2}{2} - \left(\frac{\partial}{\partial \bar{x}} \cdot \bar{q}\right)_{ke_{e^-}} - \left(\frac{\partial}{\partial \bar{x}} \cdot \bar{q}\right)_{elct} \qquad \text{(A-7)}$$

Now, if a combined electron/electronic energy is defined as

$$e_e' = \frac{\rho_{e^-}}{\rho} e_{e^-} + \sum_{n=1}^{n_s} \frac{\rho_n}{\rho} e_{elct_n} \qquad \text{(A-8)}$$

then this equation becomes

$$\frac{\partial}{\partial t}(\rho\, e_e') + \frac{\partial}{\partial \bar{x}} \cdot (\rho \bar{V} e_e') = -p_{e^-} \frac{\partial}{\partial \bar{x}} \cdot \bar{V} + \sum_{n=1}^{n_s} \xi_{e,n} + Q_e + \dot{w}_{e^-} \frac{V^2}{2}$$
$$- \left(\frac{\partial}{\partial \bar{x}} \cdot \bar{q}\right)_{ke_{e^-}} - \left(\frac{\partial}{\partial \bar{x}} \cdot \bar{q}\right)_{elct} \qquad \text{(A-9)}$$

In the interest of computational efficiency, it is desirable to use the total change in the radiative flux rather than the individual components such as those in equation (A-9) since the evaluation of the two radiative terms in this equation will require a large number of frequency integrations. This effort can be decreased by using the total change in the radiative flux and subtracting off the portion which does not affect this equation.

Since a portion of the radiative energy absorbed affects the energy stored in the zero points of the gas, adding these to the energy equation above is a step towards using

the entire change in the radiative flux. Multiplying the equation for the conservation of mass of each species by the zero point of the species and summing over all species yields

$$\frac{\partial}{\partial t}\left(\sum_{n=1}^{n_s} \rho_n e_n^o\right) + \frac{\partial}{\partial \bar{x}}\cdot\left(\bar{V}\sum_{n=1}^{n_s} \rho_n e_n^o\right) = \sum_{n=1}^{n_s} \dot{w}_n e_n^o \qquad \text{(A-10)}$$

Adding this expression to equation (A-9) above and defining a new energy

$$e_n'' = \frac{\rho_e}{\rho} e_e + \sum_{n=1}^{n_s} \frac{\rho_n}{\rho}(e_{elct_n} + e_n^o) \qquad \text{(A-11)}$$

leads to the following equation for the electron/electronic energy

$$\begin{aligned}\frac{\partial}{\partial t}(\rho e_n'') + \frac{\partial}{\partial \bar{x}}(\bar{V}\rho e_n'') &= -p_e \frac{\partial}{\partial \bar{x}}\cdot\bar{V} + \sum_{n=1}^{n_s} \xi_{e,n} + Q_e \\ &+ \dot{w}_e \frac{V^2}{2} + \sum_{n=1}^{n_s} \dot{w}_n e_n^o - \left(\frac{\partial}{\partial \bar{x}}\cdot\bar{q}\right)_{ke_e^-} - \left(\frac{\partial}{\partial \bar{x}}\cdot\bar{q}\right)_{elct}\end{aligned} \qquad \text{(A-12)}$$

By separating the mass production rates in this equation into those due to collisional reactions and those due to radiative reactions such that

$$\dot{w}_n = \dot{w}_n^{coll} + \dot{w}_n^{rad} \qquad \text{(A-13)}$$

and then incorporating equation (A-1) for the radiative terms, equation (A-12) becomes

$$\begin{aligned}\frac{\partial}{\partial t}(\rho e_e'') + \frac{\partial}{\partial \bar{x}}\cdot(\bar{V}\rho e_e'') &= -p_e \frac{\partial}{\partial \bar{x}}\cdot\bar{V} + \sum_{n=1}^{n_s} \xi_{e,n} + Q_e \\ &+ \dot{w}_e \frac{V^2}{2} + \sum_{n=1}^{n_s} \dot{w}_n^{coll} e_n^o - \frac{\partial}{\partial \bar{x}}\cdot\bar{q} + \left(\frac{\partial}{\partial \bar{x}}\cdot\bar{q}\right)_{vib} \\ &+ \left(\frac{\partial}{\partial \bar{x}}\cdot\bar{q}\right)_{tr} + \left(\frac{\partial}{\partial \bar{x}}\cdot\bar{q}\right)_{rot} + \left(\frac{\partial}{\partial \bar{x}}\cdot\bar{q}\right)_{e^o} + \sum_{n=1}^{n_s} \dot{w}_n^{rad} e_n^o\end{aligned} \qquad \text{(A-14)}$$

The remainder of this appendix involves simplifying equation (A-14) and deriving expressions for the last four terms on the right hand side of this equation. Before

proceeding with this derivation, a review is recommended of the section in the text, "Radiative Processes", which discusses the effects of each radiative process on the individual energy modes of the gas. A brief summery of the energy modes influenced by each radiative process is given by

Radiative Process	Energy Modes Affected
Free-Free, Bremsstrahlung	- Free Electron
Bound-Free	
Ionization	- Free Electron
	- Electronic
	- Zero Points
Dissociation	- Translational
	- Electronic
	- Vibrational
	- Rotational
	- Zero Points
Bound-Bound	
Atomic Lines	- Electronic
Molecular Bands	- Electronic
	- Vibrational
	- Rotational

Defining $Y_{\nu}^{p} = k_{\nu}^{p}/k_{\nu,tot}$ for each individual radiative process rather than only for those causing chemical reactions, as in Appendix B, it is possible to find the change in the radiative flux due to each process

$$\left(\frac{\partial q}{\partial x}\right)^{p} = \int_{0}^{\infty} Y_{\nu}^{p} \frac{\partial q_{\nu}}{\partial x} d\nu \qquad \text{(A-15)}$$

Likewise, since the energy of a photon is $h\nu$, the rate of photon absorption per unit volume per unit time for each process can be written as

$$\left(\frac{rate\ of\ photons\ absorbed}{volume}\right)^{p} = \int_{0}^{\infty} \frac{Y_{\nu}^{p}}{h\nu} \frac{\partial q_{\nu}}{\partial x} d\nu \qquad \text{(A-16)}$$

These equations result from a derivation following the same steps demonstrated in Appendix B for the mass production rates. Equation (A-16) will play a vital part in the development of the radiative terms in the electron/electronic energy equation.

At this point, it is necessary to consider each radiative process and quantify its effects on each of the energy modes. First, the free-free process will be considered. As discussed previously, this process affects only the kinetic energy of the free electrons. By equation (A-15), we have

$$\left(\frac{\partial q}{\partial x}\right)_{ke_e^-}^{FF} = \int_0^\infty Y^{FF} \frac{\partial q_\nu}{\partial x} d\nu \qquad \text{(A-17)}$$

Since the atomic lines involve only transitions between electronic states in an atom, the radiation emitted or absorbed through this process affects only the electronic energy. As with the free-free processes above, the effect can be determined with the use of equation (A-15),

$$\left(\frac{\partial q}{\partial x}\right)_{elct}^{BB_{A\text{-}lines}} = \int_0^\infty Y^{BB_{A\text{-}lines}} \frac{\partial q_\nu}{\partial x} d\nu \qquad \text{(A-18)}$$

In this equation, the variable, $Y^{BB\ A\text{-}lines}$, must include the absorption coefficients for all of the atomic lines. Equation (A-15) was used to determine the effects on the energy of absorption or emission through the free-free and atomic line processes. Since each of these processes affects only one energy mode, equation (A-15) can be used to determine the amount of energy added to or taken away from the one energy mode involved. However, for the remaining processes it is necessary to find the effects of the absorption or emission of an individual photon on each energy mode and then use equation (A-16)

to account for all of the photons involved. This is necessary since the energy absorbed or emitted through the remaining processes is distributed through several energy modes.

The absorption and emission of radiation through molecular bands involves not only the electronic states, but also the vibrational and rotational states. As mentioned in the text, the change in the electronic energy due to the absorption or emission of a photon through a molecular band is easily found from knowledge of the two electronic states associated with the band and is

$$\Delta E_{elct_i} = E^{upp}_{elct_i} - E^{low}_{elct_i} \tag{A-19}$$

where $E^{upp}{}_{elct\ i}$ and $E^{low}{}_{elct\ i}$ are the energies relative to the ground state of the molecule for the upper and lower electronic states associated with the ith molecular band. From this expression and equation (A-16), the total change in the electronic energy due to molecular bands is

$$\left(\frac{\partial q}{\partial x}\right)^{BB_{M\text{-}band}}_{elct} = \sum_{i=1}^{n_{M\text{-}band}} \int_0^{\infty} \frac{Y^{BB_{M\text{-}band}}_{\nu_i} (E^{upp}_{elct_i} - E^{low}_{elct_i})}{h\nu} \frac{\partial q_\nu}{\partial x} d\nu \tag{A-20}$$

The integration in this equation accoints for all photons absorbed or emitted in each molecular band and the summation is over all molecular bands in order to account for the effects of every band.

The effect of absorption through the molecular bands on the vibrational and rotational energy of the gas is not easily calculated without exact knowledge of the upper and lower energy levels of the molecule associated with the absorption of the photon; however, these upper and lower states vary with the frequency of the absorbed photon

and are not easily found. The sum of the effect on these two energy modes can however be found easily. The change in these two energy modes is given by equation (20) as

$$\Delta E_{vib_i} + \Delta E_{rot_i} = h\nu - \Delta E_{elct_i} \tag{A-21}$$

As above the influence of all the molecular bands can be found with the use of equation (A-16) and by summing over the molecular bands,

$$\left(\frac{\partial q}{\partial x}\right)_{vib}^{BB_{M\text{-}band}} + \left(\frac{\partial q}{\partial x}\right)_{rot}^{BB_{M\text{-}band}} = \sum_{i=1}^{n_{M\text{-}bands}} \int_0^\infty \frac{Y_{\nu_i}^{BB_{M\text{-}band}}(h\nu - E_{elct_i}^{upp} + E_{elct_i}^{low})}{h\nu} \left(\frac{\partial q_\nu}{\partial x}\right) d\nu \tag{A-22}$$

The effects of the bound-free absorption processes on the zero point energy of the gas can be considered as a whole rather than splitting it into contributions due to ionization and dissociation. This is appropriate since the chemical reactions related to the bound-free photoprocess can all be represented by the reaction

$$\sum_{n=1}^{n_s} a_{i,n} x_n + h\nu \rightleftharpoons^{k'_{\nu_i}} \sum_{n=1}^{n_s} a'_{i,n} x_n \tag{A-23}$$

The energy necessary for this reaction to occur is the difference between the zero point energies of the products and the reactants. For the ionization reaction this difference is equivalent to the ionization energy, I, and for the dissociation reaction, it is the dissociation energy, D. For each photon absorbed through the ith process this reaction energy is given by

$$I_i, D_i = \sum_{n=1}^{n_s} (a'_{i,n} - a_{i,n}) m_n e_n^o \tag{A-24}$$

Using equation (A-16), the increase in the energy associated with the zero points of the gas due to absorption by the ith bound-free process is given by

$$\Delta e_i^o = \int_0^\infty \frac{Y_{\nu_i}^p}{h\nu} \frac{\partial q_\nu}{\partial x} \sum_{n=1}^{n_s} (a'_{i,n} - a_{i,n}) m_n e_n^o \, d\nu \tag{A-25}$$

Summing over all of the bound-free processes results in the change in the zero point energy of the gas due to all of the radiative bound-free processes, i.e.

$$\left(\frac{\partial q}{\partial x}\right)_{e^o}^{BF_{ion}} + \left(\frac{\partial q}{\partial x}\right)_{e^o}^{BF_{diss}} = \sum_{i=1}^{n_{BF}} \sum_{n=1}^{n_s} e_n^o m_n \int_0^\infty \frac{Y_{\nu_i}^p}{h\nu} (a'_{i,n} - a_{i,n}) \frac{\partial q_\nu}{\partial x} \, d\nu \tag{A-26}$$

or

$$\left(\frac{\partial q}{\partial x}\right)_{e^o}^{BF_{ion}} + \left(\frac{\partial q}{\partial x}\right)_{e^o}^{BF_{diss}} = \sum_{n=1}^{n_s} e_n^o m_n \int_0^\infty \frac{\sum_{i=1}^{n_{BF}} Y_{\nu_i}^p (a'_{i,n} - a_{i,n})}{h\nu} \frac{\partial q_\nu}{\partial x} \, d\nu \tag{A-27}$$

Now, substituting equation (B-17) for the mass production of each species due to photoreactions into equation (A-27), it is apparent that

$$\left(\frac{\partial q}{\partial x}\right)_{e^o}^{BF_{ion}} + \left(\frac{\partial q}{\partial x}\right)_{e^o}^{BF_{diss}} = \sum_{n=1}^{n_s} \dot{w}_n^{rad} e_n^o \tag{A-28}$$

The effects of the bound-free processes on the remaining energy modes will be found by first considering the ionization process and then the dissociation process. As discussed in the photoprocesses section of the text, the ionization process affects the electronic, free electron and zero point energies of the gas. For each photon absorbed, the electronic energy of the gas decreases by the electronic energy, E_{elct}, of the particle absorbing the photon since the ion formed in the process is in the ground state and thus

has no electronic energy. Using equation (A-16) and summing over the photoionization processes, the change in the electronic energy due to these reactions is

$$\left(\frac{\partial q}{\partial x}\right)_{elct}^{BF_{ion}} = \sum_{i=1}^{n_{BF_{ion}}} \int_0^\infty \frac{Y_{\nu_i}^{P}(-E_{elct_i})}{h\nu} \frac{\partial q_\nu}{\partial x} d\nu \qquad \text{(A-29)}$$

Due to the photoionization process, the energy of the free electrons increases by the kinetic energy of the electron created. This increase in the electron kinetic energy due to the absorption of a photon in the ith ionization continuum is given by equation (21) as

$$ke_{e_i^-} = h\nu + E_{elct_i} - I_i \qquad \text{(A-30)}$$

Once again, the use of equation (A-16) along with a summation over the ionization processes leads to

$$\left(\frac{\partial q}{\partial x}\right)_{ke_{e^-}}^{BF_{ion}} = \sum_{i=1}^{n_{BF_{ion}}} \int_0^\infty \frac{Y_{\nu_i}^{P}\,(h\nu + E_{elct_i} - I)}{h\nu} \frac{\partial q_\nu}{\partial x} d\nu \qquad \text{(A-31)}$$

The final process to be considered is that of photodissociation. This radiative process affects the electronic, vibrational, rotational, translational and zero point energies of the gas. As discussed previously, the change in the electronic energy of the gas can be determined from knowledge of the molecular band through which the dissociation occurs; this change in the electronic energy due to a photon absorbed in the ith dissociation process is given by equation (23) as

$$\Delta E_{elct_i} = E_{elct_i}^{atm\,1} + E_{elct_i}^{atm\,2} - E_{elct_i}^{molc} \qquad \text{(A-32)}$$

In this equation, the energy of the electronic state for each particle is considered relative to the ground state of the particle. Using this equation along with equation (A-16) and summing over the dissociation processes leads to the expression

$$\left(\frac{\partial q}{\partial x}\right)_{elct}^{BF_{diss}} = \sum_{i=1}^{n_{BF_{diss}}} \int_0^{\infty} \frac{Y_{\nu_i}^{P} \left(E_{elct_i}^{atm\,1} + E_{elct_i}^{atm\,2} - E_{elct_i}^{molc}\right)}{h\nu} \frac{\partial q_\nu}{\partial x} d\nu \qquad \text{(A-33)}$$

for the change in the electronic energy due to all of the bound-free dissociation processes.

In a photodissociation process, the vibrational and rotational energy modes of the gas lose energy equal to the vibrational energy, $E^{molc}{}_{vib}$, and cthe rotational energy, $E^{molc}{}_{rot}$, of the molecule dissociated. It follows that the sum of the change in the vibrational and rotational energies of the gas due to the photodissociation process is given by

$$\left(\frac{\partial q}{\partial x}\right)_{vib}^{BF_{diss}} + \left(\frac{\partial q}{\partial x}\right)_{rot}^{BF_{diss}} = \sum_{i=1}^{n_{BF_{diss}}} \int_0^{\infty} \frac{Y_{\nu_i}^{P} \left(- E_{vib}^{molc} - E_{rot}^{molc}\right)}{h\nu} \frac{\partial q_\nu}{\partial x} d\nu \qquad \text{(A-34)}$$

As above, this equation results from utilizing equation (A-16) to account for all photons absorbed or emitted in each dissociation process and a summation to account for all dissociation processes.

Lastly, the translational energy of the heavy particles is increased by the kinetic energy of the two atoms created in the dissociation process. From equations (22) and (23), the increase in the translational energy due to the absorption of a photon in the ith dissociation continuum is given by

$$ke_{atm_i} = -\Delta E_{elct_i} + E_{vib_i}^{molc} + E_{rot_i}^{molc} + h\nu - D_i \qquad \text{(A-35)}$$

From this expression and equation (A-16), the total change in the heavy particle translational energy due to the photodissociation processes is

$$\left(\frac{\partial q}{\partial x}\right)_{tr}^{BF_{diss}} = \sum_{i=1}^{n_{BF_{diss}}} \int_0^\infty \frac{Y_{\nu_i}^{p}\,(-\Delta E_{elct_i} + E_{vib_i}^{molc} + E_{rot_i}^{molc} + h\nu - D_i)}{h\nu} \frac{\partial q_\nu}{\partial x}\, d\nu \qquad \text{(A-36)}$$

The total change in the energy in each energy mode due to photoprocesses is given by adding the contributions from each type of photoprocess. This approach leads to the following expressions:

Free Electron Kinetic Energy--

$$\left(\frac{\partial q}{\partial x}\right)_{ke_{e^-}} = \int_0^\infty Y_\nu^{FF} \frac{\partial q_\nu}{\partial x}\, d\nu + \sum_{i=1}^{n_{BF_{ion}}} \int_0^\infty \frac{Y_{\nu_i}^{p}\,(h\nu + E_{elct_i} - I_i)}{h\nu} \frac{\partial q_\nu}{\partial x}\, d\nu \qquad \text{(A-37)}$$

Heavy Particle Translational--

$$\left(\frac{\partial q}{\partial x}\right)_{tr} = \sum_{i=1}^{n_{BF_{diss}}} \int_0^\infty \frac{Y_{\nu_i}^{p}\,(-\Delta E_{elct_i} + E_{vib_i}^{molc} + E_{rot_i}^{molc} + h\nu - D_i)}{h\nu} \frac{\partial q_\nu}{\partial x}\, d\nu \qquad \text{(A-38)}$$

Electronic--

$$\left(\frac{\partial q}{\partial x}\right)_{elct} = \int_0^\infty Y_\nu^{BB_{A\text{-}lines}} \frac{\partial q_\nu}{\partial x}\, d\nu + \sum_{i=1}^{n_{M\text{-}band}} \int_0^\infty \frac{Y_{\nu_i}^{p}(E_{elct_i}^{upp} - E_{elct_i}^{low})}{h\nu} \frac{\partial q_\nu}{\partial x}\, d\nu$$

$$+ \sum_{i=1}^{n_{BF_{ion}}} \int_0^\infty \frac{Y_{\nu_i}^{p}\,(-E_{elct_i})}{h\nu} \frac{\partial q_\nu}{\partial x}\, d\nu \qquad \text{(A-39)}$$

$$+ \sum_{i=1}^{n_{BF_{diss}}} \int_0^\infty \frac{Y_{\nu_i}^{p}\,(E_{elct_i}^{atm1} + E_{elct_i}^{atm2} - E_{elct_i}^{molc})}{h\nu} \frac{\partial q_\nu}{\partial x}\, d\nu$$

Vibrational and Rotational--

$$\left(\frac{\partial q}{\partial x}\right)_{vib} + \left(\frac{\partial q}{\partial x}\right)_{rot} = \sum_{i=1}^{n_{M\text{-}band}} \int_0^{\infty} \frac{Y_{\nu_i}^{p}\,(h\nu - E_{elct_i}^{upp} + E_{elct_i}^{low})}{h\nu} \frac{\partial q_\nu}{\partial x}\, d\nu + \sum_{i=1}^{n_{BF_{diss}}} \int_0^{\infty} \frac{Y_{\nu_i}^{p}\,(-E_{vib_i}^{molc} - E_{rot_i}^{molc})}{h\nu} \frac{\partial q_\nu}{\partial x}\, d\nu \tag{A-40}$$

Zero Point--

$$\left(\frac{\partial q}{\partial x}\right)_{e^o} = -\sum_{i=1}^{n_s} \dot{w}_n^{rad} e_n^o \tag{A-41}$$

Substituting each of the appropriate terms into the electron energy equation (A-14) and simplifying leads to

$$\frac{\partial}{\partial t}(\rho e_e'') + \frac{\partial}{\partial \bar{x}}\cdot(\bar{V}\rho e_e'') = -p_{e^-}\frac{\partial}{\partial \bar{x}}\cdot\bar{V} + \sum_{n=1}^{n_s}\xi_{e,n} + Q_e + \dot{w}_{e^-}\frac{V^2}{2} + \sum_{n=1}^{n_s}\dot{w}_n^{coll} e_n^o - \frac{\partial}{\partial \bar{x}}\cdot\bar{q} + \sum_{i=1}^{n_{BF_{diss}}} \int_0^{\infty} \frac{Y_{\nu_i}^{p}\,(h\nu - \Delta E_{elct_i} - D_i)}{h\nu}\left(\frac{\partial}{\partial \bar{x}}\cdot\bar{q}\right) d\nu + \sum_{i=1}^{n_{M_{band}}} \int_0^{\infty} \frac{Y_{\nu_i}^{p}\,(h\nu - E_{elct_i}^{upp} + E_{elct_i}^{low})}{h\nu}\left(\frac{\partial}{\partial \bar{x}}\cdot\bar{q}\right) d\nu \tag{A-42}$$

where

$$e_e'' = \frac{\rho_{e^-}}{\rho} e_{e^-} + \sum_{n=1}^{n_s} \frac{\rho_n}{\rho}(e_{elct_n} + e_n^o) \tag{A-43}$$

APPENDIX B

DERIVATION OF THE MASS PRODUCTION RATES DUE TO RADIATIVE REACTIONS

As in Vincenti and Kruger[41], the emission coefficient, j_ν, and the absorption coefficient, k_ν, are defined such that the rates of radiant energy emitted and absorbed per unit volume are given by:

$$\frac{rate\ of\ energy\ emmited}{volume} = \int_0^\infty \int_0^{4\pi} \rho j_\nu \, d\Omega \, d\nu \qquad \text{(B-1a)}$$

$$\frac{rate\ of\ energy\ absorbed}{volume} = \int_0^\infty \int_0^{4\pi} \rho k_\nu I_\nu \, d\Omega \, d\nu \qquad \text{(B-1b)}$$

Since the energy of a photon is given by $h\nu$, it follows that the rate of emission and absorption of photons per unit volume is given by:

$$\frac{rate\ of\ photons\ emitted}{volume} = \int_0^\infty \int_0^{4\pi} \frac{\rho j_\nu}{h\nu} \, d\Omega \, d\nu \qquad \text{(B-2a)}$$

$$\frac{rate\ of\ photons\ absorbed}{volume} = \int_0^\infty \int_0^{4\pi} \frac{\rho k_\nu I_\nu}{h\nu} \, d\Omega \, d\nu \qquad \text{(B-2b)}$$

A set of radiative reactions can now be considered which are represented by the general radiative reaction

$$\sum_{n=1}^{n_s} a_{n,i} X_n + h\nu \underset{j_{\nu_i}}{\overset{k_{\nu_i}}{\rightleftharpoons}} \sum_{n=1}^{n_s} a'_{n,i} X_n \tag{B-3}$$

In this reaction, $a_{n,i}$ and $a'_{n,i}$ are the stoichiometric coefficients in the ith reaction for the species given by X_n. Also, $k_{\nu i}$ and $j_{\nu i}$ are the absorption and emission coefficients for the photoprocess associated with the ith photoreaction.

Using this notation, the total emission and absorption coefficients for the gas are given by

$$\begin{aligned} k_\nu &= \sum_{i=1}^{n_{BF}} k_{\nu_i} + k_{\nu_{n_{BF+1}}} \\ j_\nu &= \sum_{i=1}^{n_{BF}} j_{\nu_i} + j_{\nu_{n_{BF+1}}} \end{aligned} \tag{B-4}$$

where $j_{\nu, n\,BF+1}$ and $k_{\nu, n\,BF+1}$ represent the emission and absorption coefficients which are associated with the emission or absorption of radiation which does not cause a chemical reaction. This emission or absorption of radiation causes a change in the energy of the gas but no change in the composition. This is the case for radiation emitted or absorbed through the free-free process, the atomic lines or the molecular bands. Note that the summation in equation (B-4) is over the bound-free processes.

If the assumption is made that every photon absorbed by a given photoprocess causes the associated photoreaction to occur, then, using equations (B-2) and (B-3), the mass production of each species by the ith reaction is given by

$$\dot{w}_{n_i} = (a'_{n,i} - a_{n,i})\, m_n \int_0^\infty \int_0^{4\pi} \frac{\rho_{abs}}{h\nu}(k_{\nu_i} I_\nu - j_{\nu_i})\, d\Omega\, d\nu \tag{B-5}$$

where m_n is the mass per particle of the species represented by X_n and ρ_{abs} is the density of the species absorbing the photon. The spectral integration in this equation is over all frequencies from zero to infinity. Looking at an individual reaction, the portion of the integral from zero to the threshold will have no effect on the mass production rate since the absorption and emission coefficients are equal to zero in this region.

Now, under the quasi-equilibrium hypothesis the change in the radiative intensity, I_ν, for each radiative reaction is given by

$$\left(\frac{\partial I_\nu}{\partial x}\right)_i = -\rho_{abs}(k_{\nu_i} I_\nu - j_{\nu_i}) = -k'_{\nu_i}(I_\nu - S_\nu) \tag{B-6}$$

where

$$k'_{\nu_i} = k_{\nu_i}(1 - e^{-h\nu/kT}) \tag{B-7}$$

Using equations (B-5) and (B-6) the mass production rate of each species due to the ith reaction is given by

$$\dot{w}_{n_i} = (a'_{n,i} - a_{n,i}) m_n \int_0^\infty \int_0^{4\pi} \frac{k'_{\nu_i}}{h\nu}(I_\nu - S_\nu)\, d\Omega\, d\nu \tag{B-8}$$

Now, if $Y^p_{\nu,i}$ is defined such that for each reaction, $Y^p_{\nu,i} = k'_{\nu,i}/k'_{\nu,tot}$, then this equation can be expressed as

$$\dot{w}_{n_i} = (a'_{n,i} - a_{n,i}) m_n \int_0^\infty \int_0^{4\pi} \frac{Y^p_{\nu_i}}{h\nu} k'_{\nu_{tot}} (I_\nu - S_\nu) d\Omega d\nu \tag{B-9}$$

The superscript "p" is used on the ratio of the absorption coefficient for the individual process to the total absorption coefficient, $Y_{\nu,i}$, to indicate that this value is for the specific bound-free process associated with the photoreaction of interest. From equation (B-6) above, the total change in the radiative intensity due to all photoprocesses is given by

$$\begin{aligned} \frac{\partial I_\nu}{\partial x} &= \sum_{i=1}^{n_{BF+1}} \left(\frac{\partial I_\nu}{\partial x} \right)_i = - \sum_{i=1}^{n_{BF+1}} k'_{\nu_i} (I_\nu - S_\nu) \\ &= -k'_{\nu_{tot}} (I_\nu - S_\nu) \end{aligned} \tag{B-10}$$

Combining equations (B-9) and (B-10), the mass production of the nth species by the ith photoreaction is given by

$$\dot{w}_{n_i} = -(a'_{n,i} - a_{n,i}) m_n \int_0^\infty \int_0^{4\pi} \frac{Y^p_{\nu_i}}{h\nu} \frac{\partial I_\nu}{\partial x} d\Omega d\nu \tag{B-11}$$

or, by rearranging the integral terms

$$\dot{w}_{n_i} = -(a'_{n,i} - a_{n,i}) m_n \int_0^\infty \frac{Y^p_{\nu_i}}{h\nu} \int_0^{4\pi} \frac{\partial I_\nu}{\partial x} d\Omega \, d\nu \tag{B-12}$$

However, in this equation the integral over 4π steradians of the change in the radiative intensity is the rate of change of the radiative energy flux,

$$\frac{\partial q_\nu}{\partial x} = \int_0^{4\pi} \frac{\partial I_\nu}{\partial x} d\Omega \tag{B-13}$$

Applying equation (B-13) to equation (B-12) gives

$$\dot{w}_{n_i} = -(a'_{n,i} - a_{n,i}) m_n \int_0^\infty \frac{Y^p_{\nu_i}}{h\nu} \frac{\partial q_\nu}{\partial x} d\nu \tag{B-14}$$

for the mass production rate due to the ith reaction. This equation gives the rate of mass production of the nth species due to the ith photoreaction. Thus, the total mass production of the nth species due to photoreactions is given by

$$\begin{aligned} \dot{w}_n &= \sum_{i=1}^{n_{BF}} \dot{w}_{n_i} \\ &= -m_n \int_0^\infty \left[\sum_{i=1}^{n_{BF}} (a'_{n,i} - a_{n,i}) Y^p_{n_i} \right] \frac{1}{h\nu} \frac{\partial q_\nu}{\partial x} d\nu \end{aligned} \tag{B-15}$$

or

$$\dot{w}_n = -m_n \int_0^\infty \frac{Y^s_{\nu_n}}{h\nu} \frac{\partial q_\nu}{\partial x} d\nu \tag{B-16}$$

where

$$Y^s_{\nu_n} = \sum_{i=1}^{n_{BF}} (a'_{n,i} - a_{n,i}) Y^p_{\nu_i} \tag{B-17}$$

In this notational scheme, $Y^p{}_{,i}$ is the fraction of the radiative energy emitted and absorbed at the frequency ν due to the photoprocess associated with the ith photoreaction;

$Y^s_{\nu,n}$, on the other hand, is the fraction of the radiative energy absorbed at the frequency ν which is associated with the production of the nth species. The distinction between these terms is that $Y^p_{\nu,i}$ is defined for a specific radiative process and $Y^s_{\nu,n}$ is defined for a specific species. Defining $Y^s_{\nu,n}$ for each species rather than for each reaction is used only as a means of simplifying the equation since there may be many reactions associated with the production or destruction of each species.

Equation (B-16) above is a general equation which allows the calculation of the mass production rate of each species due to photoreactions by knowing the change in the radiative flux due to absorption, the absorption coefficient for each individual process and the total absorption coefficient at each frequency ν. We will now apply this to the specific set of photoreactions of interest in this study. From the precursor gas model described in the text, these reactions are:

$$N_2 + h\nu \rightleftharpoons^{k_{\nu_1}'} 2N$$

$$N_2 + h\nu \rightleftharpoons^{k_{\nu_2}'} N_2^+ + e^-$$

$$N + h\nu \rightleftharpoons^{k_{\nu_3}'} N^+ + e^-$$

For this set of photoreactions, the mass production rate of each species is given by equation (B-16) above where

$$
\begin{aligned}
Y^S_{\nu_{N_2}} &= -\left(Y^P_{\nu_1} + Y^P_{\nu_2}\right) = -\frac{k'_{\nu_1} + k'_{\nu_2}}{k'_{\nu_{tot}}} \\
Y^S_{\nu_{N_2^+}} &= Y^P_{\nu_2} = \frac{k'_{\nu_2}}{k'_{\nu_{tot}}} \\
Y^S_{\nu_N} &= 2Y^P_{\nu_1} - Y^P_{\nu_3} = \frac{2k'_{\nu_1} - k'_{\nu_3}}{k'_{\nu_{tot}}} \\
Y^S_{\nu_N^+} &= Y^P_{\nu_3} = \frac{k'_{\nu_3}}{k'_{\nu_{tot}}} \\
Y^S_{\nu_e^-} &= Y^P_{\nu_2} + Y^P_{\nu_3} = \frac{k'_{\nu_2} + k'_{\nu_3}}{k'_{\nu_{tot}}}
\end{aligned}
\qquad \text{(B-18)}
$$

APPENDIX C

DERIVATION OF THE RADIATION ATTENUATION FACTORS

In this appendix the equation for the radiative flux in the precursor region is first derived using the tangent slab approximation. This approximation treats the radiation emitted at each point as if it were emitted from an infinite plane of gas perpendicular to the direction of travel of the radiation. For the purpose of this derivation only, the radiation emitted in the cold precursor region is neglected compared to that of the hot shock layer. The equation for the radiative flux in the precursor is then be derived by treating the radiation emitted in the shock layer as if it were from a finite disk of gas. These two equations are then compared and attenuation factors obtained which modify the infinite slab equation for the geometric effects associated with a finite slab.

The equation of radiative transfer in the s direction is given by

$$\frac{dI_\nu}{ds} = k_\nu'(I_\nu - S_\nu) \tag{C-1}$$

where s is measured away from the point of interest and I_ν is the radiative intensity towards the point. Placing both terms involving the radiative intensity on the left hand side and multiplying the integration factor

$$e^{-\int k_\nu' ds''} \tag{C-2}$$

through both sides results in the equation

$$\frac{dI_\nu}{ds} e^{-\int k_\nu' ds''} - k_\nu' I_\nu e^{-\int k_\nu' ds''} = -k_\nu' S_\nu e^{-\int k_\nu' ds''} \tag{C-3}$$

Combining the terms on the left hand side of equation (C-3) results in the equation

$$\frac{d}{ds}\left[I_\nu\, e^{-\int k_\nu' ds''}\right] = -k_\nu' S_\nu\, e^{-\int k_\nu' ds''} \qquad \text{(C-4)}$$

In these equations, the s'' terms are used to keep track of the various integration variables. Integrating both sides of equation (C-4) from the points s_1 to s and solving for the radiative intensity, $I_\nu(s)$, results in

$$I_\nu(s) = I_\nu(s_1)\, e^{\int_{s_1}^{s} k_\nu' ds''} - e^{\int_{s_1}^{s} k_\nu' ds''} \int_{s_1}^{s} k_\nu' S_\nu\, e^{-\int_{s_1}^{s'} k_\nu' ds''} ds' \qquad \text{(C-5)}$$

By combining the two exponential terms on the right hand side, this equation becomes

$$I_\nu(s) = I_\nu(s_1)\, e^{\int_{s_1}^{s} k_\nu' ds''} - \int_{s_1}^{s} k_\nu' S_\nu\, e^{\int_{s'}^{s} k_\nu' ds''} ds' \qquad \text{(C-6)}$$

To find the total radiative intensity at a point, the radiation due to the gas on both sides of the point is considered as shown in Figure 58. In this geometry the spatial variables s and x are related by the expression

$$dx = -\mu\, ds \qquad \text{(C-7)}$$

where

$$\mu = Cos(\theta) \qquad \text{(C-8)}$$

Applying this relation to equation (C-6) results in the following equation for the radiative intensity in terms of the spatial variable x

$$I_\nu(x) = I_\nu(x_1)\, e^{-\int_{x_1}^{x} \frac{k_\nu'}{\mu} dx''} + \int_{x_1}^{x} \frac{k_\nu' S_\nu}{\mu}\, e^{-\int_{x_1}^{x} \frac{k_\nu'}{\mu} dx''} dx' \qquad \text{(C-9)}$$

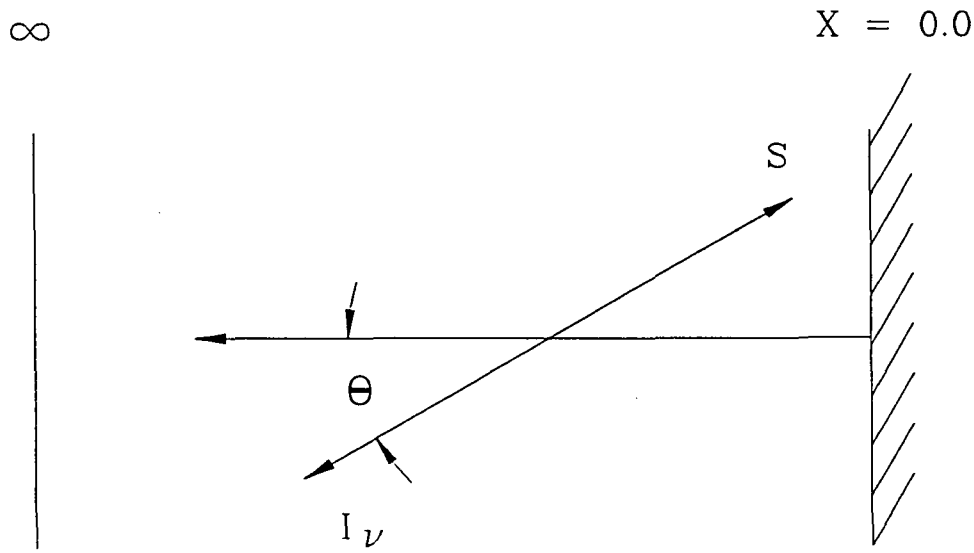

Figure 57: Geometry for the Derivation of the One-Dimensional Radiative Flux Equations

The radiative intensity at the point of interest can now be considered in two parts, that from the right, I_ν^R, and that from the left, I_ν^L. First consider the radiation from the right of the point of interest, between the point and the wall. With the geometry used in this derivation, the radiative intensity, I_ν, is in the direction from right to left and the angle θ is in the range from 0 to 90 degrees. Also, x_1 corresponds to the wall,

$$x_1 = 0$$
$$I_\nu(x_1) = I_\nu^{wall} \tag{C-10}$$

Applying equation (C-9) to this portion of the radiative intensity leads to the expression

$$I_\nu^R(x) = I_\nu^{wall} e^{-\int_0^x \frac{k_\nu'}{\mu} dx''} + \int_0^x \frac{k_\nu' S_\nu}{\mu} e^{-\int_{x'}^x \frac{k_\nu'}{\mu} dx''} dx' \tag{C-11}$$

for the radiation from the right of the point. The first term in this equation is the radiative intensity due to the wall and the second term is the radiative intensity due to gas between the point and the wall.

Now, considering the portion of the radiative intensity from the left of the point, the x_1 and $I_\nu(x_1)$ values correspond to those at infinity,

$$x_1 = \infty$$
$$I_\nu(x_1) = I_\nu^\infty \tag{C-12}$$

Applying equation (C-9) to this portion of the radiation yields

$$I_\nu^L(x) = I_\nu^\infty e^{-\int_\infty^x \frac{k_\nu'}{\mu} dx''} + \int_\infty^x \frac{k_\nu' S_\nu}{\mu} e^{-\int_{x'}^x \frac{k_\nu'}{\mu} dx''} dx' \tag{C-13}$$

for the radiative intensity from the left of the point. In this equation, the first term on the right is the radiative intensity from the boundary at infinity and the second term is that due to the gas between the point of interest and infinity.

Introducing the optical depth, τ_ν, defined such that

$$d\tau_\nu = k'_\nu dx \tag{C-14}$$

or

$$\tau_\nu = \int_0^x k'_\nu dx' \tag{C-15}$$

into the equations for the radiative intensity from the right and left results in the following expressions,

$$I_\nu^R(x) = I_\nu^{wall} e^{-\frac{\tau_\nu}{\mu}} + \int_0^{\tau_\nu} \frac{S_\nu}{\mu} e^{-\frac{(\tau_\nu - \tau'_\nu)}{\mu}} d\tau'_\nu \tag{C-16}$$

$$I_\nu^L(x) = I_\nu^\infty e^{-\frac{(\tau_\nu - \tau_\nu^\infty)}{\mu}} + \int_{\tau_\nu^\infty}^{\tau_\nu} \frac{S_\nu}{\mu} e^{-\frac{(\tau_\nu - \tau'_\nu)}{\mu}} d\tau'_\nu \tag{C-17}$$

These equations for the radiative intensity are valid for both the infinite as well as the finite slab cases. The differences between these two assumptions occur in the integration of the radiative intensity over the solid angle to find the radiative flux. In the

tangent slab approximation this relationship between the radiative flux and the radiative intensity is of the form

$$q_\nu^{TS} = \int_0^{2\pi}\int_{-1}^{1} I_\nu \mu \, d\mu d\phi \tag{C-18}$$

or

$$\begin{aligned} q_\nu^{TS} &= \int_0^{2\pi}\int_0^{1} I_\nu^R \mu \, d\mu d\phi - \int_0^{2\pi}\int_0^{-1} I_\nu^L \mu \, d\mu d\phi \\ &= q_\nu^R - q_\nu^L \end{aligned} \tag{C-19}$$

The angle ϕ in these equations is around the x-axis in the plane perpendicular to this axis. The radiative flux as defined in these equations is positive in the x-direction, or away from the wall.

In equation (C-19), by integrating over the direction cosine, μ, from 0 to -1 in the two terms, it is assumed that the radiation is emitted from an infinite slab, evident since a value of 0 for μ corresponds to a value of 90 degrees for the angle θ shown in Figure 58.

Utilizing equations (C-16), (C-17), and (C-19) and carrying out the integration with respect to ϕ from 0 to 2π, the radiative flux away from the wall for the tangent slab approximation can be written as

$$\begin{aligned} q_\nu^{TS} = {} & 2\pi \int_0^1 I_\nu^{wall} \mu e^{-\frac{\tau_\nu}{\mu}} d\mu + 2\pi \int_0^1 \int_0^{\tau_\nu} S_\nu e^{-\frac{(\tau_\nu - \tau_\nu')}{\mu}} d\tau_\nu' d\mu \\ & - 2\pi \int_0^{-1} I_\nu^{\infty} \mu e^{-\frac{(\tau_\nu - \tau_\nu^{\infty})}{\mu}} d\mu - 2\pi \int_0^{-1} \int_{\tau_\nu^{\infty}}^{\tau_\nu} S_\nu e^{-\frac{(\tau_\nu - \tau_\nu')}{\mu}} d\tau_\nu' d\mu \end{aligned} \tag{C-20}$$

By switching the order of integration on the second and fourth terms and introducing the new variable

$$\begin{aligned} \mu' &= -\mu \\ d\mu' &= -d\mu \end{aligned} \tag{C-21}$$

into the third and fourth terms, equation (C-20) can be written as

$$\begin{aligned} q_\nu^{TS} = 2\pi I_\nu^{wall} \int_0^1 \mu\, e^{-\frac{\tau_\nu}{\mu}}\, d\mu \;+\; 2\pi \int_0^{\tau_\nu} S_\nu \int_0^1 e^{-\frac{(\tau_\nu - \tau_\nu')}{\mu}}\, d\mu\, d\tau_\nu' \\ -\; 2\pi I_\nu^{\infty} \int_0^1 \mu'\, e^{-\frac{(\tau_\nu^{\infty} - \tau_\nu)}{\mu'}}\, d\mu' \;+\; 2\pi \int_{\tau_\nu^{\infty}}^{\tau_\nu} S_\nu \int_0^1 e^{-\frac{(\tau_\nu^{\infty} - \tau_\nu)}{\mu'}}\, d\mu'\, d\tau_\nu' \end{aligned} \tag{C-22}$$

In this equation the integrals with respect to μ are the 2nd and 3rd exponential integrals,

$$\begin{aligned} E_2(t) &= \int_0^1 e^{-\frac{t}{\mu}}\, d\mu \\ E_3(t) &= \int_0^1 \mu\, e^{-\frac{t}{\mu}}\, d\mu \end{aligned} \tag{C-23}$$

By introducing these expressions into equation (C-22) the equation for the radiative flux for the tangent slab approximation becomes

$$\begin{aligned} q_\nu^{TS} = 2\pi I_\nu^{wall} E_3(\tau_\nu) \;+\; 2\pi \int_0^{\tau_\nu} S_\nu E_2(\tau_\nu - \tau_\nu')\, d\tau_\nu' \\ -\; 2\pi I_\nu^{\infty} E_3(\tau_\nu^{\infty} - \tau_\nu) \;+\; 2\pi \int_{\tau_\nu^{\infty}}^{\tau_\nu} S_\nu E_2(\tau_\nu' - \tau_\nu)\, d\tau_\nu' \end{aligned} \tag{C-24}$$

This expression is the complete radiative flux equation for the tangent slab approximation. Up to this point no assumptions have been made regarding the point of

interest. However, by assuming that the point of interest is in the precursor, the integration in the second term of this equation can be divided into two parts, one over the shock layer and the second from the shock wave to the point in the precursor, resulting in the equation

$$q_\nu^{TS} = 2\pi I_\nu^{wall} E_3(\tau_\nu) + 2\pi \int_0^{\tau_\nu^s} S_\nu E_2(\tau_\nu - \tau_\nu') \, d\tau_\nu'$$

$$+ 2\pi \int_{\tau_\nu^s}^{\tau_\nu} S_\nu E_2(\tau_\nu - \tau_\nu') \, d\tau_\nu' - 2\pi I_\nu^\infty E_3(\tau_\nu^\infty - \tau_\nu) \qquad \text{(C-25)}$$

$$+ 2\pi \int_{\tau_\nu^\infty}^{\tau_\nu} S_\nu E_2(\tau_\nu' - \tau_\nu) \, d\tau_\nu'$$

If it is also assumed that the radiation emitted in the cool precursor is negligible compared to that emitted in the shock layer, then equation (C-25) will further simplify to

$$q_\nu^{TS} = 2\pi I_\nu^{wall} E_3(\tau_\nu) + 2\pi \int_0^{\tau_\nu^s} S_\nu E_2(\tau_\nu - \tau_\nu') \, d\tau_\nu' \qquad \text{(C-26)}$$

This equation gives the radiative flux in the precursor region due to emission in the shock layer by using the tangent slab approximation. However, as discussed previously in this text, this assumption is not valid in the precursor region. In the precursor, the shock layer no longer appears to be of infinite extent but appears to be a finite disk of gas. An equation will now be derived which properly accounts for the dimensions of the body and shock layer in the calculation of the radiative flux.

If it is assumed that the point of interest is in the precursor and that the emission from the precursor region is negligible, then equations (C-16) and (C-17) for the radiative intensity from the right and left side of the point reduce to

$$I_\nu^R = I_\nu^{wall} e^{-\frac{\tau_\nu}{\mu}} + \int_0^{\tau_\nu^s} \frac{S_\nu}{\mu} e^{-\frac{(\tau_\nu - \tau_\nu')}{\mu}} d\tau_\nu' \qquad \text{(C-27)}$$

$$I_\nu^L = 0$$

As can be seen in Figure 59, at a point in the precursor the shock comprises only a small part of the spherical field of view. Therefore, in this region the solid angle over which the radiative intensity should be integrated must be properly calculated. Considering the geometry of the problem, the expression relating the radiative flux to the radiative intensity is given by

$$q_\nu = \int_0^{2\pi} \int_{\mu_{bdy}}^{1} I_\nu^R \mu \, d\mu d\phi \qquad \text{(C-28)}$$

where μ_{bdy} is the cosine of half of the angle subtended by the body,

$$\mu_{bdy} = Cos(\beta) \qquad \text{(C-29)}$$

In equation (C-28) the radiative intensity from the left of the point of interest is omitted since this term is zero. By integrating over μ in this equation from μ_{bdy} to 1 rather than from 0 to 1 as in equation (C-18), the solid angle considered is only that subtended by

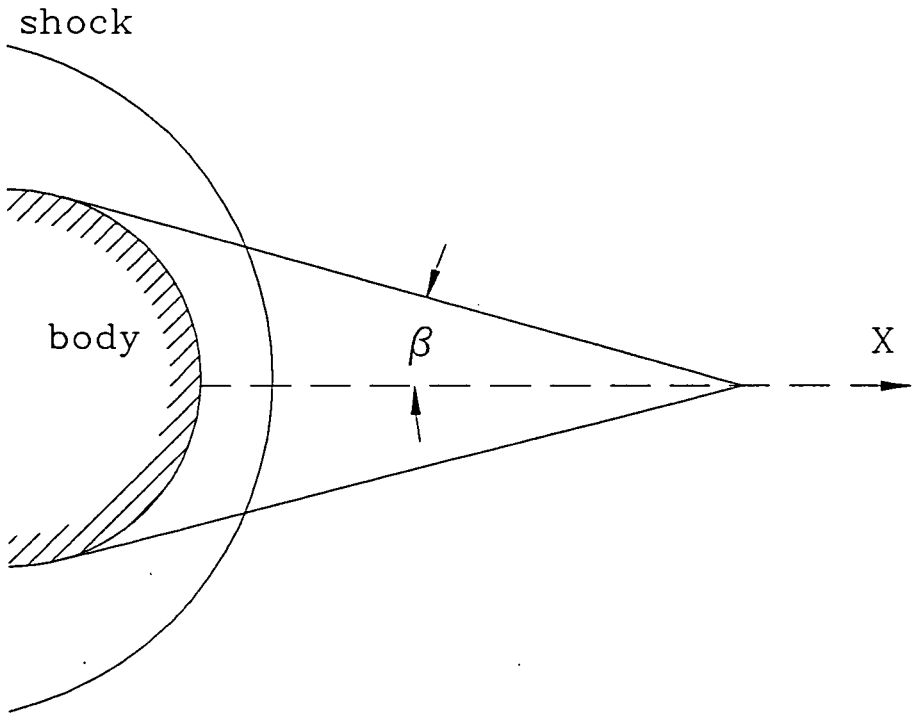

Figure 58: Geometry for the Derivation of the Radiative Flux from a Finite Diameter Body

the body. Combining equations (C-27) and (C-28) and performing the integration over ϕ, the equation for the radiative flux in the precursor region is

$$q_\nu = 2\pi I_\nu^{wall} \int_{\mu_{bdy}}^{1} \mu e^{-\frac{\tau_\nu}{\mu}} d\mu + 2\pi \int_0^{\tau_\nu^s} S_\nu \int_{\mu_{bdy}}^{1} e^{-\frac{(\tau_\nu - \tau_\nu')}{\mu}} d\mu d\tau_\nu' \qquad \text{(C-30)}$$

By dividing the integrals over μ into two parts, the first from 0 to 1 and the second from 0 to μ_{bdy}, as well as the introduction of the exponential integrals, this equation can be written as

$$q_\nu = 2\pi I_\nu^{wall} E_3(\tau_\nu) \left[1 - \frac{\int_0^{\mu_{bdy}} \mu e^{-\frac{\tau_\nu}{\mu}} d\mu}{E_3(\tau_\nu)} \right]$$

$$+ 2\pi \int_0^{\tau_\nu^s} S_\nu E_2(\tau_\nu - \tau_\nu') d\tau_\nu' \left[1 - \frac{\int_0^{\tau_\nu^s} \int_0^{\mu_{bdy}} e^{-\frac{(\tau_\nu - \tau_\nu')}{\mu}} d\mu d\tau_\nu'}{\int_0^{\tau_\nu^s} E_2(\tau_\nu - \tau_\nu') d\tau_\nu'} \right] \qquad \text{(C-31)}$$

Now, introducing a change in the variable of integration for the two remaining integrals over μ such that

$$\mu' = \frac{\mu}{\mu_{bdy}}$$

$$d\mu' = \frac{1}{\mu_{bdy}} d\mu \qquad \text{(C-32)}$$

converts these integrals into the form of the exponential integrals

$$q_\nu = 2\pi I_\nu^{wall} E_3(\tau_\nu)\left[1 - \frac{\int_0^1 \mu_{bdy}^2 \mu' e^{-\frac{\tau_\nu}{\mu_{bdy}\mu'}} d\mu'}{E_3(\tau_\nu)}\right]$$

$$+ 2\pi \int_0^{\tau_\nu^s} S_\nu E_2(\tau_\nu - \tau_\nu') \, d\tau_\nu' \left[1 - \frac{\int_0^{\tau_\nu^s}\int_0^1 \mu_{bdy} e^{-\frac{(\tau_\nu - \tau_\nu')}{\mu_{bdy}\mu'}} d\mu' d\tau_\nu'}{\int_0^{\tau_\nu^s} E_2(\tau_\nu - \tau_\nu') \, d\tau_\nu'}\right] \quad \text{(C-33)}$$

or

$$q_\nu = 2\pi I_\nu^{wall} E_3(\tau_\nu)\left[1 - \mu_{bdy}^2 \frac{E_3\left(\frac{\tau_\nu}{\mu_{bdy}}\right)}{E_3(\tau_\nu)}\right]$$

$$+ 2\pi \int_0^{\tau_\nu^s} S_\nu E_2(\tau_\nu - \tau_\nu') \, d\tau_\nu' \left[1 - \mu_{bdy} \frac{\int_0^{\tau_\nu^s} E_2\left(\frac{(\tau_\nu - \tau_\nu')}{\mu_{bdy}}\right) d\tau_\nu'}{\int_0^{\tau_\nu^s} E_2(\tau_\nu - \tau_\nu') \, d\tau_\nu'}\right] \quad \text{(C-34)}$$

Evaluating the integrals over τ_ν' of the exponential integrals from 0 to τ_ν^s and substituting the definition for μ_{bdy}, (C-29), equation (C-34) becomes

$$q_\nu = 2\pi I_\nu^{wall} E_3(\tau_\nu)\left[1 - Cos^2(\beta)\frac{E_3(\tau_\nu Sec(\beta))}{E_3(\tau_\nu)}\right] +$$

$$2\pi \int_0^{\tau_\nu^s} S_\nu E_2(\tau_\nu - \tau_\nu') \, d\tau_\nu' \left[1 - Cos^2(\beta)\frac{E_3((\tau_\nu - \tau_\nu^s)Sec(\beta)) - E_3(\tau_\nu Sec(\beta))}{E_3(\tau_\nu - \tau_\nu^s) - E_3(\tau_\nu)}\right] \quad \text{(C-35)}$$

This equation gives the radiative flux in the precursor due to emission in the shock layer properly accounting for the decreased field of view occupied by the hot shock layer. Comparing this equation to equation (C-26) for the radiative flux in the precursor using the tangent slab approximation, it can be seen that the presence of the terms in brackets is the only difference between them. These terms are essentially attenuation factors which can be used to modify each term in the tangent slab equation to account for the attenuation due to the three dimensional geometry of the problem. The first term in brackets is the attenuation factor for the wall radiation and the second term in brackets is the attenuation factor for the radiation from the shock layer

$$AF_{\nu}^{bdy} = \left[1 - Cos^2(\beta)\frac{E_3(\tau_{\nu} Sec(\beta))}{E_3(\tau_{\nu})}\right]$$

$$AF_{\nu}^{shck} = \left[1 - Cos^2(\beta)\frac{E_3((\tau_{\nu}-\tau_{\nu}^{s})Sec(\beta)) - E_3(\tau_{\nu} Sec(\beta))}{E_3(\tau_{\nu}-\tau_{\nu}^{s}) - E_3(\tau_{\nu})}\right] \qquad \text{(C-36)}$$

VITA

Scott Alan Stanley was born in Shawnee Mission, Kansas on August 19, 1965. After graduating from Gainesville High School, Gainesville, Texas in 1983 he attended Cooke County College for one year. He then transferred to Texas A&M University where he received his BS degree in Aerospace Engineering in 1988. In the August of the same year, he returned to Texas A&M to continue his education in the Aerospace Engineering Department. He will receive his MS degree in December of 1990 and expects to begin a career in the Aerospace industry in the following January.

Correspondence may be addressed to him care of W.C. and Nona Stanley, 709 S. Morris, Gainesville, Texas 76240.